CONTROL OVER EXTREME-ULTRAVIOLET HIGH-HARMONIC GENERATION FROM GASES AND SOLIDS

Sylvianne D.C. Roscam Abbing

Ph.D. thesis, Vrije Universiteit van Amsterdam, 2023
Control over Extreme-Ultraviolet High-Harmonic Generation from Gases and Solids
Sylvianne D.C. Roscam Abbing

ISBN: 978-90-833032-7-7
Cover design: Georges Hendriks

The work described in this thesis was carried out at the Advanced Research Center for Nanolithography (ARCNL), a public-private partnership between the University of Amsterdam (UvA), the Vrije Universiteit Amsterdam (VU Amsterdam), the Netherlands Organisation for Scientific Research (NWO), and the semiconductor equipment manufacturer ASML.

VRIJE UNIVERSITEIT

CONTROL OVER EXTREME-ULTRAVIOLET HIGH-HARMONIC GENERATION FROM GASES AND SOLIDS

ACADEMISCH PROEFSCHRIFT

ter verkrijging van de graad Doctor of Philosophy aan
de Vrije Universiteit Amsterdam,
op gezag van de rector magnificus
prof.dr. J.J.G. Geurts,
in het openbaar te verdedigen
ten overstaan van de promotiecommissie
van de Faculteit der Bètawetenschappen
op maandag 27 maart 2023 om 13.45 uur
in een bijeenkomst van de universiteit,
De Boelelaan 1105

door

Sylvianne Dorothea Christina Roscam Abbing

geboren te Leiden

promotor:	dr. S.M. Witte
copromotor:	dr. P.M. Kraus
promotiecommissie:	prof.dr. M.L. Groot prof. J. Petersen prof.dr. W.M.J.M. Coene prof.dr. A. F. Koenderink dr. E. Olsson

Contents

1
Introduction

1.1. Ultrafast and ultrasmall

The interaction between light and matter determines how we see the world around us. Studying this interaction lies at the basis of understanding our surroundings, and has driven technology with an accelerating rate over the last decades. The discovery of the laser [1] in 1960 has revolutionized the field of science that studies light-matter interaction, as it provided a source of coherent, collimated, and monochromatic light. These unique properties allowed to produce light intensities that where not achievable before. Successively, it triggered the development of technologies that enabled the generation of ultrashort pulses of light, from the picosecond (= 10^{-12} s) [2] down to the femtosecond (= 10^{-15} s) [3, 4] regime, which is the timescale at which electrons interact and behave naturally. The assets of high intensity and ultrashort duration were unified by the invention of the CPA [5] (chirped pulse amplification), acknowledged with a Nobel prize in 2018 [6]. The technique enabled the generation of high intensity ultrashort light pulses, up to the point that the pulses allow for modification of the optical and electronic properties of the matter they interact with. For sufficiently high intensities, the interaction can lead to the generation of new wavelengths, a field of physics which is described by nonlinear optics [7, 8]. This type of nonlinear interactions led to an evolution of accessible wavelengths, specifically shorter wavelengths with higher photon energies. The ability to resolve small features in matter is restricted due to the Abbe diffraction limit [9], which directly relates the minimum resolvable distance to the wavelength of the light involved in the interaction. The access to shorter wavelengths has therefore opened up the investigation of light-matter interaction on the ultrasmall (nanometer (nm) = 10^{-9} m) scale. The interaction at these small scales lies at the basis of nanolithography [10], which is the key technology that is used to produce the nm features in semiconductor chips. Access to ultrafast and ultrasmall light-matter interaction unlocked new domains of science, such as femtochemistry [11], that before remained unexplored and were only accessible through indirect observations. Furthermore, investigation of the ultrafast and ultrasmall aspects of our world inspired the field of attosecond science [12], that investigates the primary processes following excitation in all scientific disciplines of biology, chemistry, and physics.

1.2. High-harmonic generation

The light source that has driven the field of attosecond science over the last decades is based on the process of high-harmonic generation (HHG), which was discovered experimentally in the late eighties [13, 14]. Under strong irradiation of an ultrafast pulse, gases were shown to emit a broadband spectrum extending into the extreme-ultraviolet (XUV, defined as broadband electromagnetic radiation from 10 eV to 120 eV) range. The strong laser field allows for the excitation of electrons, which are subsequently accelerated and eventually recombine with the parent ion, leading to the emission of high energy photons [15, 16]. The intrinsic short timescales at which the XUV bursts are generated [17–19], enable the investigation of electron dynamics with attosecond resolution in gases [20–22] and condensed matter [23]. In addition, the short wavelengths allow for investigation and imaging of small structures with high resolution [24, 25], for instance through lensless imaging [26–28]. Moreover, the XUV bursts itself contain encoded information on the strong-field light-matter interaction that generates the high harmonics. This additional property is explored in the field of high-harmonic spectroscopy [29], which for example allows to reconstruct molecular orbitals [30, 31]. The underlying mechanism of gas-based HHG has been well understood [32], and revealed the possibility to push HHG into the soft X-ray regime (defined as radiation from 120 eV to 1200 eV) [33] and increase the element sensitivity and spatial resolution of the technique.

Whereas gas-based HHG was discovered experimentally, the generation of high harmonics from solid-state materials was predicted theoretically [34, 35], before the first experimental demonstration. The existence of solid-based HHG was confirmed in 2011 by the experimental observation of HHG from ZnO [36], which demonstrated that photon energies extending beyond the bandgap of ZnO could be generated by driving with mid-infrared laser pulses. Ever since the discovery, solid-based HHG has been shown in a wide variety of materials such as semiconductors [37–39], wide bandgap dielectrics [40–45], thin-film materials [46], two-dimensional materials [47, 48], and metals [49]. The choice of wavelength of the driving laser allows to generate energies extending from the THz [37] to the XUV regime [40]. Moreover, the generation from patterned solids [50–53] demonstrated the additional benefit of solid HHG to engineer the generated wavefront and process through geometrical confinement of the strong-field light-matter interaction. The generation of high harmonics from solids emerges from the strong-field induced carrier dynamics [35] within a periodic potential, which is determined by the electronic properties of the material under investigation. More specifically, the strong field causes excitation and recombination of carriers between the valence and the conduction band, referred to as the interband process. Additionally, the acceleration of carriers within the bands leads to HHG due to intraband processes. Since the carriers are bound to follow the energy landscape of the material, solid-based HHG can be used to directly probe band structures [39, 40, 54–56], electron dynamics [41, 57], and Berry curvatures [58], through high-harmonic spectroscopy. The high density and additional flexibility to structure the medium, in combination with the ultrafast induced electron dynamics, will enable solid-based HHG to empower the field of attosecond photonics [59, 60].

Evidently, HHG is an excellent technique to obtain broadband coherent ultrashort XUV pulses in a table-top setting, allowing for next-generation attosecond science and metrology. However, the applications of HHG remain restricted due to the limited brightness of the XUV pulses. So far, probing of electron dynamics has mainly been achieved with the assistance of an infrared or visible pulse, worsening the temporal resolution. Applications to achieve higher spatial and temporal resolution rely on the interferometry of two XUV pulses [61, 62], or even their nonlinear interaction [63], which is only feasible with high enough XUV intensity. Additionally, the low signal-to-noise requires long integration times, sensitive detectors, and challenging experimental conditions. The XUV intensity is limited due to the inherently low conversion efficiency (10^{-8} to 10^{-6}) of the HHG process. In addition, to achieve high intensity at the interaction plane, proper focusing of the XUV wavefront is crucial. However, shaping of the XUV wavefront after generation is by all means non-trivial, since the short XUV wavelengths are absorbed in almost any material, and the use of conventional optical elements is limited. Since the XUV wavefront and the HHG efficiency are determined by the light-matter interaction that leads to the generation of high harmonics, control over the HHG process is crucial to improve the XUV intensity and the applicability of HHG sources.

1.3. Outline

The goal of this thesis is to investigate novel methods to control the HHG process to improve the efficiency and engineer the XUV wave front. Through a set of different experiments, it is demonstrated that multi-color driving, structuring the generation medium, and pre-exciting the medium, will all offer control parameters over HHG. To start with, we describe the theoretical background of high-harmonic generation in Chapter 2. Here we elaborate on the concept of extreme nonlinear optics, followed by a description of the microscopic properties of the HHG process in both a semiclassical and quantum mechanical framework, and discuss the macroscopic properties of the HHG process. The general methods to perform the experiments and simulations presented in this thesis are described in Chapter 3, which contains details on the generation of the ultrashort pulses, a description of the optical setups, and reports on the material parameters of the solid samples used in the experiments. Control over the divergence and efficiency of gas-based HHG is presented in Chapter 4. Driving the HHG process with both the fundamental and its second harmonic simultaneously, allows to control the ionization process and the electron dynamics with sub-cycle precision and enables optimization of the yield and the divergence of the XUV wavefront. The potential of structuring the generation medium in solid-based HHG is explored in Chapter 5. We demonstrate that geometrical modifications of the HHG process in micrometer- and nanometer-sized silica structures facilitates control over the phase, amplitude, and polarization of the generated XUV wavefront. Additionally, we use the coherent diffractive emission from these structures to probe near-field confinement in nanostructures and to image complex structures with sub-fundamental-wavelength resolution. In Chapter 6, we present that two-color XUV high-order wavemixing from silica follows perturbative intensity scalings and boosts the conversion efficiency of solid-based HHG by at least one order of magnitude. A quantum theory is used to describe the underlying generation mechanism and reveals that the HHG process is enhanced due to laser-dressed states. Finally, we demonstrate the technique of transient grating high-harmonic spectroscopy in MgO in Chapter 7, and observe that pre-excitation of the solid enables control over the XUV wavefront and the HHG process. Preliminary analysis shows that the XUV wavefront is modified due to the combination of macroscopic propagation effects of the fundamental and microscopic generation properties of the HHG process.

2

Theoretical Background

2.1. Introduction - Extreme nonlinear optics

Over the last decades it has become possible to produce ultrashort femtosecond laser pulses [3, 4], such that research on light-matter interaction in the ultrafast domain has become accessible. In addition to the ultrafast timescales, the short pulses allow for reaching intensities of the light which can modify the optical and electronical properties of matter, which unlocks a regime with rich and new physics [12, 64, 65]. In order to describe the interaction of the intense ultrashort pulses with matter, we start by defining the complex electric field amplitude of a linearly polarized pulse as [66],

$$\mathbf{F}(t) = F_0(t)e^{i(\phi(t))} + c.c. \tag{2.1}$$

with $F_0(t)$ the temporal envelope, which determines the length and the spectral width of the pulse, and an oscillating component with a temporal phase $\phi(t)$. The c.c component is required to make the value of the field real, but we discard this term to simplify notation further on. We categorize the temporal phase into three contributions, $\phi(t) = \phi_0 + \omega_0 t + \phi_{\text{add}}(t)$. The first contribution is the carrier-envelope phase, ϕ_0, which determines the offset of the oscillating wave with the temporal envelope. For pulses that consist of only a few cycles, the peak intensity of the pulse will be sensitive to the carrier-envelope phase, which then has a significant impact on the light-matter interaction [67]. In this thesis, we use pulses with many optical cycles, such that the carrier-envelope phase does not have any significant influence on the peak intensity and therefore we set this phase to 0 rad. The second contribution determines the frequency of the oscillations in the pulse and is set by the central angular frequency ω_0. The third contribution accounts for any additional phase $\phi_{\text{add}}(t)$, which originates from dispersion effects during propagation of the pulse, such as chirp. To simplify calculations, we neglect the additional phase throughout this chapter.

When a short pulse interacts with a material, the strong electric field exerts a force on the carriers inside the material and induces microscopic charge separation, which leads to a polarization $\mathbf{P}(t)$. For moderate strengths of the electric field, the carrier motion follows the oscillations of the electric field, which results in a linear polarization $\mathbf{P}^{\mathrm{L}}(t)$ [8]. As the field strength increases, the carrier acceleration becomes perturbed, which results in nonlinear contributions to the polarization, $\mathbf{P}^{\mathrm{NL}}(t)$. The total polarization is defined as the combination of the linear and nonlinear contributions,

$$\mathbf{P}(t) = \mathbf{P}^{\mathrm{L}}(t) + \mathbf{P}^{\mathrm{NL}}(t) = (\chi^{(1)}\mathbf{F}(t) + \chi^{(2)}\mathbf{F}^2(t) + \chi^{(3)}\mathbf{F}^3(t) + ...) \tag{2.2}$$

where χ^j denotes the j-th order optical susceptibility. As follows from this definition, only materials with properties that results in a non-zero χ^j are able to induce the corresponding j-th order polarization. As a consequence of the nonlinear polarization, electric fields with different frequencies than the central frequency w_0 are generated. The underlying physics of the conversion from one frequency into another is described by nonlinear optics [8, 68, 69]. As an example, materials that posses a $\chi^{(2)}$ or $\chi^{(3)}$ can generate the second [7] and third [8] harmonic of the central frequency w_0, respectively. In some materials, the strong field can induce a significant $\chi^{(j)}$, which leads to the generation of low-order harmonics, defined as Kerr-type harmonic generation [70]. The magnitude of the optical susceptibility drops significantly fast for higher orders [71], such that the generation of higher harmonics due to higher order susceptibilities $\chi^{(j)}$ becomes very inefficient, resulting in a characteristic spectral shape. The intensity scaling of harmonics, generated by a $\chi^{(j)}$-th order susceptibility, increases according to a perturbative law, set by the order of nonlinearity j.

At even higher intensities of the pulse, the perturbative regime will not be sufficient to describe the light-matter interaction, and we enter the domain of extreme nonlinear optics [34], which includes high-harmonic generation (HHG). This chapter provides the theoretical background of the interaction of a strong laser field with either gases or solids, which leads to HHG. At first, we approach the microscopic aspects using semiclassical concepts, which provides tools to understand the main characteristics of HHG, but is not able to fully describe the underlying physics. Therefore, also a quantum mechanical approach is described, to provide a more complete picture of the microscopic generation mechanisms. Finally, the macroscopic properties of HHG will be presented, to correctly reproduce an experimental setting. Throughout this thesis atomic units ($e = m = \hbar = 4\pi\epsilon_0 = 1$) are used, unless stated otherwise.

2.2. Semiclassical approach

The generation of high harmonics originates from the carrier dynamics that are induced by a strong laser field, and was initially observed for a gas [13, 14]. Conceptually, HHG can be described by just three steps [15, 16, 72]: the ionization of an electron, the propagation through the continuum, and the recombination of the electron with the parent ion, see Fig. 2.1a. In the recombination step, the energy accumulated by the electron is converted into high energy photons due to recollision with the parent ion. It is this recollision-type HHG, that has driven the field of attosecond science over the last decades. In analogy, the three-step model can also describe the solid-state HHG process

[73], see Fig. 2.1b. The process starts with the excitation of an electron from the valence to the conduction band, leaving behind a hole in the valence band. Subsequently, the electron (hole) propagates along the conduction (valence) band during the second step. Finally, the interband recombination of the electron with the hole results in the emission of high energy photons. The recombination mechanism is equivalent to the recollision-type HHG in gases and will be described in section 3. For both gas and solid HHG, the first step involves the excitation of carriers across a potential barrier by strong-field ionization [74], which will be described in section 1. The strong-field ionization indicates that the carriers tunnel through the potential barrier, which inherently involves a quantum mechanical process, making the overall three-step model semiclassical. Additionally, the nonlinearity of the strong-field ionization can lead to the generation of low-order Brunel harmonics [70, 75]. The propagation step of the carriers in both the gas or solid HHG process can be described fully classically, as is presented in section 2. In solid HHG, the acceleration of the carriers across the nonlinear curvature of the energy bands also results in the generation of high energy photons, associated with velocity harmonics [76].

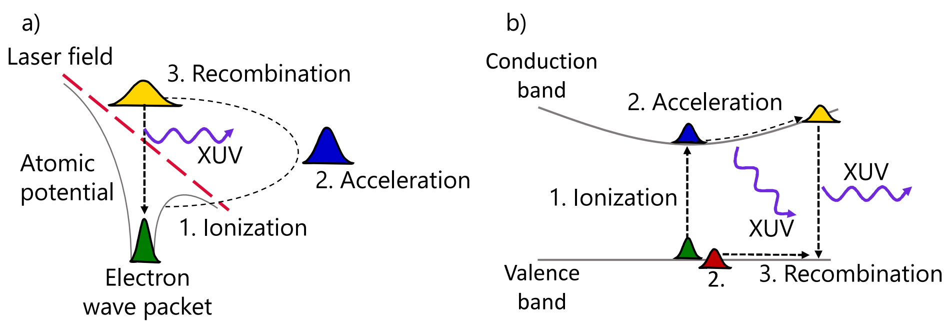

Figure 2.1: The three-step model: a) gas HHG: the ionization (1) of an electron (wave packet), followed by the acceleration (2) of the electron, leads to the generation of XUV photons due to recombination (3) of the electron with the parent ion. b) In solid HHG the ionization creates an electron (hole) in the conduction (valence) band. The nonlinear acceleration of the carriers during the propagation step leads to harmonic radiation. Additionally, harmonics are generated upon recombination of the electron with the associated hole.

2.2.1. Ionization - Strong-field ionization and Brunel harmonics

The emission of any harmonic generation starts with the promotion of electrons from the ground state to an excited state, which is either a continuum state for gas-based HHG, or a bound state in an energy band for solid-based HHG. The process of exciting carriers can be described by strong-field ionization, defined by Keldysh for both the atomic and solid case [74]. The characteristics of strong-field ionization are summarized by the adiabatic Keldysh parameter:

$$\gamma_k = \frac{\omega}{F_0}\sqrt{2I_p} = \frac{\omega}{F_0}\sqrt{2E_g}. \tag{2.3}$$

This parameter depends explicitly on the field strength F_0, the fundamental frequency ω, and the energy gap between the ground state and the excited state, either the ionization potential I_p or the energy bandgap E_g, for an atom or a solid, respectively. To obtain this expression, the assumption is made that the Coulomb potential of the excited electron and the remaining positively charged component is neglected, which is referred to as the strong-field approximation (SFA) [77]. Three relevant regimes are indicated by the Keldysh parameter γ_k, that will change the underlying mechanism of how an electron will be promoted to the excited state. For $\gamma_k >> 1$, the excitation occurs through multiphoton ionization (MPI), which resembles the excitation of an electron through the absorption of multiple photons simultaneously, necessary to cross the energy barrier. For example, to excite an electron across the energy gap of MgO (7.8 eV), we will need about five 800-nm (1.55 eV) photons. In the situation that $\gamma_k << 1$, the excitation of an electron can be described by tunneling ionization (TI). Due to the strong electric field, the energy barrier is distorted, such that an electron can tunnel through the barrier. In the intermediate regime, for $\gamma_k \approx 1$, the excitation is described by diabatic tunneling, in which the electron quickly changes energy levels, to become excited. This concept will be discussed in more detail in the quantum mechanical approach. For a given energy gap, or ionization potential, and a given wavelength of the driving laser, the intensity is the control parameter to determine which process describes the ionization.

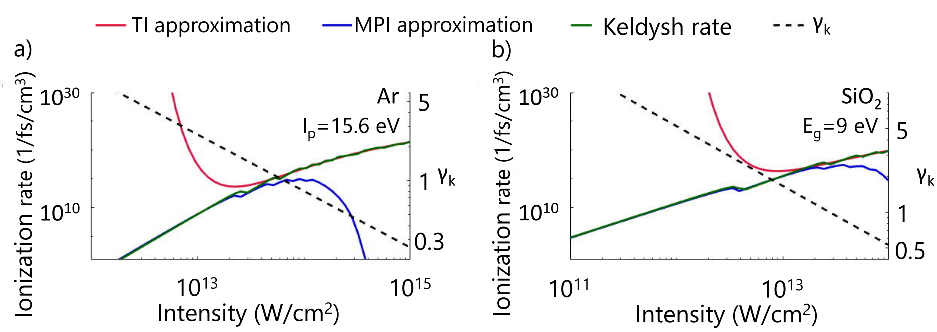

Figure 2.2: The Keldysh rate (green) and parameter (dashed black line), for general atomic (a) and solid (b) HHG conditions, driven by 800-nm pulses. The ionization rate is also shown for the approximation that tunnel ionization (TI, red) or multiphoton ionization (MPI, blue) is the dominating excitation mechanism.

As an example, Fig. 2.2 shows the full Keldysh ionization rate (green line) for an Argon atom and for a SiO_2 bandgap, respectively, for a range of intensities at which HHG occurs for an 800-nm pulse. Additionally, Keldysh approximated the ionization rates for the case that TI or MPI is the dominating excitation mechanism, which are also shown in Fig. 2.2, as the red and blue line respectively. The equations for the full Keldysh rate, the approximated TI rate, and the approximated MPI rate, can be found in Appendix A, and are calculated and formulated following the approach presented in [78]. As expected, the Keldysh ionization rate is approximated by MPI for $\gamma_k >> 1$, and can be approximated by TI for $\gamma_k << 1$. For the generation intensities required to obtain harmonics from Argon

(10^{14} W/cm^2), the Keldysh parameter (dashed black line) has a value below 1, meaning the ionization can be described by TI. At lower intensities, the Keldysh parameter becomes higher than 1, and the ionization can be described by MPI. Since the ionization potential of Argon (15.6 eV) is large compared to the driving photon energy (1.55 eV), the ionization rate approximated by MPI will be inefficient. The generation conditions for a solid are different. In general, the energy gap of a solid is smaller than the ionization potential of the gases used for HHG. This means that a lower intensity is needed to reach Keldysh parameters above 1, and to achieve efficient ionization. Due to the lower damage threshold of solids (a few 10^{13} W/cm^2 for SiO_2), it is difficult to reach far into the TI regime. Typically, the generation conditions for solid HHG imply a Keldysh parameter around 1, meaning we find ourselves in the diabatic tunneling regime, which will be elaborated on in the quantum mechanical section, presented later in this chapter.

The strong-field ionization rate, as defined by Keldysh, only accounts for a monochromatic cycle-averaged increase of the excited-state carrier population. Effectively, this leads to a step-wise increase of the carrier population, where the electrons are excited at the peak of the electric field. However, if we excite carriers with a femtosecond pulse, the strong-field ionization has a sub-cycle character and the growth in carrier population follows a nonlinear trend. A lot of work has followed up on the initial work by Keldysh, to describe the sub-cycle dynamics of strong-field ionization [79–81]. In Chapter 4 of this thesis, the ADK-rate [82] is used to determine the ionization rate in a two-color field.

$$\mathrm{ADK} \propto e^{\frac{2(2I_p)^{1.5}}{3|\mathbf{F}(t)|}}. \tag{2.4}$$

A rapidly changing electron population can lead to the generation of low-order harmonics, which originate from the nonlinearities in the sub-cycle strong-field ionization. This harmonic generation mechanism was initially proposed by Brunel [75], hence we refer to this source of radiation as Brunel harmonics. The origin of other low-order harmonics due to strong-field ionization is described in more detail in [70].

2.2.2. Propagation - Classical description for gases and solids

Atomic trajectories

In the atomic case, the propagation of the electron through the continuum can be described fully classically [15]. We determine the position of the electron in space, denoted by the variable x, upon interaction with a monochromatic linearly polarized electric field. The electron is driven by the force of the electric field, and the position x can be retrieved by solving the equation of motion $d^2x/dt^2 = -F(t)$, which is formulated in atomic units. Through integration of the equation of motion, starting from the ionization time t', we find the velocity $v(t)$ of the electron at time t,

$$\begin{aligned} v(t) &= -\int_{t'}^{t} F_0 \cos(\omega\tau)\mathrm{d}\tau + v_0, \\ &= -\frac{F_0}{\omega}[\sin(\omega t) - \sin(\omega t')] + v_0. \end{aligned} \tag{2.5}$$

In the semiclassical approach, the initial velocity v_0 of the electron is assumed to be zero. With a second step of integration, we find the position of the electron, which is formulated as:

$$\begin{aligned} x(t) &= \int_{t'}^{t} v(\tau)\mathrm{d}\tau \\ &= \frac{F_0}{\omega^2}\left(\cos(\omega t) - \cos(\omega t') + \sin(\omega t')\omega(t-t')\right) \end{aligned} \tag{2.6}$$

This expression allows to calculate the trajectory of the electron for any time of ionization t' in the laser cycle, which will lead to a unique set of trajectories, see Fig. 2.3a. All trajectories start at $x(t') = 0$, and will recombine with the parent ion at a later time t, if $x(t) = 0$. Each ionization time has an associated recombination time, which can be used to calculate the kinetic energy K of the electron, accumulated during the propagation:

$$K(t) = \frac{1}{2}v^2(t) = 2U_p[\sin(\omega t) - \sin(\omega t')]^2, \tag{2.7}$$

with the ponderomotive energy defined as $U_p = F_0/4\omega^2$. The kinetic energy, in units of the ponderomotive energy, is shown as a function of ionization time in Fig. 2.3b. This figure indicates that there are two electron trajectories that will accumulate the same kinetic energy during the propagation. These contributions are referred to as the short and the long trajectories, linked to the relative length of both trajectories. There is one energy, in which these two trajectories merge, which is the highest kinetic energy that the electron can obtain, which is equivalent to 3.17 U_p.

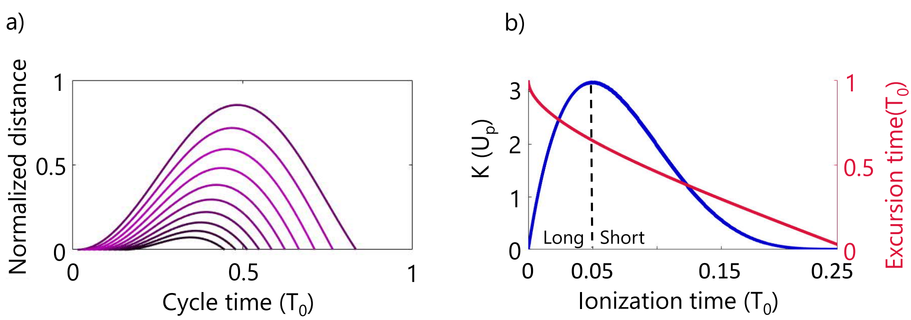

Figure 2.3: a) Electron trajectories. Each ionization time leads to a unique trajectory. b) Accumulated kinetic energy (blue) in units of U_p for a range of ionization times. There are two ionization times that lead to the same kinetic energy, refered to as the long and short trajectory, related to the length of the excursion time (red) of each trajectory.

As will be elaborated on in Chapter 4, the presence of both long and short trajectories is not favorable for the divergence properties of HHG. The contributions from the long and short trajectories can be manipulated [83], by adding a second electric field to the generation process. In the case that both fields are aligned along the same axis, and obtain the same polarization, the two-color field can be described one-dimensional and is defined as

$$F(t) = F_0 \cos(\omega t) + \alpha F_0 \cos(2\omega t + \phi_{2\omega}), \tag{2.8}$$

in which the second electric field represents the second harmonic of the fundamental driver, with a relative two-color phase $\phi_{2\omega}$. The strength of the second field is determined as a fraction α of the fundamental field amplitude F_0.

The angle between the polarization direction between the fundamental and second harmonic field is defined as θ, and can be used as a control parameter to influence the HHG process. We define that the fundamental field is aligned along the x-direction, and depending on the angle θ, the second harmonic field has a component in both the x- and y-direction. The two-color field becomes two-dimensional and is defined as,

$$\begin{aligned} F_x(t) &= F_0 \cos(\omega t) + \alpha \cos(\theta) F_0 \cos(2\omega t + \phi_{2\omega}), \\ F_y(t) &= \alpha \sin(\theta) F_0 \cos(2\omega t + \phi_{2\omega}). \end{aligned} \tag{2.9}$$

The equation of motion of the electron can be defined for both dimensions separately, which leads to the following definitions of the position of the electron along x and y,

$$\begin{aligned} x(t) = &\frac{F_0}{\omega^2} \, (\frac{1}{2}[\cos(\omega t) - \cos(\omega t') + \sin(\omega t')\omega(t - t')] \\ &+ \frac{1}{8}\alpha \cos(\theta)[\cos(2\omega t + \phi_{2\omega}) - \cos(2\omega t' + \phi_{2\omega}) + \sin(2\omega t' + \phi_{2\omega})2\omega(t - t')]), \end{aligned} \tag{2.10}$$

$$y(t) = \frac{F_0}{\omega^2} \, (\frac{1}{8}\alpha \sin(\theta)[\cos(2\omega t+\phi_{2\omega})-\cos(2\omega t'+\phi_{2\omega})+\sin(2\omega t'+\phi_{2\omega})2\omega(t-t')]). \tag{2.11}$$

Depending on the relative polarization angle, relative phase, and relative strength between the two-color fields, the electron trajectories can be manipulated, as presented in Chapter 4.

Solid motion

In the case of solid HHG the propagation of the carriers can also be described classically [34, 40]. Instead of freely propagating in the continuum, as for the atomic case, the electron (hole) is accelerated inside the conduction (valence) band. Therefore, the equation of motion is given by the propagation of the carrier along the energy dispersion of the band. In the tight-binding approximation, in one dimension, the energy dispersion relation of the energy band λ along momentum k, can be described as [84]

$$E_\lambda(k) = \sum_x \epsilon_\lambda(x) \cos(kx) \tag{2.12}$$

in which the band coefficients $\epsilon_\lambda(x)$ represent the amplitude of the spatial harmonics of the lattice structure along the x-dimension. As an example, the energy dispersion of the lowest lying conduction band of SiO_2 is shown in Fig. 2.4a, along the crystal direction

Γ-M. The velocity of the carrier in band λ is defined as

$$v^{\lambda}(k) = \frac{\partial E_{\lambda}(k)}{\partial k}, \tag{2.13}$$

and is denoted in the same figure by the red line. Around the bandgap (k=Γ), the velocity shows a linear dependence on the momentum. For higher momentum, the electron will explore the nonlinear part of the band, indicated by the nonlinear curvature of the velocity.

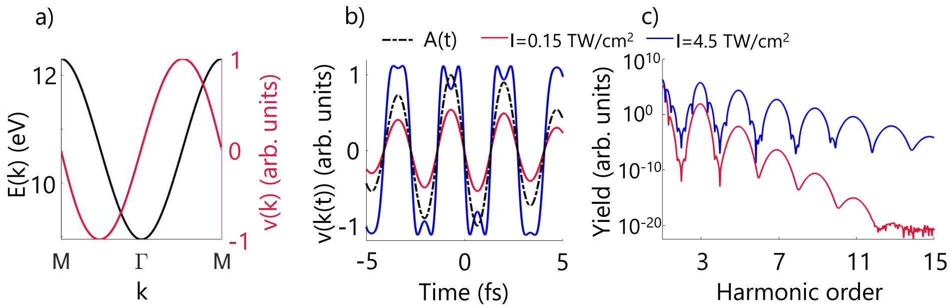

Figure 2.4: a) Conduction band of SiO_2 and velocity $\nabla E(k)$. b) Electron velocity during laser interaction, for a moderate and strong electric field. c) Spectral components originating from velocity harmonics.

Upon interaction with a linearly polarized laser field, the momentum of the electron will become time-dependent, which we describe as,

$$K(t) = k(t=0) + A(t), \tag{2.14}$$

with the vector potential, defined by the electric field $F(t)$,

$$A(t) = -\int_{\infty}^{t} F(t')dt'. \tag{2.15}$$

The time-dependent velocity of the electron can then be defined, by substituting the time-dependent momentum, and integrating Eq. 2.12 and 2.13, as,

$$v_{\lambda}(k,t) = -\sum_{x} x\epsilon_{\lambda}(x)\sin[(k+A(t))x]. \tag{2.16}$$

This expression demonstrates that the velocity is dictated by the vector potential $A(t)$. The acceleration of the electron inside the band will resemble a current $J(t)$. Due to nonlinearities in the energy band, and therefore the velocity, the current contains higher frequency components, which will lead to the generation of harmonics. The spectral components of these 'velocity' harmonics can be calculated by Fourier transformation of the time derivative of the current [34, 40],

$$I_{\mathrm{HHG}}(\omega) \propto |\frac{\partial J(t)}{\partial t}|^2 \propto \sum_k |\omega \mathscr{F}[v_\lambda(k,t)]|^2. \tag{2.17}$$

For two different intensities, the time-dependent electron velocity and the corresponding harmonic spectra are shown, see Fig. 2.4b,c, respectively. As expected by the definition in Eq. 2.16, the time-dependent velocity of the electron is dictated by the vector potential (black dashed line). At an intensity of 4.5 TW/cm^2, the amplitude of the vector potential is high enough to accelerate the carriers beyond the most nonlinear part of the band, which corresponds to the highest velocity. Therefore, the velocity drops again after the electrons are accelerated beyond the maximum. Additionally, the electrons mainly experience the nonlinear curvature of the band, resulting in higher yield of the harmonic spectrum for higher intensities, see Fig. 2.4c.

For high enough intensities, the electron is accelerated towards the edge of the Brillouin zone, where it might scatter and undergo a Bloch oscillation as it traverses the Brillouin zone again [85, 86]. The characteristics of this oscillation are described by the Bloch frequency $\omega_B = F_0 a$, which is set by the field strength F_0 and the lattice constant a. The mechanism underlying the generation of velocity harmonics, or equivalently referred to as Bloch harmonics, has been used to explain HHG [36, 37, 40]. Moreover, the Bloch frequency provides a direct explanation for the observed linear scaling between the field strength and the highest generated harmonic [36, 37, 59]. One important feature of the velocity harmonics, is that the emission of all harmonics will be synchronized to the electric field, such that no temporal chirp is present in the emitted harmonic pulse [41, 76, 87, 88]. Potentially, this emission feature can be used to identify the generation mechanism of harmonic orders in an experiment. In addition, the intensity scaling of the velocity harmonics follows a perturbative dependence on the fundamental field strength [34, 40]. The perturbative character of the harmonic yield is used in Chapter 6 of this thesis, to explain the underlying mechanism of solid HHG in silica.

Based on the semiclassical approach, the emission of velocity harmonics, induced by nonlinear velocity components, is not present for atomic HHG, as shown in Fig. 2.5. During the propagation of the electron through the continuum, the electron does not experience any nonlinear acceleration, as the energy follows the expression $k(t)^2 \propto v(t)^2$ (Eq. 2.7), which corresponds to a parabolic energy band, see Fig. 2.5a. The resulting velocity of the accelerated electrons is calculated by taking the derivative of the energy band, according to Eq. 2.13, and has a linear dependence on the momentum. The electron velocity as a function of time is shown in Fig. 2.5b, for the same two intensities used in the example of Fig. 2.4. Since the velocity depends linearly on the momentum, which depends linearly on the vector potential, as defined in Eq. 2.14, the carrier velocity follows the trend of the vector potential. As a result, the velocity does not contain any higher order frequency components that will lead to harmonic generation, and the spectrum is dominated by the frequency of the laser pulse (harmonic order 1), see Fig. 2.5c.

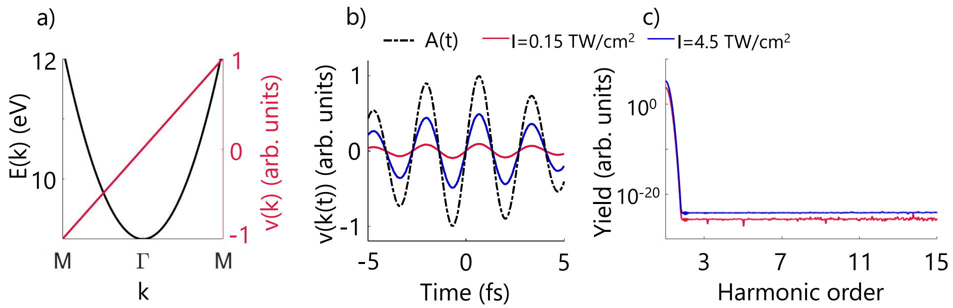

Figure 2.5: a) Parabolic band, representing an atomic energy band, and velocity $\nabla E(k)$. b) Electron velocity during laser interaction, for a moderate and strong electric field. c) Spectral components of the velocity, which demonstrate that velocity harmonics are absent for parabolic energy bands.

2.2.3. Recombination - Emission of high energy photons

Atomic recollision

After the electron has gained kinetic energy K, it will recombine with the parent ion, emitting photons with energies

$$\omega_{\text{xuv}} = I_p + K \tag{2.18}$$

in which I_p denotes the ionization potential of the gas used. The maximum energy, that can be emitted is called the cutoff energy [15]:

$$\omega_{max} = I_p + 3.17 U_p. \tag{2.19}$$

Since the ponderomotive energy depends linearly on the intensity, the cutoff energy scales accordingly, with a quadratic dependence on the field strength. Also, the ponderomotive energy depends quadratically on the wavelength of the driving laser. By using longer driving wavelengths, the electron can gain more kinetic energy during propagation, and eventually reach a higher cutoff. The strategy of using longer driving wavelengths is used to push HHG beyond the soft X-ray regime [89, 90]. As the harmonics are emitted at different recombination times, the temporal spectral shape of the attosecond pulse will be chirped [91–93]. The short trajectories will lead to a positively chirped pulse, whereas the long trajectories result in negative chirp. The temporal shape of the attosecond pulse will have a direct influence on the achievable intensity of the XUV. One of the reasons why short trajectories are favoured over long trajectories, is because positive chirp can be compensated [94, 95] for more easily in the XUV energy regime then negative chirp. The appearance of only odd high harmonics originates from the interference of the attosecond HHG pulses, which are generated in each half-cycle of the fundamental laser pulse. Since the electric field flips sign every half-cycle, only odd harmonics are constructively interfering on the detector. The addition of a second color field, can break the half-cycle symmetry, which leads to the additional detection of even harmonic orders.

Recollision model for solids

In solid HHG, the energy of the photons that are emitted through interband recombination, are given by the energy gap between the electron and the hole at the time of recombination,

$$\omega_{\text{xuv}} = E_g(k(t)) \tag{2.20}$$

As the momentum of the electron is time-dependent in the presence of a laser field, the emitted photon energy is given by the time-dependent energy gap. In a real space depiction, the emission of a photon occurs when the electron recollides with the hole. The position of the electron and hole are given by,

$$x_\lambda(t) = \int_{t'}^{t} \nabla E_\lambda[k(\tau)]d\tau \tag{2.21}$$

in which ∇E_λ resembles the energy dispersion of either the conduction band or valence band.

In contrast to the atomic case, the cutoff energy is not set by the laser field, but is restricted to the maximum electron-hole energy difference that the associated carriers can reach during acceleration. For low intensities, the electron moves around in the part of the energy band surrounding the bandgap. In the case that the band structure of the material surrounding the bandgap can be described by a parabolic shape, the velocity of the electrons will be dominated by a linear component. Therefore, in analogy with the atomic case, the recollision-type HHG for lower intensities suggests a quadratic relation between the field strength and the cutoff energy for those parabolic band structures, which is in contrast with experimental observations of a linear dependence [36, 37]. Based on the recollision mechanism, the temporal shape of the high-harmonic radiation will exhibit temporal chirp [41, 76, 87, 88]. The exact temporal shape will depend on the energy band dispersion. This feature of the recollision-type generation mechanism, has been used to identify the origin of the harmonic generation in several experiments [88, 96], and has been used to reconstruct the band properties in materials [54]. Again, the odd harmonics that are present in the far-field originate from an interference effect between half-cycle emission, and driving HHG with two-color fields can lead to the observation of even harmonics. In addition, a spatial asymmetry can also induce even harmonic orders. Depending on the rotational symmetry of a crystal, a linearly polarized pulse might probe different crystal axis upon interaction, which leads to symmetry breaking and the appearance of even harmonics.

2.3. Quantum mechanical approach

The semiclassical three-step model of HHG is useful to identify some generation mechanisms of high-harmonics, such as Brunel harmonics, velocity harmonics, and recollision-type harmonics. In particular for gas-based HHG the three-step model is sufficient to explain the main features of HHG. However, the variety in experimental observations for solid HHG have led to intense discussions regarding the underlying mechanisms, since not all phenomena could be explained by an universal description. Especially the relative contribution and interaction between the different generation mechanisms in solid HHG is a topic of investigation [59, 97]. To obtain a more complete description, we take into account the quantum mechanical nature of the medium that generates harmonic radiation due to strong-field light-matter interaction. We start with describing the interaction of an electron with a laser field for two set energy levels, to introduce some basic concepts. The two-level model allows to calculate a harmonic spectrum, but is not able to discriminate between interband and intraband contributions. Therefore, as a next step, we include the propagation of carriers along the energy bands. The interaction is solved using Houston states, which treat the eigenstates in an adiabatic basis and allows to disentangle interband and intraband contributions. Next, we introduce the concepts of Bloch oscillations and Wannier-Stark localization, which both occur at high driving intensities of the field. Finally, we end this section with the semiconductor Bloch equations (SBE), which allows to take into account multi-electron interaction.

2.3.1. Field-free basis and Bloch states

For simulating HHG in a two-level system, we follow the approach presented in [87]. We start with describing the interaction of a linearly polarized laser field with a two-level system in one-dimension, in order to determine the electronic wave function. In the velocity-gauge approach the time-dependent Schrödinger equation is given by [87, 98]

$$i\frac{\partial}{\partial t}\left|\Psi(t)\right\rangle = (\hat{H}_0 + \hat{H}_{\text{int}})\left|\Psi(t)\right\rangle, \tag{2.22}$$

where $\hat{H}_0$ is the field-free Hamiltonian and $\hat{H}_{\text{int}}$ is the interaction Hamiltonian, which describes the strong-field light-matter interaction between the laser field and the electron, defined as,

$$\hat{H}_0 = \frac{\hat{p}^2}{2} + V(\hat{x}), \tag{2.23}$$

$$\hat{H}_{\text{int}} = A(t)\hat{p}, \tag{2.24}$$

with $\hat{p}$ the momentum operator, $V(\hat{x})$ the periodic lattice potential, and $A(t)$ the vector potential of the electric field $F(t)$. In this derivation we apply the dipole approximation $A(x,t) = A(t)$, which is justified since the wavelengths involved are larger than the lattice constants, which determine the spatial dimension of the interaction.

The first step is to define the eigenstates of the field-free Hamiltonian, which are defined as the Bloch states [87],

$$\hat{H}_0\left|\phi_{nk}\right\rangle = E_n(k)\left|\phi_{nk}\right\rangle. \tag{2.25}$$

Here n is the level index, k is the crystal momentum and the eigenvalues $E_n(k)$ represent the energy dispersion of the bands along the crystal momentum. The Bloch state can be written out as a plane wave interacting with a function that is periodic in the lattice constant a.

$$\langle x|\phi_{nk}\rangle = e^{ikx} U_{nk}(x), \tag{2.26}$$

in which the function satisfies the periodic condition.

$$U_{nk}(x+a) = U_{nk}(x). \tag{2.27}$$

Since we assume that the vector potential has no dependence along x, each of the momentum channels in k can be solved independently [98, 99]. For a given momentum k_0, we can express the wave function as a linear combination of Bloch states and time-dependent coefficients for energy level n and momentum k_0,

$$|\Psi_{k_0}(t)\rangle = \sum_n C_{nk_0}(t)\,|\phi_{nk_0}\rangle\,. \tag{2.28}$$

The absolute square of the time-dependent coefficients $C_{nk_0}(t)$ represent the population in level n. Making use of this expression, we can rewrite the time evolution in a given momentum channel as,

$$i\hbar\frac{\partial}{\partial t}C_{nk_0} = C_{nk_0}E_n(k_0) + A(t)\sum_{n'} C_{n'k_0}\,p_{k_0}^{nn'}, \tag{2.29}$$

in which $E_n(k_0)$ corresponds to the energy of level n for momentum channel k_0. The coupling strength between levels n and n' is given by the transition matrix element $p_{k_0}^{nn'}$,

$$p_{k_0}^{nn'} = \langle\phi_{nk_0}|\,\hat{p}\,|\phi_{n'k_0}\rangle\,. \tag{2.30}$$

The numerical calculation and obtained values of this transition matrix element are described in Chapter 3. Since the Bloch states are defined without the presence of the field, and therefore do not dependent explicitly on time, we refer to this basis as the 'field-free' basis. The interaction of the solid with the laser in the field-free basis corresponds to the interaction with many independent n-level systems, see Fig. 2.6a. To simulate the band structure, each two-level system is solved for a slightly different energy gap [99]. The interaction leads to a driven current in each momentum channel k_0, which can be calculated using,

$$\begin{aligned} j_{k_0}(t) &= -[\langle\Psi_{k_0}(t)|\,\hat{p}\,|\Psi_{k_0}(t)\rangle + A(t)] \\ &= -[\mathfrak{Re}[\sum_{n,n'} C^*_{nk_0}(t)C_{n'k_0}(t)p_{k_0}^{nn'}] + A(t)]. \end{aligned} \tag{2.31}$$

The total current is retrieved by adding up all momentum contributions along the Brillouin zone,

$$\mathbf{J}_{\text{total}}(t) = \int_{k_0\in BZ} j_{k_0}(t)\,dk_0. \tag{2.32}$$

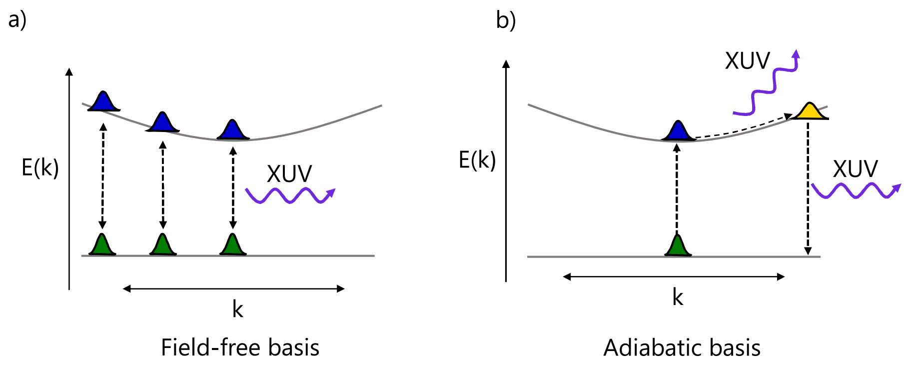

Figure 2.6: a) In the field-free basis, the interaction corresponds to population exchange between many independent two-level systems. b) In the adiabatic basis, the carriers propagate along k, before recombination, such that interband and intraband contributions can be calculated separately.

The total current rapidly oscillates, which leads to the generation of high-harmonics. The spectral components of the harmonic emission can be computed by Fourier transformation of the total current, see Fig. 2.7. The spectrum shows clearly resolved low-order harmonics below the bandgap, followed by a plateau region of the harmonics extending to the cutoff. The disadvantage of solving the interaction in the field-free basis, is that we are not able to discriminate between separate contributions to the harmonic signal, but can only compute the total harmonic signal.

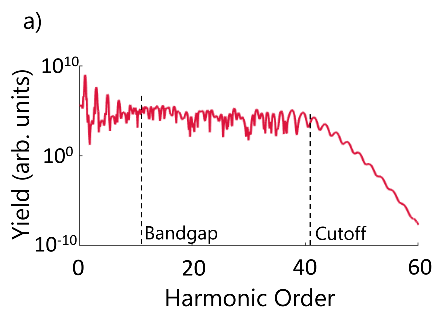

Figure 2.7: a) Harmonic spectrum calculated using the field-free basis.

2.3.2. Adiabatic basis and Houston states

In order to identify the different harmonic emission mechanisms, we simulate the interaction in a time-dependent adiabatic basis, see Fig. 2.6b. As the electron interacts with the laser field, it is driven along the energy band, such that the momentum becomes time-dependent, $k(t) = k_0 + A(t)$, which is equivalent to the momentum evolution described in the semiclassical approach. The result of the time-dependent momentum is that the eigenstates of the Hamiltonian will also become time-dependent,

$$H(t)\,|\phi_n(t)\rangle = E_n(t)\,|\phi_n(t)\rangle\,, \tag{2.33}$$

in which $|\phi_n(t)\rangle$ is the adiabatic eigenstate, better known as the Houston state [100], with the corresponding eigenvalue $E_n(t)$. Instead of a fixed energy value, the eigenvalues become time-dependent and correspond to the band energy at a given time t. A general example, based on the results presented in [87], of time-dependent eigenvalues is shown in Fig. 2.8a. The energy level of the valence and conduction band are set at -0.5 and 0.5 a.u., respectively. Upon interaction with the laser field (ω=0.1 a.u.), which corresponds to a few-cycle femtosecond pulse, the carriers are accelerated inside the energy bands, resulting in a time-dependent eigenvalue for the corresponding band.

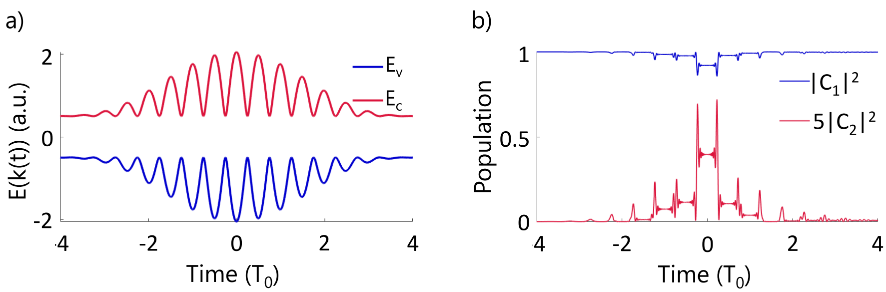

Figure 2.8: a) Energy eigenvalues of the adiabatic Houston states, for a valence and a conduction band. b) Population in valence and conduction band.

The wave function in the adiabatic basis, for an initial momentum k_0, becomes

$$|\Psi(t)\rangle = \sum_n a_{nk_0}(t)\,|\phi_{nk_0}(t)\rangle\,, \tag{2.34}$$

with the coefficients $a_{nk_0}(t)$ related to the population of level n. To calculate the time-dependent population in each band, we solve for the coefficients using,

$$i\frac{\partial a_{nk_0}}{\partial t} = \sum_{n'}[E_n(k(t))\delta_{nn'} - F(t)X_{nn'}(k(t))]\,a_{n'k_0}. \tag{2.35}$$

The coupling strength between two levels n and n' is now given by the time-dependent transition matrix element, defined by

$$X_{nn'}(t) = i\frac{\langle\phi_n(t)|\,\hat{p}\,|\phi_{n'}(t)\rangle}{E_n(t) - E_{n'}(t)}. \tag{2.36}$$

The coupling strength within a level n is zero. By solving Eq. 2.35, we can calculate the population evolution in each level, see Fig. 2.8b. The population exchange shows two types of dynamics, which we categorize as diabatic and adiabatic processes, which are defined with respect to the time evolution of the system, which is set by the cycle time of the driving field. On one hand we observe sudden population exchange, which occurs at moments in time where the transition matrix element $X_{nn'}$ is large. The transition coupling strength is maximum at points where the energy difference between the bands is minimal, this occurs at the peak of the electric field and results in the diabatic population exchange. On the other hand, we observe that the population remains constant between the peaks of the electric field. During this time, the carriers are accelerated across the bands, such that their energy changes slowly, which is referred to as adiabatic dynamics.

Similar as for the field-free basis, the total harmonic signal originates from the rapidly oscillating current, induced by the population dynamics,

$$j(t) = \langle\Psi(t)|\,\hat{p}\,|\Psi(t)\rangle = \sum_n |a_n(t)|^2 \langle\phi_n(t)|\,\hat{p}\,|\phi_n(t)\rangle + \sum_{n,n'} a_n^*(t)\,a_{n'}(t)\,\langle\phi_n(t)|\,\hat{p}\,|\phi_{n'}(t)\rangle\,. \tag{2.37}$$

In the adiabatic basis, we can separate two contributions. The first term corresponds with the currents that are correlated to the population dynamics within a band, therefore referred to as *intraband* processes $j_{\mathrm{intra}}(t)$. The second term corresponds with currents that originate from the population exchange between the bands, therefore called the *interband* contribution $j_{\mathrm{inter}}(t)$. The harmonic emission generated by the interband and intraband processes are shown in Fig. 2.9a. The emission below the bandgap shows a perturbative drop in harmonic yield and is dominated by the intraband contribution. Above the bandgap, the emission originates from the interband process and extends into an emission plateau of harmonics. At the cutoff energy, the spectrum drops sharply. Figure 2.9b shows the time-dependent spectral characteristics of the HHG. The color map denotes the harmonic yield on a logarithmic scale. This analysis of the HHG emission allows to identify which energies are emitted at which time of the interaction. Two clear emission features can be identified. For energies above the bandgap (1 a.u., equivalent to HO 10), the emission shows a strong time-dependence. For a certain time in the cycle, only one energy is generated. This feature can be described by the recollision-type generation mechanism, for which the emitted energy corresponds to the energy gap at a given time. For confirmation, the time-dependent bandgap, corresponding to the difference in eigenvalues between the valence and the conduction band, is also shown in Fig. 2.9b as the white line, and traces out the emission features. In addition, we observe that twice in each half-cycle the same harmonic energy is emitted, which can be identified as the presence of short and long trajectories [101]. The other emission feature is related to the below bandgap harmonics, which shows no time dependence. We perform the same analysis for the intraband and interband contributions separately, see Fig. 2.9c,d, respectively. Indeed, the intraband contribution dominates the below bandgap emission, and shows no time-dependent emission profile. From Fig. 2.9d we observe that the interband contributions are clearly responsible for the recollision-type emission features above the bandgap. Below the bandgap, no time-dependence is vis-

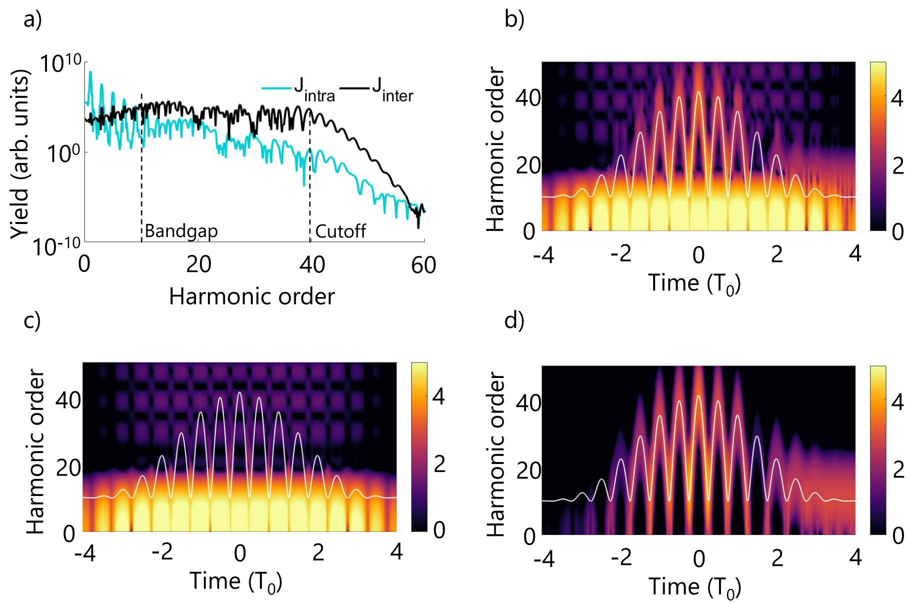

Figure 2.9: a) Intraband and interband contributions of the harmonic spectrum, calculated using the Houston states. b) Spectrogram of the total current, c) the intraband contributions, and d) the interband contributions. The color axis represents harmonic yield on a logarithmic scale.

ible, and the harmonics are emitted in phase with the electric field. For clarification, both the intraband and interband contributions themselves can be induced by different mechanisms. In analogy with the semiclassical description, the current induced by the change in population of a certain level $|a_n(t)|^2$, due to strong-field ionization can be identified as Brunel harmonics. Under the assumption that the population within a band does not change, the velocity of the carriers, contained in the term $\langle \phi_n(t)|\,\hat{p}\,|\phi_n(t)\rangle$, relates to velocity harmonics. The interband term is directly related to the population exchange between the bands, $a_n^*(t)a_{n'}(t)$, which can be identified as the recollision mechanism. Additionally, the build up of polarization between the bands, induced by the excitation of carriers, will contribute to both the intraband and interband emission.

Overall, the adiabatic basis provides a method to separate interband and intraband contributions, and to investigate the spectral and temporal features of the harmonic emission. However, these features as described above strongly depend on the intensity of the driving field. As presented in [87], at high intensities the spectral shape of the harmonic emission changes drastically. Due to the large force on the electron, it will accelerate across the first edge of the Brillouin zone, and will undergo a Bloch oscillation. As a result, the population exchange changes very rapidly, which blurs out the harmonic features in the emission profile. This phenomena can be understood in the context of crossing Wannier-Stark states, and is described in the following section.

2.3.3. Dressed states: Floquet & Wannier-Stark

Another way to think about the strong light-matter interaction, is in the context of light-dressed states. In the quantum mechanical framework, the electron wave function becomes 'dressed' upon interaction with light inside a periodic potential, associated with the Floquet picture. The dressed electronic wave function corresponds with a Floquet-Bloch [102, 103] state, which leads to photon-dressed energy bands. In other words, as the electron is accelerated inside an energy band, extra energy bands emerge, which are separated from the original energy band by the fundamental photon energy. The electron wave function is fully delocalized in this definition, and spreads out throughout the crystal.

As described in the previous section, as the intensity of the light field increases, the electron is driven across the edge of the Brillouin zone. In real space, the crossing of the edge resembles a Bragg-like reflection [100] and subsequently the wave function becomes localized [104, 105]. As an example, we take a look at the one-dimensional interaction of a valence and a conduction band, described in the Floquet picture. To simulate the interaction we follow the approach as described in [106]. The Hamiltonian describing this system, in the length-gauge formalism is

$$\mathscr{H}(t) = \begin{bmatrix} E_v(k(t)) & -F_0\mu \\ -F_0\mu^* & E_c(k(t)) \end{bmatrix} \tag{2.38}$$

in which $E_\lambda(k(t))$ describes the energy dispersion of band λ as a function of time-dependent momentum. The interaction between the energy bands is described by the term $F_0\mu$, which relates to the field strength F_0 and the dipole moment μ, as defined in the length-gauge. In a static field, the momentum changes linearly with time, $k(t) = k(t=0) + Ft$. Therefore the Hamiltonian becomes periodic in time, and can be written up as a Fourier series,

$$\mathscr{H}(t) = \sum_n e^{-in\omega_B t}\,\tilde{\mathscr{H}}^n, \quad \tilde{\mathscr{H}}^n \equiv \begin{bmatrix} \tilde{\epsilon_v^n} & -F_0{\mu^n} \\ -F_0{\mu^{n*}} & \tilde{\epsilon_c^n} \end{bmatrix} \tag{2.39}$$

in which $\tilde{\epsilon_\lambda^n}$ denotes the Fourier component of the energy band λ, similar to the components in Eq. 2.12, and ω_B represents the Bloch frequency. The transition dipole between states are given by the Fourier components μ^n. Next, we solve the eigenvalue problem [106]

$$\sum_{\nu',n'} (\mathscr{H}_{\nu\nu'}^{n-n'} - n\omega_B\delta_{\nu\nu'}\delta^{nn'})\,|\phi_\nu^n\rangle = \epsilon_\nu^n\,|\phi_\nu^n\rangle \tag{2.40}$$

and obtain the eigenenergies ϵ_ν^n of the eigenstates $|\phi_\nu^n\rangle$, which are Wannier-Stark states [107]. Instead of being dressed by the fundamental photon energy, the Wannier-Stark states are dressed by the Bloch frequency and form a Wannier-Stark ladder, see Fig. 2.10a. This figure shows two Wannier-Stark ladders represented in a coordinate picture, one for the conduction band (red lines) and one for the valence band (blue lines). The Wannier-Stark ladder is built up from Wannier states at each lattice site n, which are separated in energy by the Bloch frequency $\omega_B = aF_0$, which depends on the field strength F_0 and

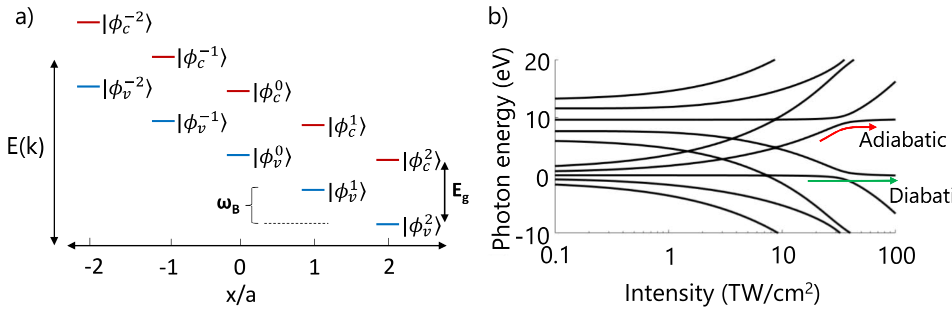

Figure 2.10: a) Wannier-Stark ladder, showing the Wannier states for the conduction (red) and valence (blue) band. b) Intensity dependent eigenvalues of the Wannier-Stark states, showing avoided crossings (diabatic transitions) between states for high intensities.

the lattice constant a. The two ladders are separated by the band gap energy E_g. The coefficients $\tilde{\epsilon}_\lambda^n$ relate to the coupling strength between the nth neighbouring site. The amount of states within a ladder resembles over how many lattice sites the electronic wave function is defined. In this example, each WS ladder is described for the nearest $n = \pm 1$ and next-nearest $n = \pm 2$ neighbour.

The eigenenergies of both Wannier-Stark ladders are shown as a function of the intensity in Fig. 2.10b. The energy levels of the valence and conduction band $\tilde{\epsilon}_\lambda^0$ are set at 0 and 9.6 eV, respectively. The coupling to the nearest neighbour $n = 1$, relates to the width of band λ and is set to $\tilde{\epsilon}_c^1 = 2$ eV and $\tilde{\epsilon}_v^1 = 0.67$ eV. As the intensity increases, the difference between eigenvalues within the same Wannier-Stark ladder becomes larger and the two Wannier-Stark ladders start to overlap. The states between two Wannier-Stark ladders form avoided crossings, at which population transfer between the conduction and valence band occurs through diabatic transitions (denoted by the green arrow). The population transfer described by these diabatic transitions can be described by Zener tunneling [106]. In addition, population that remains within the same Wannier-Stark state can change energy through adiabatic dynamics (denoted by the red arrow). The population transfer results in the emission of high energy photons [106], where the emitted energy is given by the separation between Wannier states $\epsilon_\nu^n - \epsilon_{\nu'}^{n'}$. As the separation of states is defined by the Bloch frequency, Wannier-Stark localization can be used to explain the experimentally observed linear scaling in the cutoff energy with respect to the field strength F_0, which corresponds to a quadratic dependence to the intensity, see Fig. 2.10b.

2.3.4. Semiconductor Bloch equations

Simulating HHG using Bloch states, Houston states, or Wannier-Stark states allows to identify the main characteristics of solid harmonic generation. However, the previously described models have in common that they do not take into account the dephasing of the coherence between the carriers, which originates from elastic or inelastic scattering with other electrons, impurities, or phonons [108]. Therefore, we model the generation of high-harmonics from silica, by solving the semiconductor Bloch equations [35, 37, 109] for a three-level system, consisting of one valence band and two conduction bands, for an 800-nm pulse. In the following equations we refer to the valence and the two conduction bands as h_1, e_1, and e_2, respectively. The additional advantage of the semiconductor Bloch equations is that it solves directly at which position in k-space the carriers are located as a function of time, such that the behaviour of the carrier dynamics is more transparent and easier to identify. The system of coupled differential equations are solved for the momentum k dependent population f_k^{λ} in band λ and the polarization $p_k^{\lambda\lambda'}$ between bands λ and λ', and is written out for bands $\lambda \in \{h_1, e_1, e_2\}$ as:

$$\begin{aligned} i\frac{\partial}{\partial t}p_k^{h_1e_1} = (E_k^{e_1} + E_k^{h_1} - i\frac{1}{T_2})p_k^{h_1e_1} - (1 - f_k^{e_1} - f_k^{h_1})d_k^{e_1h_1}F(t) \\ + iF(t)\cdot\nabla_k p_k^{h_1e_1} + F(t)[d_k^{e_2h_1}p_k^{e_2e_1} - d_k^{e_1e_2}p_k^{h_1e_2}] \end{aligned} \tag{2.41}$$

$$\begin{aligned} i\frac{\partial}{\partial t}p_k^{h_1e_2} = (E_k^{e_2} + E_k^{h_1} - i\frac{1}{T_2})p_k^{h_1e_2} - (1 - f_k^{e_2} - f_k^{h_1})d_k^{e_2h_1}F(t) \\ + iF(t)\cdot\nabla_k p_k^{h_1e_2} + F(t)[d_k^{e_1h_1}p_k^{e_2e_1} - d_k^{e_1e_2}p_k^{h_1e_1}] \end{aligned} \tag{2.42}$$

$$\begin{aligned} i\frac{\partial}{\partial t}p_k^{e_1e_2} = (E_k^{e_2} - E_k^{e_1} - i\frac{1}{T_2})p_k^{e_1e_2} + (f_k^{e_2} - f_k^{e_1})d_k^{e_2e_1}F(t) \\ + iF(t)\cdot\nabla_k p_k^{e_1e_2} + F(t)[d_k^{e_1h_1}p_k^{e_2h_1} - d_k^{h_1e_2}(p_k^{h_1e_1})^*] \end{aligned} \tag{2.43}$$

$$\frac{\partial}{\partial t}f_k^{e_1} = -2\,\mathrm{Im}[d_k^{e_1e_2}F(t)(p_k^{e_2e_1})^* + d_k^{e_1h_1}F(t)(p_k^{h_1e_1})^*] + F(t)\cdot\nabla_k f_k^{e_1}. \tag{2.44}$$

$$\frac{\partial}{\partial t}f_k^{e_2} = -2\,\mathrm{Im}[d_k^{e_2e_1}F(t)(p_k^{e_1e_2})^* + d_k^{e_2h_1}F(t)(p_k^{h_1e_2})^*] + F(t)\cdot\nabla_k f_k^{e_2}. \tag{2.45}$$

$$\frac{\partial}{\partial t}f_k^{h_1} = -2\,\mathrm{Im}[d_k^{e_1h_1}F(t)(p_k^{h_1e_1})^* + d_k^{e_2h_1}F(t)(p_k^{h_1e_2})^*] + F(t)\cdot\nabla_k f_k^{h_1}. \tag{2.46}$$

in which, the single particle energies of the carriers in band λ are given by E_k^{λ}. The creation of polarization and population due to the presence of an electric field $F(t)$ follows from the terms that involve the transition dipole moment $d_k^{\lambda\lambda'}$. The intraband dynamics, caused by carrier acceleration by $F(t)$ within the bands, are described by the terms including ∇_k. The dephasing time of the polarization is denoted by T_2. The transition dipole moment $d_k^{\lambda\lambda'}$ between the bands λ and λ' is approximated in first order $\mathbf{k}\cdot\mathbf{p}$ theory [110] as

$$d_k^{\lambda\lambda'} = d_0^{\lambda\lambda'}\frac{E_g^{\lambda\lambda'}}{E_k^{\lambda} - E_k^{\lambda'}}, \tag{2.47}$$

where $d_0^{\lambda\lambda'}$ resembles the transition dipole moment between bands λ and λ' at the Γ-

point, and $E_g^{\lambda\lambda'}$ the bandgap energy at the Γ-point between bands λ and λ'. The amplitude of the transition dipole moments is calculated as described in Chapter 3, and is directly correlated to the coupling strength between two different bands. Since the transition dipole moment varies in amplitude for different combinations of bands, the transitions and carrier dynamics between and within these bands also vary. The semiconductor Bloch equations are cast as a set of coupled partial differential equations with periodic boundaries. To solve this numerical problem, the k-dimension of the equations are represented in a Fourier-series base and then solved by using spectral methods, as provided through the Dedalus project [111].

The macroscopic polarization $P(t)$ and macroscopic current $J(t)$ are calculated [35] by

$$P(t) = \sum_{\lambda,\lambda',k} [d_k^{\lambda\lambda'} p_k^{\lambda\lambda'} + c.c.] \tag{2.48}$$

$$J(t) = \sum_{\lambda,k} v^{\lambda}(k) f_k^{\lambda} \tag{2.49}$$

with the group velocity $v^{\lambda}(k)$ given by

$$v^{\lambda}(k) = \nabla_k E_k^{\lambda}. \tag{2.50}$$

The interband polarization and the intraband current are equivalent to the interband and intraband processes, as described in the adiabatic basis previously. We calculate the spectral representation of the source field of interband polarization as follows

$$F_{\text{inter}}(\omega) = \mathscr{F}\left[\frac{\partial}{\partial t} j_{\text{inter}}(t)\right] = \mathscr{F}\left[\frac{\partial^2}{\partial^2 t} P(t)\right] = \omega^2 \mathscr{F}[P(t)] = \omega^2 P(\omega). \tag{2.51}$$

and the intraband current as

$$F_{\text{intra}}(\omega) = \mathscr{F}\left[\frac{\partial}{\partial t} j_{\text{intra}}(t)\right] = i\omega \mathscr{F}[J(t)] = i\omega J(\omega). \tag{2.52}$$

The total harmonic spectral density at the sample plane is defined by both contributions,

$$I_{\text{HHG}}(\omega) = |\omega^2 P(\omega) + i\omega J(\omega)|^2. \tag{2.53}$$

The spectral components of the interband polarization and intraband current are shown in Fig. 2.11. We observe that the interband polarization dominates the emission above the bandgap, and that the intraband current is most efficient below the bandgap. Both the interband polarization and intraband current show a perturbative trend for the low-order below bandgap harmonics. In more detail we look at the carrier and polarization dynamics in time and momentum space, see Fig. 2.12a,b, respectively. As time evolves, the population of electrons in the first conduction band grows with each half-cycle,

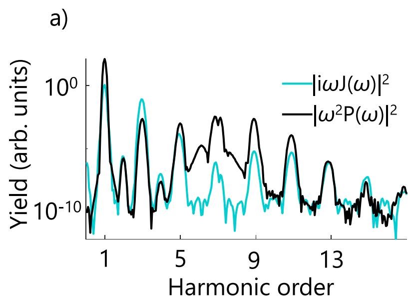

Figure 2.11: a) The spectral components of the intraband current and interband polarization calculated using the semiconductor Bloch equations.

which is denoted by the change in color, which represents the population density. We can observe from the same figure, that the electric field drives the carriers within the band along the momentum axis. These oscillations are in phase with the vector potential (the magenta line in Fig. 2.12a), which is equivalent to the time-dependent momentum picture presented earlier on. For the polarization growth, shown in Fig. 2.12b, we conclude that the trend is dictated by the electric field (the white line in Fig. 2.12b). Additionally, the polarization is the largest for values of the momentum surrounding the bandgap ($k = 0$). Next, we look at the spectral components for each momentum channel k, see Figs. 2.12c,d. The spectral components of the intraband current, clearly show that no emission is present at the bandgap. As the curvature of the band is flat around the bandgap, indeed no emission is expected. The main emission of the intraband current dominates the below bandgap region. The standing oscillation features along k, for each harmonic, are associated with Bloch frequencies, originating from the carrier excursion beyond the Brillouin zone edge. The polarization shows similar features, see Fig. 2.12d. The main emission originates from above bandgap harmonics.

2.4. Macroscopic properties

The previous theoretical background has described in detail how the microscopic high-harmonic generation is calculated. In an experimental setting, the macroscopic quantities of the high-harmonic generation are measured. This section describes how to obtain the macroscopic properties and how to take into account the spatial properties of the harmonic radiation, to reproduce an experimental setting.

2.4.1. Gaussian beams and interference

In addition to the temporal characteristics of a femtosecond pulse, described previously in Eq. 2.1, we need to describe the spatial properties, which we define as,

$$F(x,y,z) = F_0(x,y,z)e^{-i(kz+\frac{k(x^2+y^2)}{2R(z)}-\zeta(z))} \tag{2.54}$$

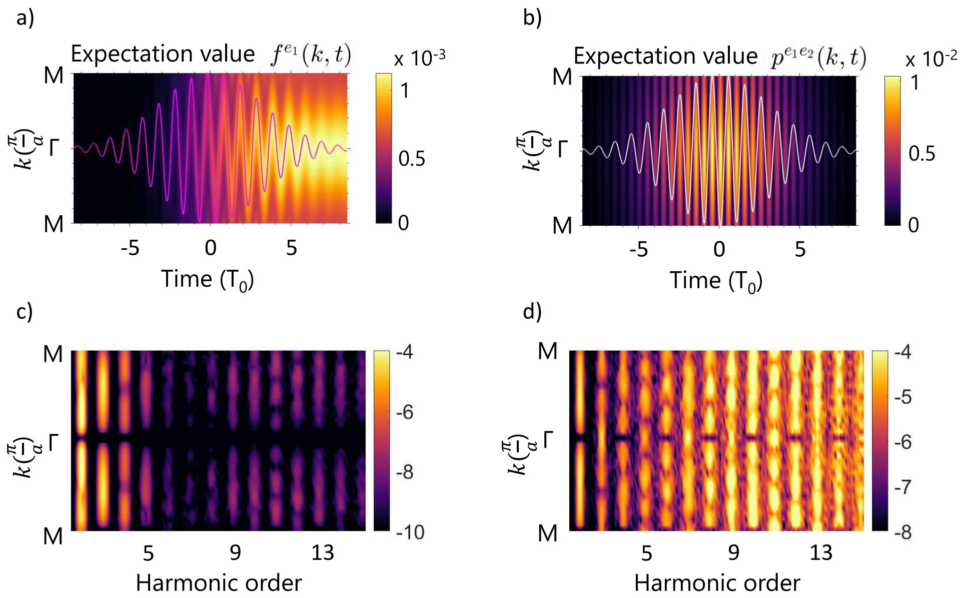

Figure 2.12: a) Conduction band population in momentum and time. The vector potential of the electric field is shown as the magenta line. b) Microscopic polarization in momentum and time. The electric field is represented by the white line. c) Spectral components of the intraband current for each momentum k. The color axis represents harmonic yield on a logarithmic scale. d) Spectral components of the interband polarization for each momentum k. The color axis represents harmonic yield on a logarithmic scale.

with the spatial envelope $F_0(x,y,z)$, which corresponds with a Gaussian envelope, and a phase term, which consists of three contributions. As the pulse propagates along z, the plane wave component will accumulate a phase, set by the wave vector $k = \omega/c$. The second term determines the parabolic curved wavefront, which originates from the propagation associated with a radius of curvature $R(z)$. The last term corresponds to the Gouy phase, which is given by the offset between the plane wave and the parabolic waves. In the focus we assume no wave front curvature and are left with a plane wave.

In the experiments described in Chapter 6 and 7, we use multiple beams, which we cross non-collinearly in focus. The interference between the two beams results in an oscillating total electric field along the sample plane. In order to correctly calculate the generation of the harmonics, we have to determine the total electric field for each position in the sample. The crossing angle β induces a phase factor between the interfering field, which depends on the position x as $\phi(x) \approx x\sin(\beta)$. As an example we take the configuration used in Chapter 6, where an 800-nm beam and a 400-nm beam cross at the sample plane, see Fig. 2.13. Along the x direction interference occurs, which results in a modulated intensity distribution at the sample plane, see Fig. 2.13b. In Chapter 7, two 266-nm beams are crossed at the sample plane, and form a standing grating. The spatial features of this grating are described in more detail in the corresponding chapter.

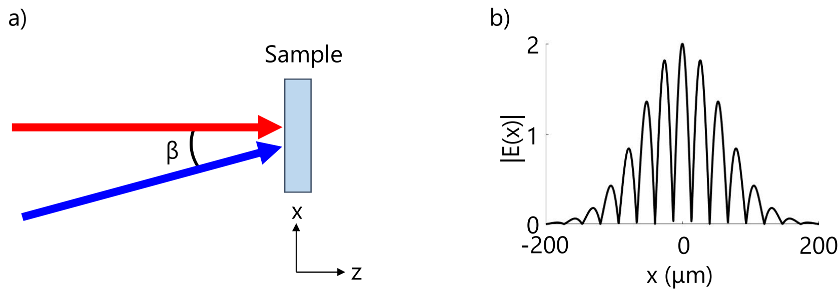

Figure 2.13: a) Non-collinear configuration, two beams with crossing angle β lead to an interference pattern in the sample plane, as shown in b).

2.4.2. Diffraction

The spatial properties of the harmonic radiation at the sample plane determine the features of HHG during detection, which takes place in the far-field. The far-field profile of the harmonic radiation can be computed by Fraunhofer diffraction, which corresponds to a Fourier transform of the harmonic wave at the sample plane:

$$\mathscr{F}[F_{\mathrm{HHG}}(x_{SP},\omega)] \propto F_{\mathrm{HHG}}(x_{FF},\omega). \tag{2.55}$$

The Fraunhofer diffraction is appropriate to use, if the wavefront has propagated over far enough distance, which can be determined by the Fresnel number,

$$F = \frac{a^2}{L\lambda} \tag{2.56}$$

in which a corresponds with the size of the object, L relates to the propagated distance and λ the wavelength of the light. For the regime, at which the propagation distance is much larger than the object size, the Fresnel number becomes much smaller than 1, and Fraunhofer diffraction can be used to approximate the diffraction. In the case that the propagation distance is on the order of the size of the object, we have to use Fresnel theory to calculate the diffraction of the wavefront. For example, as shown in more detail in Chapter 5 and Chapter 7, a structure can imprint a phase grating onto the fundamental wavefront. As the fundamental wave then propagates through the 100 µm sample, we are still in the Fresnel diffraction regime, which leads to modulation of the wavefront. We refer to this regime as near-field diffraction, which is equivalent to the regime in which high-harmonic generation occurs.

2.4.3. Phase matching

The total harmonic signal in gas-based HHG originates from many gas atoms, the emitters, that are distributed across space. The associated generated harmonic fields interfere with each other. To achieve a maximal harmonic signal, the emission of all gas atoms has to constructively interfere, a process we refer to as phase matching [112–115]. The phase mismatch between the emitters can be written as $\Delta k_q = \Delta k_g + \Delta k_n + \Delta k_p + \Delta k_d$, and depends on four significant contributions. The first term Δk_g relates to the phase mismatch introduced by the Gouy phase. The second term Δk_n originates from any phase delay introduced by the dispersion of the neutral medium, which is related to the gas pressure and the refractive index mismatch between the fundamental driver and the HHG. The third term Δk_p corresponds to a phase mismatch introduced by the free-electron plasma dispersion that is created during the HHG process, since the gas becomes ionized during the process. The last term Δk_d relates to the dipole phase that the electrons accumulate during the propagation step, which is different for each harmonic order and their corresponding long and short trajectories, and is dependent on the field intensity. The position of the gas jet, the intensity of the driving pulse, and the pressure of the gas are all control parameters in the process of optimizing phase matching. Since the dipole phase is different for short and long trajectories, one of these trajectories can be phase-matched accordingly to one's liking [116].

The photon energies that are generated during solid-state HHG, as experimentally presented in this thesis which focuses on XUV generation, are associated with a very short absorption length inside the materials (SiO_2 and MgO) used for generation [117, 118]. Due to the short XUV emission volume, no destructive or constructive interference can take place, such that we can neglect phase matching effects in solid HHG.

3
Methods

3.1. Laser source

The femtosecond light pulses used in the experiments described in this thesis are generated using a commercially available Ti-Sapphire amplified laser system (Astrella, *Coherent*). The Astrella can be described by three main components: the *Vitara*, which generates the seed pulses, the *Revolution*, which generates the pump pulses, and the regenerative amplifier, which generates the final output pulses.

The *Vitara* femtosecond oscillator produces pulses with a central wavelength of 815 nm with a bandwidth of 60 nm at FWHM at 80 MHz repetition rate. The oscillator is pumped by an integrated *Verdi-G* diode-pumped laser, which generates about 4.5 W power at an operating current of 27 A. The *Vitara* modelocked power is 600 mW, of which half is used to seed the Astrella cavity. To prevent optical damage to the Ti:Sapphire crystal, while amplifying the seed pulses from the nJ to the mJ level, the seed pulses are stretched in time using a grating stretcher to lower the peak intensity of the pulses during the amplification process, a technique known as chirped pulse amplification [5]. The pulses are coupled into the regenerative amplifier, of which the design resembles an optical cavity, at a repetition rate of 1 kHz using a Pockels cell. Subsequently the pulses are amplified in a Ti:Sapphire crystal, which is pumped by the *Revolution*. This pump-laser provides pulses at a central wavelength of 532 nm, an average power of 35 W, at an operating current of 21.3 A, at 1 kHz repetition rate. The pulses make 13 round trips in the regenerative amplifier, before being coupled out by another Pockels cell. Subsequently the pulses are compressed in time using a grating compressor. After the grating compressor, the pulses have a central wavelength of about 800 nm, a bandwidth of 35 nm, with a total average power of 7 W at 1 kHz repetition rate. The bandwidth of the pulses allows for a 35-fs pulse length, if no higher-order dispersion is present. The characterization of the pulse length is performed by a home-built second-harmonic generation frequency-resolved optical gating (FROG) setup, using a 100 μm β-Barium Borate (BBO) (Castech) to generate the second-harmonic signal at around 400 nm. An experimental trace is presented in Fig. 3.1a, which was reconstructed (Fig. 3.1b) to obtain the spectral shape and phase (Fig. 3.1c) and electric field and temporal phase (Fig. 3.1d). The

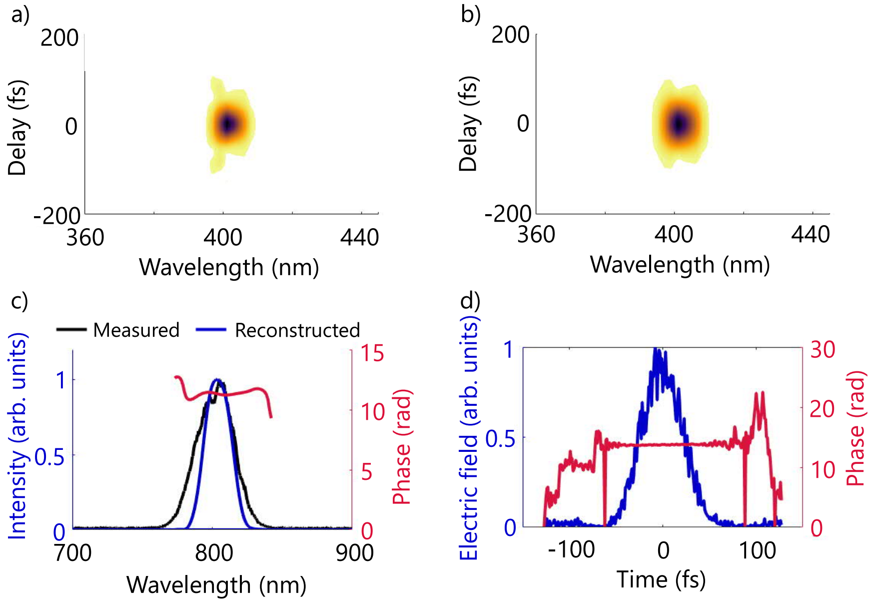

Figure 3.1: a) Experimental FROG trace. b) Reconstructed FROG trace. c) Reconstructed spectral intensity (blue) and phase (red). d) Reconstructed electric field amplitude (blue) and temporal phase (red).

reconstructed pulse length at FWHM is about 45 fs, with a reconstructed bandwidth of 20.9 nm. As can be seen in Fig. 3.1c, the reconstructed bandwidth is narrower than the measured bandwidth of 32 nm. Due to phase matching, the β-BBO used in the FROG setup cannot frequency-double all spectral components with the same efficiency, which will therefore narrow the spectral bandwidth, which is translated into a narrower reconstructed fundamental spectrum. Due to this spectral narrowing, the reconstructed pulse duration is an upper limit of the actual pulse duration.

3.2. High-harmonic generation setup

The general layout of the high-harmonic generation setup is shown in Fig. 3.2. The driving pulse is reflected with a flat mirror onto a spherical mirror, that focuses the pulses inside the center of the HHG chamber. Depending on the experiment, the incoming pulses might consist of multi-color pulses, of which the setup is described in the corresponding chapter. In general, the spherical mirror has a silver coating and a 75-cm focal length. In the center of the HHG chamber, the generation medium is positioned, which is either a gas or a solid. A manual three dimensional translation stage allows for precise positioning of the generation medium to the desired position. Subsequently, the generated harmonics and remaining fundamental pulses propagate through a differential pumping tube towards the detection chamber. The harmonics are spectrally dispersed with an aberration-corrected, concave, flat-field grating (1200 lines/mm, Shimazu model 30-002), and are detected by a double-stack microchannel plate (MCP, *Photonis*) assembly. This geometry serves as a far-field spectrometer, where the spectrum is dispersed in the horizontal plane, and the beam freely propagates in the vertical direction. The phosphor screen is imaged with a camera, positioned outside the vacuum setup. Images are recorded and subsequent data analysis is performed.

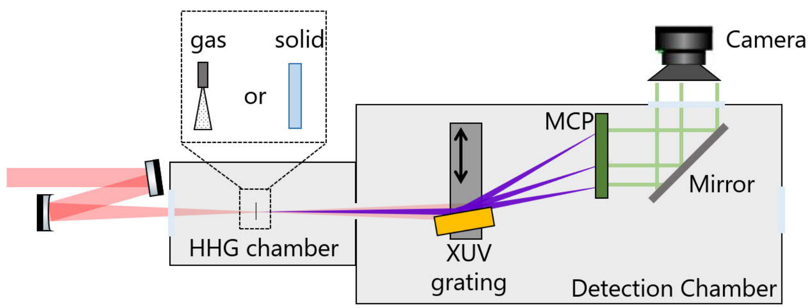

Figure 3.2: General layout of the high-harmonic generation setup. The infrared laser pulses are focused onto the generation medium (either a gas or a solid), positioned in the center of the HHG chamber. After the generation, the XUV and the fundamental infrared pulses propagate to the detection chamber, where they are dispersed by an XUV grating and detected using a multi channel plate (MCP) assembly.

The experimental generation conditions, such as beam size and pulse energy, vary for the generation of harmonics from gases and solids. More specifically, the peak intensity of the pulses in gas HHG lies around 2 10^{14} W/cm^2, whereas the peak intensity inside the solid sample has to stay below a few 10^{13} W/cm^2, in order to prevent damage to the samples. Due to the lower intensity in solid HHG, in general, the signal of the generated harmonics is also lower. Additionally, the XUV grating that is used to refocus the harmonics onto the MCP, is specified for short wavelengths (5 nm - 20 nm), such that in the plane of the MCP the lower harmonics (H5-H11, 160 nm - 72 nm) are not focused properly, which reduces the signal-to-noise. To compensate for the lower signal level, the voltage between the MCP plates is increased from 1.6 kV to 2.3 kV, with the phosphor screen set at 3 kV above the voltage applied to the MCP plates. The disadvantage of the high applied voltage onto the MCP, is that other charged particles (electrons and ions) increase the background noise significantly, reducing again the signal-to-noise. The background signal is the lowest in the case that we apply a positive voltage between the front and back MCP plate, which allows to only measure negatively charged particles, in addition to the XUV photons, indicating that ions are the main source of the background signal.

3.3. Material parameters for simulations

To simulate the strong-field light-matter interaction that generates high harmonics, one needs to know the material parameters of the solid-state sample that is used for the generation. These parameters resemble: the energy levels of the bands, the dispersion of the bands, the dipole coupling strength between the bands, and the lattice parameters along the used symmetry direction of the material of interest. All these parameters are determined by the properties of the many electron wave functions that build up the material. In this thesis, the energy bands and the dipole coupling between the bands are calculated within density functional theory, which uses functionals of the electron density instead of wave functions to calculate the electronic structure. In particular, we use pseudopotentials and a plane-wave basis set as implemented in Quantum Espresso (QE) [119].

The first step in determining the energy bands and the dipole couplings is to perform a self-consistent field (scf) calculation, using the pw.x executable, from the Plane-Wave scf (PWscf) package provided by QE. The crystal structure, lattice parameters, pseudopotentials of the atoms, and positions of the atoms that build up the unit cell of the solid, are input parameters. The scf calculation has to be tested for convergence, specifically the plane-wave cutoff (variable 'ecutwfc') and the grid of k points have to be chosen such that the total energy converges. The next step is to use the output of the scf calculation as input for the band calculation, again using the pw.x executable. The eigenvalues of the energy bands are calculated for each k point that is specified. In order to calculate the energy dispersion along a symmetry direction, the k-points have to be chosen accordingly to the crystal symmetry. Finally, the output of the band calculation is post-processed using the bands.x executable from the Post-Processing (PP) package, provided by QE.

The last parameter that needs to be calculated before we can simulate HHG is the transition dipole moment between the bands. We approximate the k-dependence of the transition dipole moment $d_k^{\lambda\lambda'}$ between the bands λ and λ' in first order $\mathbf{k}\cdot\mathbf{p}$ theory [110] as

$$d_k^{\lambda\lambda'} = d_0^{\lambda\lambda'} \frac{E_g^{\lambda\lambda'}}{E_k^{\lambda} - E_k^{\lambda'}}, \tag{3.1}$$

where $d_0^{\lambda\lambda'}$ is the transition dipole moment between bands λ and λ' at the Γ-point, and $E_g^{\lambda\lambda'}$ the bandgap energy at the Γ-point between bands λ and λ'. Throughout this thesis, all solid-state HHG experiments are performed on either amorphous or crystalline silica (SiO_2) or crystalline Magnesium Oxide (MgO), along the crystal symmetry planes that always involve the Γ-point. Since we can calculate the energy bands along the corresponding symmetry planes using QE, we only need to determine the transition dipole moment at the Γ-point. The dipole moments are calculated using the epsilon.x executable, which is a post processing code of the PWscf package. This code can be used to calculate the real and imaginary part of the dielectric tensor, and uses the transition dipole moments between the bands to calculate this. In order to get access to these values, one needs to modify the epsilon.x executable, such that the dipole moments are printed in the output file. The epsilon.x code does not work for an automatically generated k-point grid, therefore the k points have to be written out explicitly. Additionally, the epsilon.x code requires pseudopotentials that are not Ultrasoft, which is a kind of pseudopotential that needs less planewaves to describe the pseudo-wavefunctions of the system, which is specified in the variable 'is_ultrasoft' in the header data of each pseudopotential-file. The epsilon.x code can be used after an initial scf calculation, which meets these requirements.

Silica

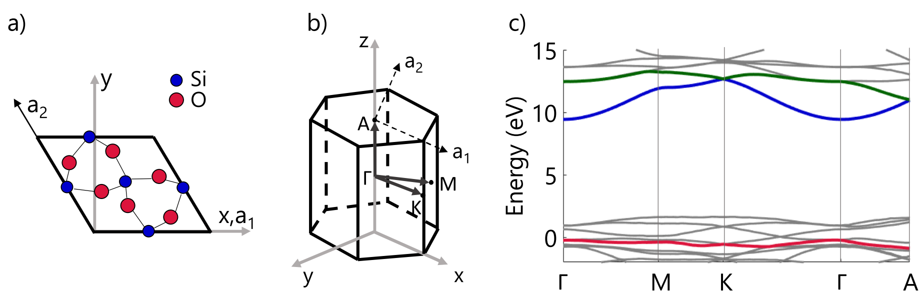

Figure 3.3: (a) Top view of the unit cell of SiO_2. b) Hexagonal crystal orientations. c) Calculated band structure of SiO_2. The strongest coupling valence band, and the two strongest coupling conduction bands are highlighted in red, blue, and green, respectively.

The energy levels and the transition dipole moments of fused silica at the Γ-point between the valence band and two conduction bands are calculated, to provide input for the semiconductor Bloch equations, described in the theoretical background, in Chapter 2. The unit cell of SiO_2, see Fig. 3.3a, is described by three basis vectors that describe an hexagonal crystal lattice, $\mathbf{v}_1$=a(1, 0, 0), $\mathbf{v}_2$=a(-1/2, $\sqrt{3}/2$, 0) and $\mathbf{v}_3$=a(0, 0, c/a), with a=8.04 Å and c/a=1.1, see Fig. 3.3b. The pseudopotentials (generalised gradient approximation in the shape of the Perdew, Burke, and Ernzerhof (PBE) functional [120]) that were used for the Si and O atoms were obtained from the QE website. The plane-wave energy cutoff used was 40 Ry. The calculation is performed for an automatically generated uniform grid of 10 points in each k direction. Both these parameters were tested for convergence. The calculated band structure along the main symmetry directions of SiO_2 is presented in Fig. 3.3c. For a simulation of high-harmonic generation, we are specifically interested in the energy bands that are strongly coupled to each other, as this will lead to the strongest interaction. In this specific band structure calculation, it is not the highest valence band that couples the strongest to the lowest lying conduction bands, but the valence band that lies four levels below the highest lying valence band, marked in red in Fig. 3.3c. Therefore we perform the calculations using the energy levels and coupling parameters between the strongest coupling valence band, and the two lowest lying conduction bands. These energy levels are calculated to be 0 eV, 9.6 eV and 12.6 eV, at k = 0, for the valence and the two lowest lying conduction bands respectively. The experimentally determined band gap of silica varies from 7.5 eV to 9.6 eV [121], which is comparable to our calculation. The dipole moments between these energy levels λ, λ' are calculated to be $d_0^{h_1 e_1} = 0.318$ a.u., $d_0^{e_1 e_2} = 0.014$ a.u. and $d_0^{e_2 h_1} = 0.037$ a.u. The calculated dipole coupling strength between the valence and the conduction band is comparable to the theoretical value of 0.37 a.u., presented in [122], which was calculated for a smaller band gap energy of about 8 eV. We model the light-matter interaction along the Γ-M crystal direction of silica, as this orientation generates the highest harmonic yield [40].

Magnesium Oxide

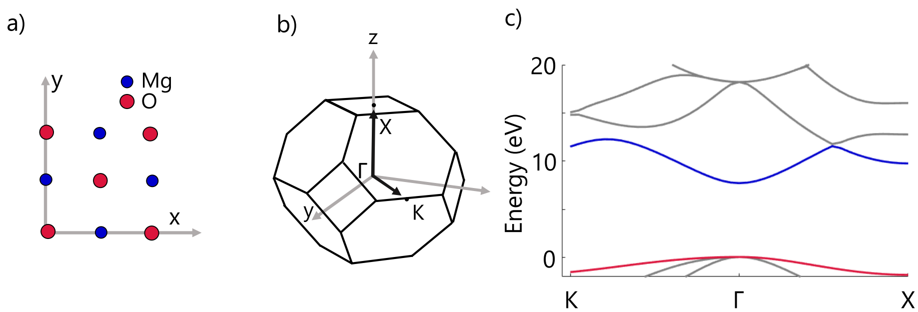

Figure 3.4: (a) Top view of the unit cell of MgO. b) FCC crystal orientations. c) Calculated band structure of MgO. The highest lying valence band and the lowest lying conduction band are highlighted in red and blue, respectively.

The unit cell of MgO, see Fig. 3.4a, is described by three basis vectors that describe a face-centered cubic (FCC) lattice, $\mathbf{v}_1$=a/2(-1, 0, 1), $\mathbf{v}_2$=(0, 1, 1) and $\mathbf{v}_3$=a/2(-1, 1, 0), with the lattice constant a=7.23 Å, see Fig. 3.4b. The pseudopotentials (generalised gradient approximation in the shape of the Perdew and Zunger functional) that were used for the Mg and O atoms are also retrieved from the QE website. The plane-wave energy cutoff used was 44 Ry. The calculation was performed on an automatic generated k-grid of 6 points along each direction. Both these parameters were tested for convergence. The calculated band structure of MgO, see Fig. 3.4c, contains much less energy bands in comparison to SiO_2. The difference originates from the fact that the unit cell of MgO only consists out of two atoms, whereas the SiO_2 unit cell is build up from nine atoms. The energy levels at the Γ-point are calculated to be 0 eV and 7.8 eV, for the highest lying valence and the lowest lying conduction band respectively. The calculated band gap energy is identical to the experimentally determined value of 7.8 eV [123]. The dipole moment between these energy levels is calculated to be 0.78 a.u. The energy levels and dipole moment are used to simulate HHG from MgO, as presented in Chapter 7.

4

Divergence and Yield Control in Two-color Gas High-Harmonic Generation

Parts of this chapter have been published in Phys. Rev. A. **13**,054029 (2020) [124] and Sci. Rep. **11**, 24253 (2021) [125]

4.1. Introduction

High-harmonic generation (HHG) is the cornerstone of attosecond science [12, 19, 126–129] and ultrafast (table-top) extreme-ultraviolet and soft-X-ray science [130] every since its discovery in 1987/1988 [13, 14]. Furthermore, applications in coherent diffractive imaging [27, 28, 131–134], spectroscopy [135–139] and metrology in industry [140–142] benefit from the short emitted wavelengths and the associated potentially high spatial resolution. All these applications would, however, benefit tremendously from higher conversion efficiencies and better focusability of the generated pulses. In particular, semiconductor wafer metrology requires microfocusing with limited energy in the wings, which would otherwise produce diffraction artifacts from metrology targets that are often embedded into an integrated-circuit infrastructure. In addition, larger divergent beams reduce the numerical aperture of an optical system.

The origins of divergence and better focusability can be understood by the intrinsic generation mechanism of HHG. Irradiation of a gas with a strong laser field leads to ionization of electrons from the parent ions. The electrons are accelerated in the continuum and accumulate an intensity-dependent phase during propagation, before they recombine with the parent ion, leading to the generation of XUV photons [15, 32, 143]. The typical Gaussian intensity distribution of the driving field in focus (Fig. 4.1a) gives rise to a double-Gaussian divergence-resolved profile [144–147], as shown in Fig. 4.1b. Each generated energy is the superposition of the contributions of two electron paths through the continuum, the short and the long trajectories. These trajectories have a unique transit time of the continuum electron, which leads to a different phase upon recombination, leading to the emission of two differently curved wavefronts and therefore the double-Gaussian profile of the harmonic beam in the far-field, as shown in Fig. 4.1c.

The nature of divergence in HHG has been understood in a number of early seminal publications. However, it only became clear very recently that the different trajectories give rise to aberrations, which hinder refocusing of the pulses from HHG to high intensities [148, 149]. This is caused by the different virtual sources of the long and short trajectories within each harmonic energy (illustrated in Fig. 4.1a), which cannot be reimaged to the same plane with a subsequent focusing element, thus diminishing the overall focusability of the beam. Thus the far-field divergence and its deviation from a mono-Gaussian profile is a signature of the focusability of the beam.

In order to increase the brightness of the HHG beam, control over the short and long trajectories is crucial, as selection of one of the two species improves the focusability. The work in this chapter builds on a number of earlier papers on two-color HHG. The second harmonic in two-color HHG introduces an additional momentum to the strong-field driven electron in the continuum. This approach has enabled the reconstruction of electron transit times [150, 151] using a weak second harmonic for both short and long trajectories [152]. Two-color HHG with a strong second harmonic [153] has enabled the selection of long or short electron trajectories by tuning the relative phase of the two-color pulses [83]. However, it remained unclear if and how much this strategy would change the divergence and how the overall conversion efficiency of the generation process would be affected. In a separate work, two-color HHG has been show to improve the flux of plateau harmonics dramatically [154]. However, in [154] the cutoff was not

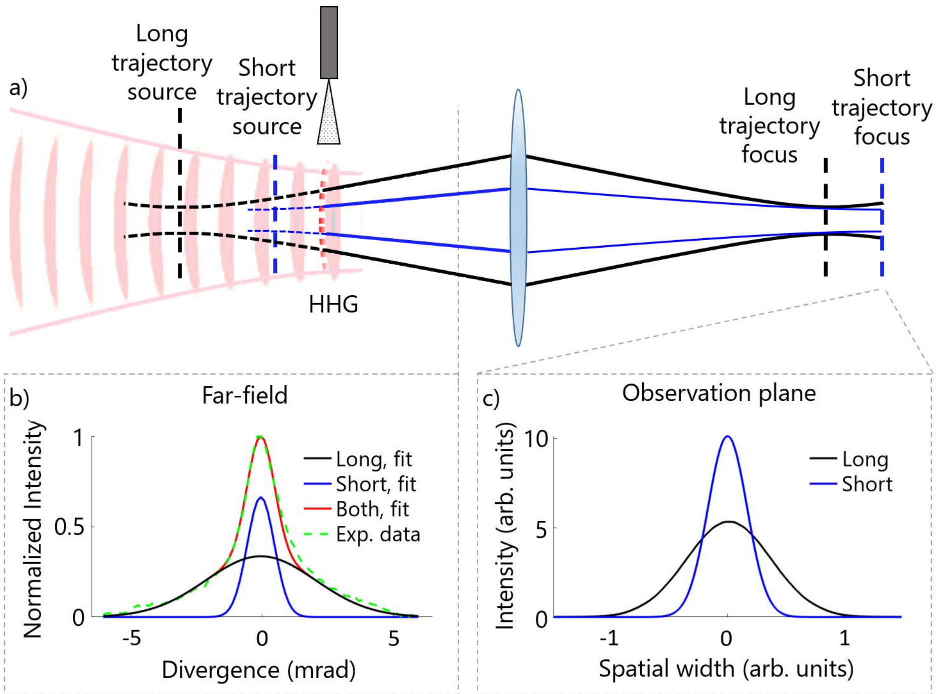

Figure 4.1: (a) Schematic representation of an HHG source and refocusing of the harmonics (a lens is shown for simplicity). For a given harmonic order q, the different contributions of the dipole phases for the short and the long trajectories give rise to different positions of the corresponding virtual sources (dashed blue and black lines). When the harmonics are refocused, the image of the long trajectories will be out of focus, leading to an overall smearing of the profile in the observation plane. (b) Experimental (green dashed line) spectrally-integrated, divergence-resolved intensity profile in the far-field, fitted with a double Gaussian distribution (red solid line), representing the contributions of short (blue line) and long (black line) trajectories, respectively. (c) Qualitative intensity distribution in the observation (focal) plane, obtained by Fraunhofer diffraction. An additional quadratic radial phase distribution was added to the profile for the long trajectories to account for the larger dipole phase of the long trajectories. This additional phase gives rise to the different divergences and virtual source positions of long and short trajectories.

detected by the spectrometer in this work, which makes any quantitative assessment of the total flux difficult. Parallel polarized multi-color fields beyond the fundamental and the second harmonic have been numerically demonstrated to simultaneously increase the yield [155] and decrease the divergence of HHG [156, 157]. Similar multi-color HHG schemes have been experimentally demonstrated to increase the HHG yield [158], as originally proposed in [159]. More recently, it has been realized that linearly and cross-polarized two-color fields with angles between fundamental and second harmonic that deviate from 0 or 90 degrees can generate elliptically and circularly polarized HHG [160–163]. These important findings motivate a systematic investigation on how yield and divergence are affected in cross-polarized two-color HHG.

In this chapter we systematically investigate both experimentally and theoretically which relative polarization configuration in two-color HHG in Argon is best suited to simultaneously optimize divergence, focusability and overall photon yield. We compare the two-color HHG spectra with a one-color configuration for the spectral range of harmonic 13 to harmonic 25. In addition to a perpendicular two-color configuration, we also generate harmonics in parallel two-color fields, and several intermediate polarization angles. By comparing experiments and simulations, we show that HHG in a two-color field can favor the emission of plateau harmonics through trajectory reshaping and selection and enhance the overall yield for specific two-color phases.

4.2. Simulated yield and trajectory contributions

This section describes the underlying concept to control divergence and yield in two-color HHG. We start of with a classical approach, followed by a more in-depth SFA simulation. The concept of the experiment is illustrated in Fig. 4.2, which shows the classically calculated long and short electron trajectories of harmonic order 15 in both a perpendicular and parallel polarized two-color laser field, for two different two-color phases. The two-color field is defined as $E(t) = E_\omega \cos(\omega t) + E_{2\omega} \cos(2\omega t + \phi_{2\omega})$, with ω the frequency of the fundamental, and where $\phi_{2\omega}$ is defined as the relative two-color phase between the fundamental and the SH. The figures also show the relative instantaneous strong-field ionization rate in the two-color field [74, 79].

Only when the field is chosen such that the electron is returning to its origin at the time of return, recombination is efficient. In a perpendicular configuration that occurs when the initial lateral velocity is compensated by the lateral displacement introduced by the second harmonic [151]. For 0 rad phase (Fig. 4.2a), the long trajectory recombines to the origin and the short trajectory misses the origin. In addition, the ionization rate is influenced significantly due to the strong SH field. In this specific case, the ionization rate at the time of birth of the short trajectory is about 1000 times lower than at the maximum of the pulse. For a phase of 0.5π rad (Fig. 4.2b), the short trajectory recombines and the long trajectory misses its ion. Moreover, the ionization rate at the time of birth of the shirt trajectory is only 400 times lower than at the maximum of the pulse. So for a perpendicular configuration, both ionization and recombination favor the short trajectory for this two-color phase. In a parallel configuration, the SH field will not be able to give a lateral momentum kick to the trajectories, but it will influence the trajectories, see Fig. 4.2c,d. For both relative two-color phases the long and short trajectories will both

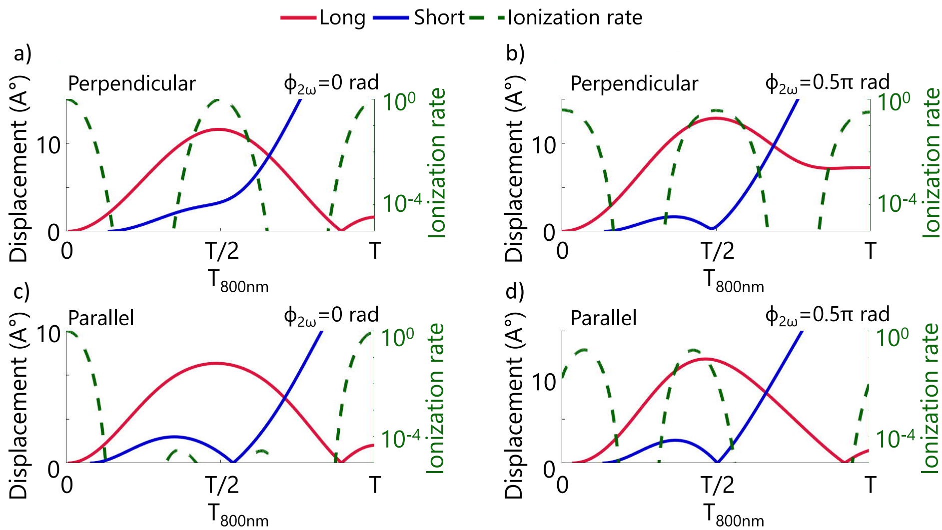

Figure 4.2: The short (blue) and long (red) trajectories for harmonic 15 as well as the two-color normalized ionization rate (green) are shown for a relative two-color phase of (a) 0 rad and (b) 0.5π rad, for a perpendicular configuration of the fields. For the same relative two-color phases of (c) 0 rad and (d) 0.5π rad for a parallel configuration.

recombine, such that trajectory selection in this configuration is not possible. Besides the trajectory selection mechanism, a change in relative strength of this ionization-rate will lead to the selection of trajectories. For example, the ionization rates for the parallel configuration vary strongly as the relative phase changes. For a relative phase of 0 rad the long trajectory has a significantly higher ionization rate than for the phase of 0.5π rad.

A more quantitative comparison is made by simulating the harmonic process in a two-color field as a single-atom response [32, 164] in Fig. 4.3, and subsequently generalized to a realistic multi-atom response by propagation computations [164] later in this chapter. Figure 4.3 shows time-frequency analyses of a single-atom simulation in a single cycle of the fundamental electric field (Fig. 4.3a) for one-color (800 nm) HHG (Fig. 4.3b), perpendicular polarized two-color HHG (Fig. 4.3c,e), and parallel polarized two-color HHG (Fig. 4.3d,f) for two different phases of the two-color field, respectively. The electric field is defined the same as for the classical calculations, and displayed for a parallel configuration for two different phases in Fig. 4.3a. The return kinetic energy of the electrons is shown on the vertical axis in Fig. 4.3b-f normalized to the ponderomotive energy of a free electron in the laser field. The horizontal axis shows one full cycle of the fundamental laser field. The time-frequency plots in Fig. 4.3 were obtained by calculation of the transverse components of the single-atom time-dependent dipole using the strong-field approximation (SFA) integral with a hydrogenic transition matrix element [144]. Subsequently, for each time in the optical cycle a frequency analysis was

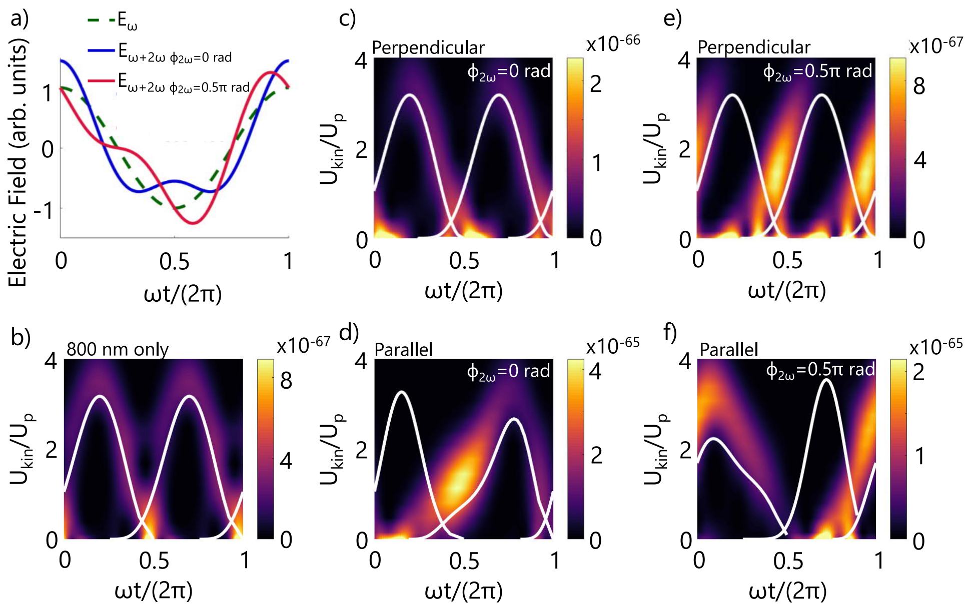

Figure 4.3: Time and frequency resolved emission. The color scale represents the squared dipole moment in C^2m^2. The white lines are the semi-classical calculation of the frequency versus the recombination time. (a) Electric field for one and two colors, for two different two color phases. (b) For 800 nm only. Long and short trajectories are labeled in the first half-cycle emission (not labeled but clearly visible in the second half cycle). (c) Two-color phase of 0 rad, perpendicular configuration. (d) Two-color phase of 0.5 π rad, perpendicular configuration. (e) Two-color phase of 0 rad, parallel configuration. (f) Two-color phase of 0.5 π rad, parallel configuration.

performed by multiplying the time-dependent dipole using a Gaussian window function with a r.m.s width of 0.4 ω centered around the time under investigation, Fourier transforming, and subtracting the ionization potential. The color map in Fig. 4.3 represents the square of the dipole moment, which is proportional to the single-atom emission intensity and therefore also to the yield of the harmonics, if phase matching can be neglected. The white lines are the return kinetic energies, as calculated semi-classically according to the three-step model [15, 143]. In these calculations, a total intensity of 10^{14} W/cm^2 with a relative contribution of 20 % second harmonic light was assumed. We assumed Gaussian laser beams focused to a 1/e^2 waist radius of 35 µm, with pulse energies of 0.72 and 0.18 mJ for the fundamental and SH respectively, and a pulse length of 80 fs FWHM for both. A flattop gas target was assumed with a length of 220 µm and a pressure of 100 mbar Argon, placed 4 mm upstream of the focus.

In the case of a one-color driving field (Fig. 4.3b) the mapping of each harmonic energy onto the recombination times in each half cycle is clearly visible. The short trajectories are positively chirped (positive slope of the emission in the time-frequency plots) and the long trajectories are negatively chirped (negative slope). We note that the SFA calculation agrees well with the semi-classical calculations. The emission intensity of the short and long trajectories is comparable, which is in agreement with the general observation of a double-Gaussian beam profile of the high-order harmonics. With the addition of a perpendicular SH field, the relative ratio between the long and short trajectories is heavily modified by the relative phase of the two-color field, see Fig. 4.3c and e for the two-color phases of 0 and 0.5π rad, respectively. Again, the SH field imparts a lateral component to the momentum of the continuum electrons, thus preventing the recombination of either short (Fig. 4.3c, 0 rad) or long electron trajectories (Fig. 4.3e, 0.5π rad), depending on the relative two-color delay. In particular, the short trajectory selection for a relative phase of 0.5π is strongly enhanced, resulting in an overall increase of the total yield for this relative two-color phase. In the case of parallel two-color generation, the forces on the continuum electrons exerted by the two fields are aligned parallel and therefore trajectory selection by hindering recombination of electrons is not possible. Nevertheless, there is a clear difference in yield from the short and long trajectories as shown in Fig. 4.3d,f. This is because the two-color phase will act as a gate for certain ionization times in the parallel case, leading to half-cycle emission with very different cutoff energies. For a relative two-color phase of 0 rad, the increased total electric field leads to enhanced ionization close to an absolute phase of the combined field of $\omega t = 0$ (x-axis in Fig. 4.3a). Ionization of electrons in this window will lead to emission of lower-energy photons, i.e. to a lower half-cycle cutoff than in the one-color case, because the absolute total electric field at the instant of recombination is lowered for subsequent absolute phases ωt of the combined fields. The strong difference in half-cycle cutoffs becomes even more extreme for a relative two-color phase of 0.5π rad (Fig. 4.3f), and the same argumentation holds. The two half cycles lead to strongly different emission cutoffs, with the lower one contributing the highest yield.

Overall the simulations suggest stronger trajectory suppression and hence larger control over the divergence for perpendicular polarizations on the one hand, but estimate on the other hand a higher emission intensity for the parallel configuration, compared to the monochromatic and the perpendicular two-color configuration. We thus set out to test this theoretical indication both through simulations and experiments, in order to find optimum polarization and two-color phase configurations that allow for simultaneous divergence and yield optimization. In addition, the predicted difference in half-cycle cutoffs can be exploited for an absolute phase and intensity calibration of the two-color field.

4.3. Experimental details

To control the relative phase and the relative polarization between a fundamental field and its second harmonic (SH) we use the setup as shown in Fig. 4.4. The fundamental 800-nm pulses are frequency doubled to 400 nm, using a 0.2 mm thin β-BBO (Castec). The power of the SH pulses was kept constant at 200 mW. The total power of the two-color pulses was 1.6 W. Assuming similar pulse lengths, similar focal spot sizes and perfect temporal synchronization, this leads to a SH intensity fraction of about 14%. The delay between the fundamental and SH is compensated using two calcite plates. By motorizing the rotation angle of one of the calcite plates, sub-cycle control over the delay between the two colors was possible. To control the relative polarization, a half-wave

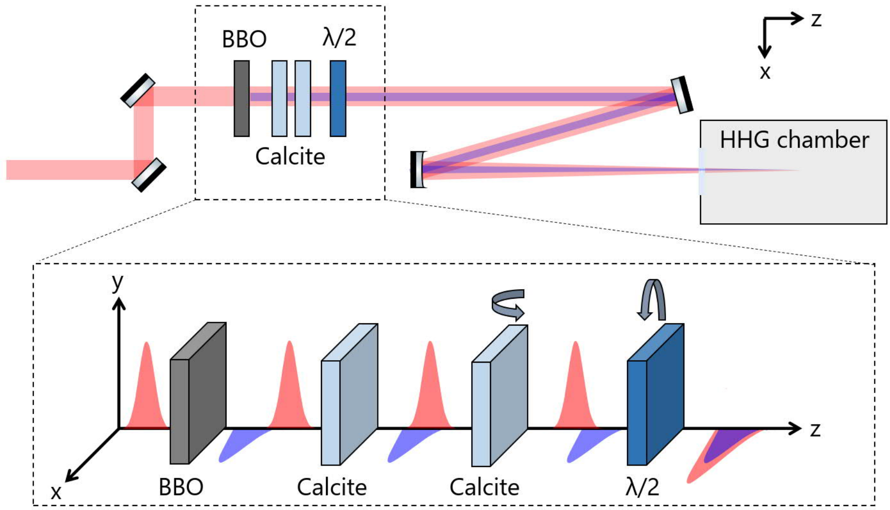

Figure 4.4: Experimental setup to control the relative phase and polarization between a fundamental and the second harmonic.

plate (Eksma Optics) for the 800 nm pulses was used, which acts roughly as a zero-wave plate for the 400 nm pulses. The two-color pulses are then focused inside an effusive Argon gas jet, using a 75 cm focal length aluminum spherical mirror. The gas jet was positioned using a 3D translational stage just before the focus. This configuration minimizes phase mismatch and reabsorption, leading to the observation of a near-single-atom response. In order to compare two-color HHG with HHG driven by monochromatic 800 nm pulses, the BBO was taken out, and the intensity of the monochromatic and two-color pulses was matched, to obtain similar cutoffs and therefore a fair comparison between the two generation schemes.

The harmonics are spectrally dispersed with a concave abberation-corrected flat-field grating, and are detected using a double-stack microchannel plate backed with a phosphor screen. The harmonics freely propagate in the vertical direction, while being focused in the horizontal direction by the grating. The phosphor screen is imaged using a CMOS camera.

4.4. Results

4.4.1. Absolute calibration of two-color fields

We now turn to exploiting the strong cutoff modulations as a function of the relative two-color phase in parallel polarized two-color fields for calibrating the absolute two-color phase and absolute intensities of fundamental and SH. The simulations in Fig. 4.3d,f suggest that adjacent half cycles will gain different cutoff energies, which we now test

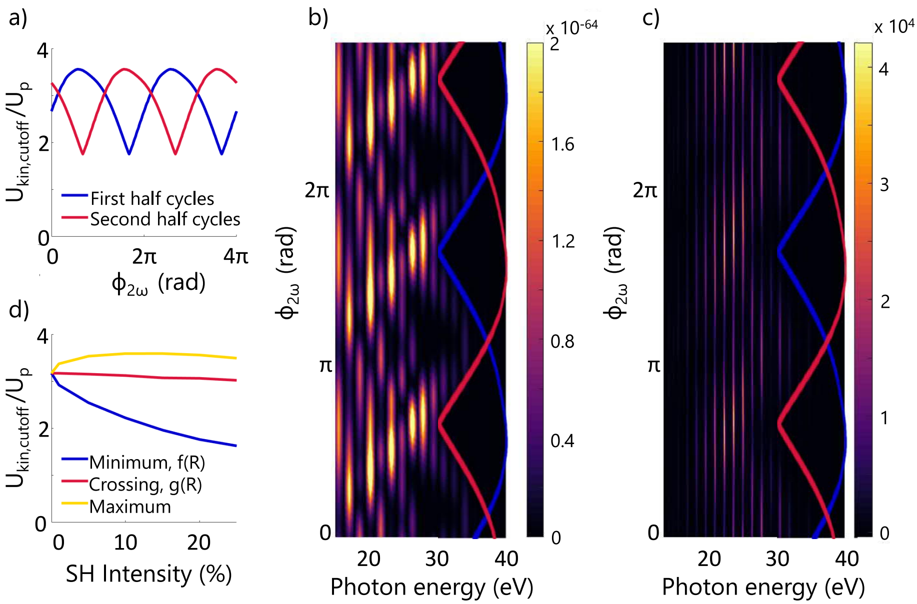

Figure 4.5: Cutoff modulation in parallel polarized two-color HHG. (a) Cutoff kinetic energy in adjacent half cycles, called first and second half cycle, as a function of two-color phase. Depending on the relative phase, each half cycle will have a different cutoff. (b) Simulated two-color HHG spectra as a function of two-color delay, showing how the cutoff modulates depending on the two-color phase delay. (c) Experimental HHG spectra as function of two-color phase, showing the same cutoff modulation as suggested in the simulations in (b). (d) Change of cutoff energy as a function of SH intensity. See text for details on the plotted functions.

experimentally in Fig. 4.5.

The kinetic energy of the returning electron in the cutoff for two adjacent half cycles, as obtained by semi-classical calculations, is shown in Fig. 4.5a. For delays where the two half cycles have the same cutoff, the maximum kinetic energy is close to the cutoff energy in one-color HHG (3.17 U_p). The simulated and measured HHG spectra as a function of two-color phase, as shown in Fig. 4.5b,c, respectively, show an excellent match and reveal that the cutoff modulation has a large impact on the yield of the generated harmonic spectra. If we overlay the modulation of the cutoff of adjacent half cycles from Fig. 4.5a with simulated and measured spectra (red and blue lines in Fig. 4.5b,c), we observe that the lower branch generates the most intense harmonics, in agreement with SFA calculations shown in Fig. 4.3d,f. Comparing the cutoff and intensity modulation between experiment and simulation now allows calibrating the absolute two-color phase, which was used throughout this chapter. In addition, we can calibrate the absolute intensities of the two-color field, as the cutoff-energy change as a function of two-color phase depends on the relative intensity of the fundamental and SH. For that purpose, the minimum and maximum cutoff energies $\hbar\omega_1$ and $\hbar\omega_2$ are extracted from the experimental data in Fig. 4.5c. We call the kinetic energy of the minimum cutoff from the experimental data normalized to the ponderomotive energy $f(R) = (\hbar\omega_1 - I_p)/U_p$ (blue line in Fig. 4.5d), with I_p the ionization potential and U_p the ponderomotive energy. The kinetic energy of the maximum cutoff from the experimental data is $g(R) = (\hbar\omega_2 - I_p)/U_p$ (red line in Fig. 4.5d). While the minimum cutoff in the experimental data corresponds to the simulated minimum half-cycle cutoff (minimum of blue and red lines in Figs. 4.5a,b,c), the maximum cutoff $g(R)$ that is visible in the experimental data corresponds to the crossing of maximum and minimum cutoff of the simulated data (crossing of red and blue line in Figs. 4.5a,b,c). The maximum cutoff as obtained by the semi-classical calculation (maximum of blue and red lines in Figs. 4.5a,b,c) is barely visible, neither in the SFA simulation (Fig. 4.5b) nor in the experimental data (Fig. 4.5c). By comparing the measured kinetic energy corresponding to the crossing point (red line in Fig. 4.5d) and the minimum cutoff (blue line in Fig. 4.5d) to the predicted values as a function of relative SH intensity, we can determine the SH intensity fraction, and from the cutoff crossing point (which does not vary much with SH intensity fraction) the absolute intensity can be determined. With this procedure we obtain a total peak intensity of $1.4 \cdot 10^{14}$ W/cm^2, a peak intensity of $1.2 \cdot 10^{14}$ W/cm^2 for the fundamental, and a peak intensity of $0.2 \cdot 10^{14}$ W/cm^2 for the SH.

While determining the peak intensity is in principle possible by measuring pulse duration, focus size and pulse energy separately, we find that the procedure outlined here gives far more accurate results, as it also reveals if fundamental and SH are properly temporally synchronized and spatially overlapped in focus. The method proposed here furthermore directly relates to the intensities that are involved in HHG as opposed to deducing intensities from a number of separate measurements.

4.4.2. Far-field characteristics

We now analyze the yield and divergence optimization in two-color HHG in detail, and determine which relative polarization between SH and fundamental in the two-color field most favorably influences these beam properties. To this end, we have measured the divergence-resolved far-field harmonic spectra for three different relative polarizations between the two colors, and scanned the relative two-color phases, see Fig. 4.6.

For a perpendicular configuration (Figs. 4.6a and b), both the shape and the yield of the spectrum change significantly for different two-color phases. Figures 4.6a and b represent phase delays that generate a rather mono-Gaussian profile (Fig. 4.6a) and a more divergent profile (Fig. 4.6b), respectively. Whereas the generation in Fig. 4.6a is very centered, and most signal is contained in the smaller divergence angles, Fig. 4.6b shows a much larger distribution of signal across larger divergence angles. This demonstrates that the divergence of the beam can be controlled by changing the relative two-color phase delay. This is directly related to the selection of short or long trajectories as shown in our simulations in Figs. 4.3b,d. In addition, we also observe that the yield for the more mono-Gaussian profile is higher than for the more divergent spectrum.

The second row of spectra corresponds to measurements with a relative polarization of 45 degrees. In Figs. 4.6c and d, we show spectra for 0.5π rad and 0 rad phase delay, that generate a high and a low total yield, respectively. There is a slight difference in divergence visible between the two spectra, but this is not as significant as for the perpendicular case in Figs. 4.6a,b. We notice that the cutoff changes by a few harmonic orders for the two different two-color phases in Figs. 4.6c and d. This is a direct result of the different half-cycle cutoffs of adjacent half cycles in (partially) parallel polarized two-color fields as shown in Fig. 4.5c, which lead to a strong cutoff modulation as a function of the two-color delay. In the third row, we analyze the results of two-color delay scans for parallel polarized two-color fields. Figure 4.6e shows the spectrum for a two-color phase of 0.5π rad, producing a high yield, and Figure 4.6f shows the spectrum for 0 rad, producing a low yield. Similar to the figures in the center column for 45 degree polarization in the two-color field and in agreement with the SFA simulations in Fig. 4.3, we see an enhanced cutoff extension in Figure 4.6f, where the yield is lowest.

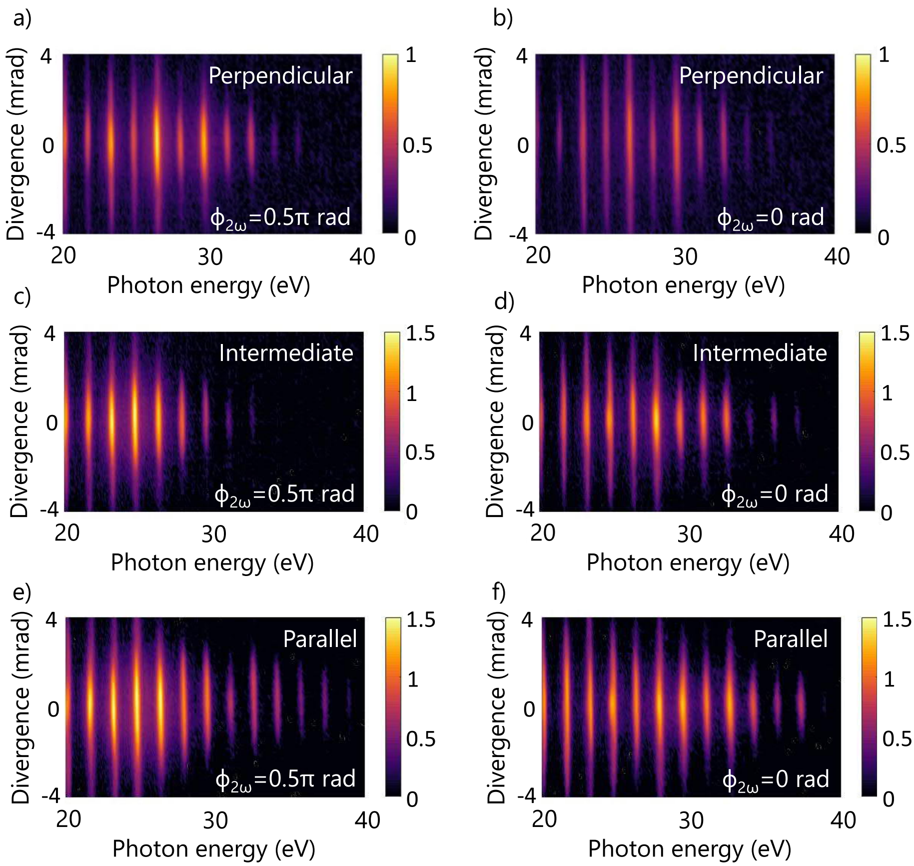

Figure 4.6: HHG spectra for different two-color phases and relative polarizations: (a,b) HHG spectra for perpendicular polarizations between SH and fundamental, for 0.5π and 0 rad, respectively. (c,d) HHG spectra for relative polarizations of 45 degrees, for 0.5π and 0 rad, respectively. (e,f) HHG spectra for parallel polarizations, for 0.5π and 0 rad, respectively. The color maps denote yield on a logarithmic scale.

We now turn to the analysis of a complete scan of the relative phase delay of the two-color field, displayed in a single figure, see Fig.4.7a. Figure 4.7 is a compact way of plotting an entire scan of a divergence- and energy-resolved HHG spectrum as a function of the two-color phase: the sinusoidal modulations of the HHG signal as a function of the two-color phase (oscillations of a few different energies and divergences are shown in Figs. 4.7b-d) are Fourier transformed pixel by pixel. The frequency component with the highest amplitude from this Fourier transform corresponds to an oscillation-cycle duration of 0.67 fs (equivalent to a relative phase shift by π rad). The amplitude of this frequency is displayed in Fig. 4.7a as the brightness of the plot, bright (as opposed to dark) regions indicate an intense harmonic signal. The phase of this frequency is encoded as color, and is determined by the phase of the intensity oscillations in each different pixel (as shown in Fig. 4.7b-d) and can thus be directly linked to relative two-color delays in units of the phase of the two-color field in radians, as shown in the legend (round color map) in Fig. 4.7a. Two pixels with colors on opposite ends of this legend thus correspond to intensity modulations, where the intensity in one pixel is maximized, whereas the other one is minimized for the same two-color delay. Figure 4.7a thus displays at which two-color delay each pixel in the spectrum has the highest emission intensity.

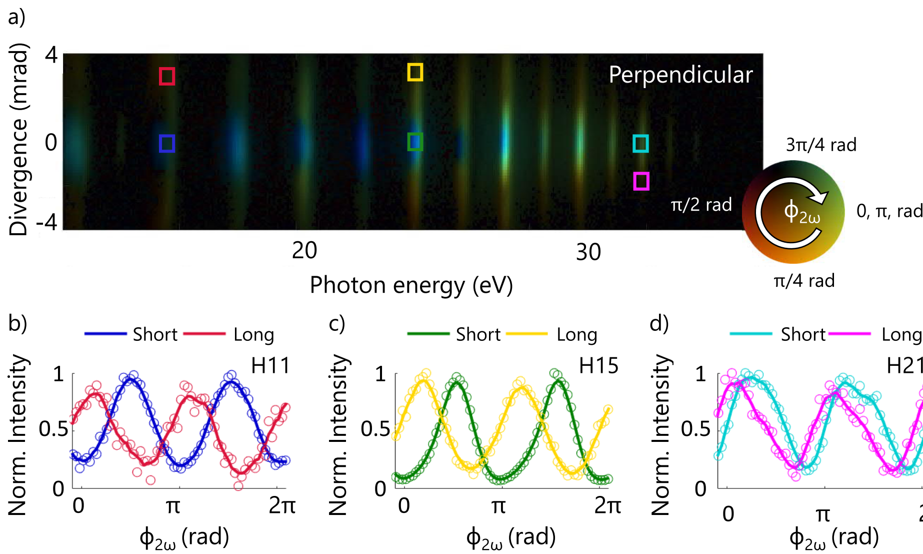

Figure 4.7: (a) Pixel-by-pixel Fourier transform of the HHG intensity as a function of two-color delay. The brightness encodes the amplitude of the dominant frequency component of the Fourier transform, and the color encodes its phase. The legend (round color map in the bottom right) indicates how the color is related to the phase of the two-color field. The intensity oscillations as function of two-color phase for selected regions of interest marked in (a) are shown for (b) harmonic order 11, (c) harmonic order 15, and (d) harmonic order 21 as function of the two-color phase.

As long and short trajectories show a maximum emission intensity for different two-color phases, this method directly visualizes which parts of the divergence-resolved beam profile are dominated by long and short trajectories, respectively. There is a clear discrimination between the larger (green-yellow) and smaller (blue) divergence angles for each harmonic order. This means that at the two-color delay related to the blue color, the harmonic signal that is coming from the smaller divergence angles is optimized, which we can relate to the emission of short trajectories. Oppositely, for the two-color delay related to the green-yellow shade, the signal is maximized in the wings, caused by an increase of long trajectory emission. In addition, each harmonic order shows a slightly different color shade, denoting that each order has a different two-color phase at which either the short or the long trajectories optimize, reflecting the change in recombination times for different harmonics. Comparing the oscillations for different harmonic orders in the spectrum, see Fig. 4.7b-d, we note that the phase difference between the two trajectories becomes smaller for higher harmonics. For the harmonic orders in the cutoff, long and short trajectories merge and thus there is no discrimination for emission between larger and smaller divergence angles, as can be seen also in Fig. 4.7 from the absence of a phase (color) contrast for small and large divergences in cutoff harmonic orders.

In the same way we will analyze the complete two-color phase scan of the intermediate polarization of 45 degrees, see Fig. 4.8a. Again we observe a color difference between inner and outer divergences for each harmonic order, which is particularly pronounced for the plateau harmonics. In addition, we observe that the modulation of the cutoff is especially visible, as we see a clear color contrast for plateau and cutoff harmonics, which means their yield maximizes for different two-color phases. This is a direct result of the different half-cycle cutoffs of adjacent half cycles in (partially) parallel polarized two-color fields as shown in Fig. 4.5c, which lead to a strong cutoff modulation as a function of the two-color delay. Overall this demonstrates that a relative polarization angle of 45 degrees provides an intermediate case, where the perpendicular SH component can still give a large enough lateral momentum to the electrons for trajectory selection, whereas the enhanced ionization through the parallel component of the SH field favorable enhances the yield. In addition, it has been reported [161–163] that an intermediate polarization between two-color fields will lead to elliptically polarized harmonics. The manipulation of the electron trajectories by using two-color fields can lead to a classical angular momentum of the electrons with respect to the atom, due to a point of recombination of the electron which is at a distance from the nucleus. The additional asymmetry of adjacent half-cycles leads to an elliptical polarization.

For the parallel case we take a look at Fig. 4.8b. The analysis of the complete two-color scan shows again that the cutoff harmonics optimize for a different two-color phase than the plateau harmonics, similar to the observation and explanation of Fig. 4.8a and in agreement with the SFA simulations in Fig. 4.3. We also observe that the divergence-resolved profile of each harmonic order in Fig. 4.8b still shows a substructure of two-color phases (colors) at which the yield optimizes. For example the harmonic around 22 eV shows orange wings in the vertical direction, and a green center. In contrast to the other polarization angles, this trend is not as clear and uniform among all harmonics simultaneously. This is because for parallel polarizations, the two-color delay also acts as a gating mechanism in the ionization step, such that the yield of each harmonic will

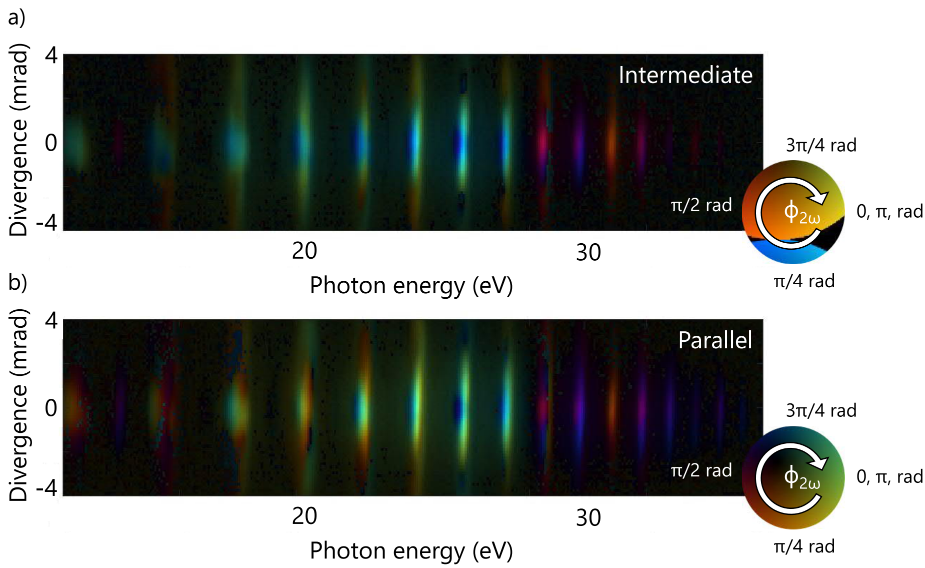

Figure 4.8: (a) Fourier map for 45 degree polarization. (b) Fourier map for parallel polarizations.

be optimized at a different two-color delay, corresponding to different colors for each harmonic in Fig. 4.8b. In addition, since the short and long trajectories have different ionization times, color contrast within a harmonic is still visible. This is in agreement with Fig. 4.3, in which we observed that also in the parallel two-color configuration there is a selection of long and short trajectories due to the changing ionization gate as function of two-color delay, albeit less pronounced than for perpendicular polarizations.

4.4.3. Divergence and yield optimization

In this section we analyze the beam profiles in two-color HHG in more detail, to quantify the divergence change and the signal level of the harmonic orders for different relative two-color delays, see Fig. 4.9. We start with the analysis of harmonic orders, generated in a perpendicular two-color configuration. For these experiments, we removed the half-wave plate in order to rotate the polarization of the 800 nm pulses, and obtain directly a perpendicular configuration between the 800 nm and 400 nm pulses. The relative strength of the SH intensity was approximately 25%. The divergence of the harmonics is determined by summing the intensity of harmonic 13 through harmonic 23 and normalizing it to their maxima, to highlight the effect of the two-color fields on the divergence. The spectrum is generated with the gas jet before the focus, such that the divergence of the short-trajectory contributions is intrinsically small [148]. This small divergence is achieved because the dipole phase and phase-front curvature of the fundamental possess opposite signs and thus partially cancel each other out when the gas-jet is placed before the focus. This gas-jet position is therefore the natural choice for divergence optimization in two-color HHG, as the short trajectory component of the beam already possesses the desired property. At the same time, the more divergence long-trajectory contributions are efficiently phase matched with the gas before the focus [165, 166]. However, we show that this does not present a problem, since the long-trajectory contribution can be effectively suppressed in two-color HHG [83]. The profile of the beam generated with the 800-nm fundamental only (dashed red curve) in Fig. 4.9a is still clearly not mono-Gaussian, indicating the presence of both long and short trajectories. The blue curve displays the HHG beam profile for a relative two-color phase of 0.5π rad, at which the short trajectories are enhanced. The green curve represents the beam profile for a relative phase of 0 rad, optimizing the contribution of the long trajectories.

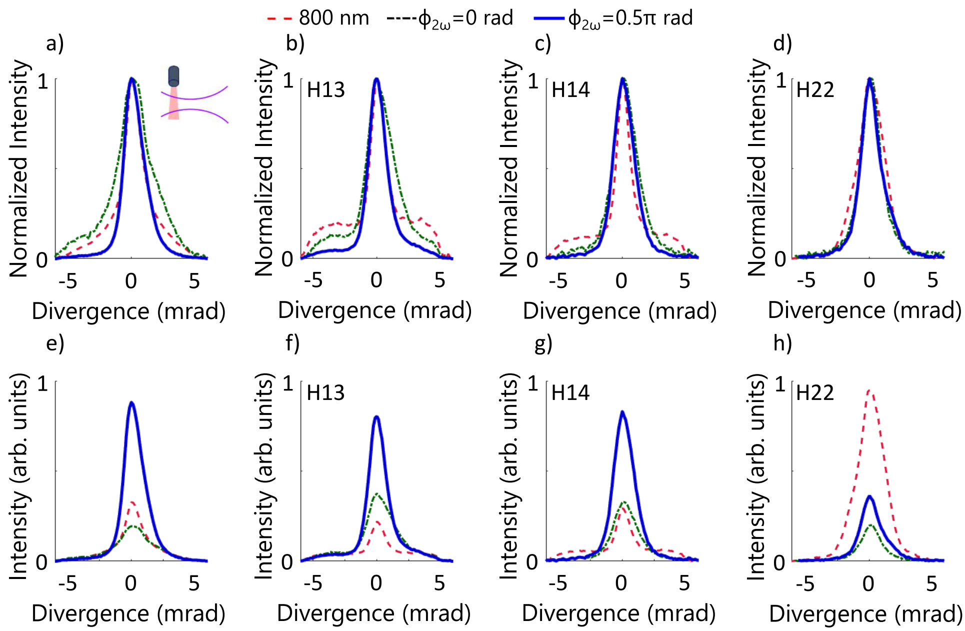

Figure 4.9: Experimental beam profiles: a) Perpendicular two-color HHG, divergence comparison for a relative phase of 0 rad (green) and 0.5π rad (blue) phase and 800 nm only (red) for H13-H23. Divergence comparison for b) H13, c) H14, d) H21. e) Yield comparison for H13-H25, with separate comparison for f) H13, g) H14, h) H21.

The beam profile generated with two-color driving and a relative phase of 0.5π rad has much less signal in the wings at larger divergence angles in Fig. 4.9a compared to HHG with the fundamental 800-nm field only. Simultaneously, the total signal at this relative phase is enhanced by a factor of 2.2 compared to the HHG with the fundamental field, as can be seen in Fig. 4.9e, which shows the actual and not the normalized intensity. Each beam profile can be fitted by a double Gaussian, as previously illustrated in Fig. 4.1b, which allows estimation of the relative contributions from the long and short trajectories. In the case of two-color HHG optimized for short trajectories (blue), the amplitude of the long-trajectory contribution is decreased by a factor of 1.9 compared to the conventional one-color HHG (red). This demonstrates that for a relative phase of

0.5π rad, both the divergence and the total signal level are improved. At this phase, the instantaneous ionization rate is modified in favor of the short trajectories and the long trajectories are prevented from recombining. At a relative delay of 0 rad, displayed by the green curve, the signal in the wings is enhanced. In addition, the total signal level is comparable to the signal for the HHG with the fundamental 800-nm field only.

The change of the instantaneous ionization rate as a function of the two-color phase is, in general, small for the long trajectories and, in particular, less significant than for the short trajectories. Therefore, a relative delay of 0 rad does not enhance the signal level of the long trajectories very much. Simultaneously, this phase deflects electrons related to short trajectories, thus decreasing the overall signal from the short trajectories. Figures 4.9b-d,f-h, show the divergence and yield changes for three separate harmonics orders 13 (62 nm), 14 (57 nm), and 23 (35 nm), respectively, taken from the same scan as the total profile shown in Fig. 4.9a. In order to compare the even harmonics with the 800-nm only configuration, an average of the neighboring odd harmonics signal is taken for generating the red curve in Figs. 4.9c,g. For lower harmonics, the long and short trajectories have vastly different excursion amplitudes. Therefore, the low harmonics show a large difference in total intensity and divergence for the two different relative phases. In all cases, the short-trajectory-optimized (800 + 400)-nm-driven HHG emissions (blue curves) show less signal in the wings, compared to the 800-nm-driven HHG (red curves). Also, the overall intensity in Figs. 4.9e-g, of the blue curve compared to the red curve increases by factors of 10 and 2 for harmonic 13 and 14 but decreases for harmonic 23 by about a factor of 2. We note that harmonic 23 is close to the cutoff and the intensity of the two-color field is likely slightly lower than for 800 nm only, as observed by a reduced cutoff. However, harmonics near the cutoff show less increase in absolute signal or even a decrease in general. The reason is that the relative excursions for the long and short trajectories become similar for higher harmonics and merge in the cutoff of the spectrum.

To further investigate the process of improving the brightness of the HHG beam, the position of the gas jet and the ratio between the power of the fundamental and second-harmonic field are varied. Figures 4.10a,b show the beam profiles in which the gas jet is positioned behind the focus. In this configuration, phase matching favors the short-trajectory contribution [165, 166] but the divergence is increased [148] and the yield decreased compared to the situation in which the jet is before the focus. As a consequence of the intrinsically increased divergence, the signal in the wings is suppressed even more in short-trajectory-optimized two-color HHG (blue) compared to the fundamental-field case (red), namely by a factor of 2.2 as compared to a factor of 1.9 in Fig. 4.9a. The overall intensity of the signal is increased (Fig. 4.10b) by a factor of 2.9, also surpassing the factor of 2.2 obtained in Fig. 4.9a, where the gas jet is placed before the focus. Figures 4.10c,d show the beam profiles for an experiment in which the percentage of the second-harmonic power is lowered to 11%. Although the total intensity is slightly improved at a relative delay of 0.5π rad compared to 800 nm only, the improvement of the divergence is less pronounced with the lower second-harmonic field power. By having a lower contribution of the second harmonic, the ionization rate will be changed less compared to the fundamental-field-only case. Also, the selection of trajectories by introducing a smaller lateral velocity component will become less efficient.

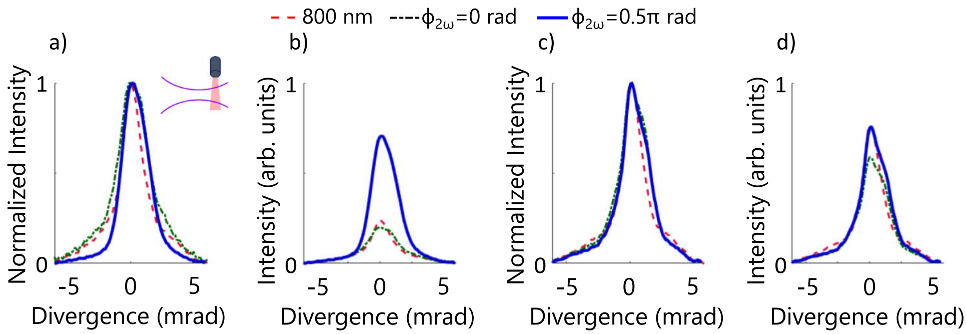

Figure 4.10: Experimental beam profiles: a) perpendicular two-color HHG, gas jet behind the focus, divergence comparison with 800 nm only (red) and for 0 (green) and 0.5π rad (blue) phase delay. b) Yield comparison. c) Perpendicular two-color HHG with only 11% of SH, divergence comparison. d) Yield comparison.

Next, we analyze the beam profiles in two-color HHG for different polarization angles and systematically compare experimental and simulated results. These experiments are performed under the conditions described in the experimental details section of this chapter, with the half-wave plate implemented to rotate the relative polarization between the 800-nm and 400-nm pulses. The top row of Fig. 4.11 shows simulated, spectrally-integrated profiles. These beam profiles were obtained by using the single-atom time-dependent dipole data, as shown in Fig. 4.3, as input to a propagation code based on the slowly varying envelope and paraxial approximations [164], which coherently adds the emitted contributions of each volume element of an extended gas medium while taking diffraction and dispersion effects into account. The time- and position dependent amplitude and phase of both laser fields were calculated by propagation through the gas medium, while keeping track of ionization-induced refractive index changes. The resulting XUV beam profile in the far-field was obtained by a Hankel transform.

For the two extreme cases, namely parallel and perpendicular polarizations, we compare the total yield (Figs. 4.11a,c) and the shape of the beam profiles after normalization (Figs. 4.11b,d). This is done for two phases, 0 and 0.5π rad (green dash-dotted and solid blue lines, respectively), which correspond to phases that optimize long and short trajectories for the perpendicular configuration, respectively. The yield and beam profile of the monochromatic configuration is also shown as a dashed red line, for comparison. The parallel two-color scheme leads to a much higher yield compared to the one-color case, for both phase delays, as shown in Fig. 4.11a. Especially for a phase delay of 0.5π rad, the yield is greatly enhanced. For the same phase delay, the shape of the beam profile is also slightly less divergent compared to the one-color configuration as shown in the normalized profiles in Fig. 4.11b. In the perpendicular configuration, a phase delay of 0.5π rad leads to the highest yield (Fig. 4.11c), which is also enhanced compared to the one-color case. Additionally, a two-color phase of 0.5π leads to an overall narrower beam shape (Fig. 4.11d).

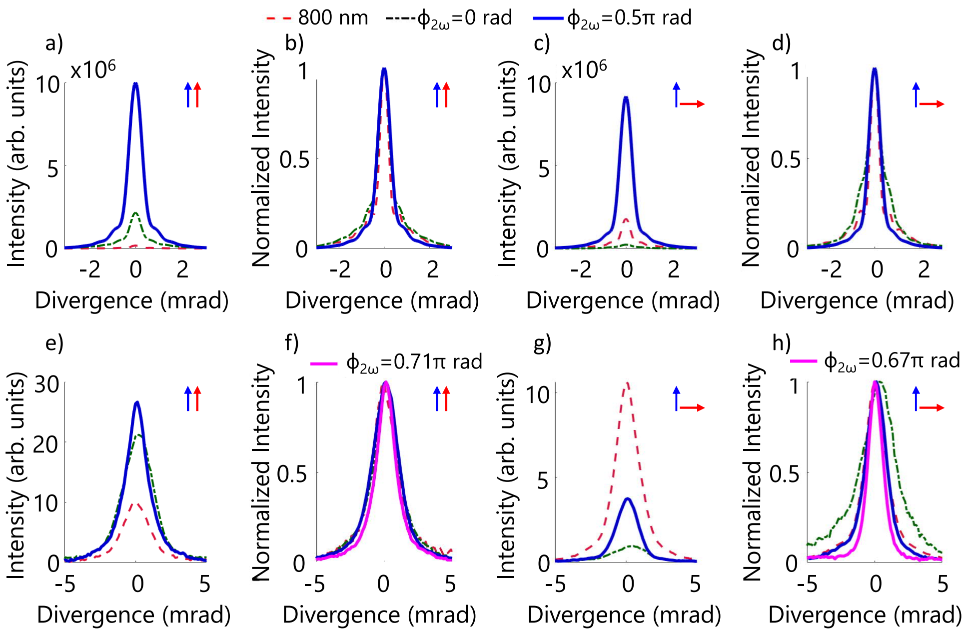

Figure 4.11: Simulated and experimental beam profiles: (a) Simulated parallel two-color HHG, yield comparison for 0 (green) and 0.5π rad (blue) phase delay and 800 nm only (red). (b) Simulated parallel two-color HHG, divergence comparison. (c) Simulated perpendicular two-color HHG, yield comparison. (d) Simulated perpendicular two-color HHG, divergence comparison. (e-h) Experimental beam profiles, corresponding to (a-d).

The simulations are compared with the experimental results in the bottom row of Fig. 4.11, for the same two-color phases of 0 and 0.5π rad, and for the same spectral region (H13-H25). The total yield for the parallel configuration, shown in Fig. 4.11e, is in excellent agreement with the simulated data (panel a). Both delays lead to a considerably higher yield than in the monochromatic case, and the beam profiles show some phase-dependent modulation as well: there exists a phase (0.71π rad) that minimizes the overall divergence of the harmonic beam, as shown in Fig. 4.11f, which is explained by trajectory selection through gating the ionization times in the earlier sections of this article. In the perpendicular case, the two-color phase has a large influence on the yield of the emission. The monochromatic case leads to a higher yield (Fig. 4.11g) than both two-color phases, in contrast with our simulations (Fig. 4.11c) and our previous set of experiments shown in Fig. 4.9, where we showed that perpendicular polarized two-color HHG can improve the yield as well. We attribute this discrepancy to the necessary introduction of a half-wave plate for 800 nm into the common beam path of 800 nm and 400 nm for adjusting the relative polarization between both colors in the present experiments discussed. This waveplate was identified to introduce some ellipticity to the 400 nm beam, lowering the total yield that could be achieved with a cleaner overall polarization state in the absence of a waveplate. In addition, the ratio between the fundamental and SH intensity will influence the amount of yield enhancement, as demonstrated in Fig. 4.10d.

In agreement with the results in Fig. 4.9, we observe that the perpendicular two-color configuration has dramatic effects on the divergence (Fig. 4.11h). The beam profiles for a phase of 0 rad and 0.5π rad show a similar trend as the simulation. For the phase of 0.5π rad the beam profile becomes more narrow than the monochromatic case. Conversely, there is a two-color phase (0 rad) that makes the contribution of the long trajectories dominant at large propagation angles, thus increasing the divergence. In addition, we show a two-color phase that minimizes the long trajectories (0.67π rad), where their contribution vanishes almost entirely, so that the overall beam profile approaches a perfect mono-Gaussian distribution.

The results in Fig. 4.11 have shown the strong influence of two-color HHG on the yield and beam profile / divergence. We now analyze further which two-color delays optimize divergence and yield, respectively, to see if both quantities can be optimized simultaneously. In Fig. 4.12, we track the total yield (black line) of the harmonics for each phase delay, which we obtain by summing the total signal of the detected harmonics. The total yield is normalized to the total 800 nm yield, to eliminate detection efficiencies depending on polarization. Second, we determine at which divergence angle the intensity of the beam profile reaches a $1/e^2$ value, which we show by the red line. We compare these values with the values obtained from HHG with the fundamental only, which are shown by the dashed lines. We compare the divergence of the two-color data for all polarization configurations to the perpendicular value.

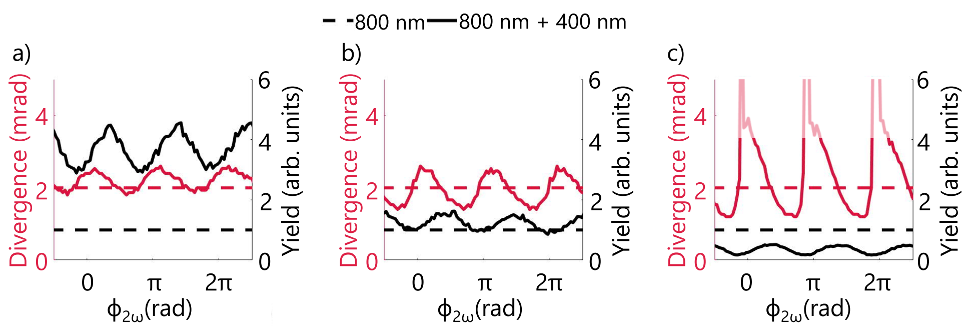

Figure 4.12: Divergence and yield, for different relative polarizations between SH and fundamental, as a function of two-color phase. (a) Parallel polarizations, leading to similar divergence as 800 nm generation, and much higher yield compared to 800 nm generation. (b) Two-color configuration, with 45 degree relative polarizations, showing improved divergence, and improved yield compared to 800 nm only. (c) Perpendicular two-color configuration, showing improved divergence compared to 800 nm only. The faded out areas correspond to profiles that became so broadened that a reliable extraction of the divergence angle at an intensity of $1/e^2$ became unfeasible.

The first remarkable observation is that for any two-color delay in the parallel configuration, the yield of the harmonics is higher than for the one-color configuration, see Fig. 4.12a. Second, tracking the divergence observable, we can see that there is a dependence on the two-color delay. The beam profile becomes narrower than in the one-color case for most of two-color delays. Interestingly, the yield and divergence do not optimize at the same two-color delays. This is expected, as the yield will optimize for maximizing both short and long trajectories, whereas the divergence changes when either selecting the short or the long trajectory. For an intermediate polarization, the yield in the two-color case is again still higher for any two-color phase than for the one-color configuration, illustrated in Fig. 4.12b. Also, we see an improved divergence, depending on the two-color delay. For a perpendicular two-color configuration, we can see that the divergence curve shows an even larger contrast than for the other polarizations, as shown in Fig. 4.12c. This confirms the significant control over trajectories in this configuration. The overall yield is lower than for the one-color configuration, which we discussed before in the text around Fig. 4.11. All in all, the results in Fig. 4.12 show that for an appropriately chosen two-color phase, two-color HHG can increase the yield and decrease the divergence and thus improve both quantities. However, the phase at which divergence and yield optimize is not identical. The relative polarization between SH and fundamental allows an experimentalist to choose between perfecting either the divergence (perpendicular polarizations) or the yield (parallel polarizations).

We have summarized our results, for five relative polarization angles in Fig. 4.13. The overall yield is the highest in the parallel case. For 67.5 degrees and larger angles, the yield becomes lower than in the one-color configuration. Even for these angles we do expect that perpendicular two-color HHG can still be made more efficient than one-color HHG as shown in Fig. 4.9, and the discrepancy was explained in the previous section by the necessary introduction of a waveplate and the ratio between the fundamental and SH intensity. Divergence control is the clearest in the perpendicular two-color configuration, as the contrast between the narrowest and broadest divergence at $1/e^2$ is the largest at this polarization angle. Still, for all polarization angles, divergence control is visible.

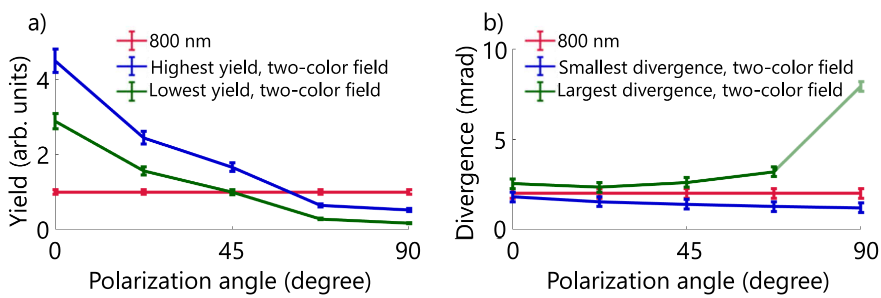

Figure 4.13: Summary of divergence and yield in two-color HHG. (a) Highest (blue) total yield for two-color HHG, compared to the lowest (green) total yield, and the 800 nm only configuration (red), for five different polarizations. (b) The blue line shows results for two-color phases, which minimize the divergence, as a function of the polarization angle between both colors in the two-color field. This is compared to results obtained with a two-color phase where the divergence is broadest (green), and to the divergence of HHG with the fundamental only (red). The last data point for largest divergence (green) at 90 degrees polarization angle is faded out, as it corresponds to a very divergent beam profile where an accurate divergence extraction becomes difficult, similar to the results in Fig. 4.12c.

We want to stress the importance of the divergence and yield control for intermediate polarization configurations with respect to the polarization state of the generated high-harmonics. The divergence control demonstrates that the electron trajectories are modified depending on the two-color phase. As mentioned before, and shown in [161–163], the lateral component in cross-polarized two-color HHG will lead to a classical angular momentum of the electrons relative to the atom. If both half-cycles are symmetric, which is the case for perpendicular cross-polarized two-color fields, the angular momentum obtained in each half-cycle will cancel out with the adjacent symmetric cycle and the harmonics will be linearly polarized. For intermediate cross-polarized configurations, adjacent half-cycles are not symmetric, as described around Fig. 4.8a,b, such that there is an effective angular momentum for the electrons which will be translated into elliptically polarized harmonics. Although we have not measured the ellipticity explicitly, the agreement between the SFA simulations and experimental data throughout this chapter gives confidence that the harmonics are indeed elliptically polarized. The generation of elliptically and circularly polarized extreme-ultraviolet pulses with two-color fields provides opportunities for circular dichroism in the extreme-ultraviolet range [167].

4.5. Conclusion and outlook

In conclusion, we have conducted an extensive parameter study to identify the effects of the relative polarization between the two colors in two-color high-harmonic generation. We have compared the divergence and the yield with the one-color configuration. A parallel polarization of fundamental and SH in the two-color field leads to the highest yield enhancement. A perpendicular configuration leads to the best divergence control. The simulations quantitatively reproduce the experimental beam profile as a function of two-color phase and relative polarization between fundamental and SH. For a qualitative understanding, we find that all observations can be rationalized by the single-atom response in terms of trajectory selection and gating the tunnel ionization window in two-color laser fields.

The control of divergence and yield of high-harmonic generation will be hugely beneficial for attosecond science and lensless imaging with HHG sources. Pump-probe experiments with two attosecond pulses from HHG, sometimes dubbed the "holy grail of attosecond science", have made tremendous progress [61, 168], but remain challenging because the peak intensities attainable with individual pulses from HHG are relatively low. All experiments that aim at attosecond pump-probe or nonlinear processes in the extreme-ultraviolet and soft X-ray range will benefit tremendously from our two-color strategy to achieve brighter HHG with higher-quality foci. Many imaging applications need a small focus, as too large a field of view can come at the expense of the resolution. In addition, a nonclean (i.e. not mono-Gaussian) focus can cause problems in image-reconstruction algorithms that do not directly retrieve the beam, and it will always cause problems when a fine detail embedded in a larger structure is imaged, where a non-mono-Gaussian focus would create imaging artifacts due to diffraction from the surrounding structures. Improvements of the focusing of HHG are not limited to two-color fields, but extend to any manipulation in the HHG process that favors trajectory selection or allow gating of the ionization rate. This seems to be the beginning of a larger effort, as recent papers have highlighted the importance of understanding [148, 149] and improving the microfocusing of HHG [169].

5

Solid-State High-Harmonic Generation from Structured Silica

Parts of this chapter have been published in Phys. Rev. Lett. **128**,223902 (2022)

5.1. Introduction

Attosecond science and strong-field physics are undergoing a revolution through the recently discovered generation of high harmonics in solids [36, 37, 170]. Until now, high-harmonic generation (HHG) from dielectrics was shown to generate photon energies well into the extreme ultraviolet (XUV) photon energy range [40, 58, 171]. The flexibility associated with solid samples consequently promises achievements beyond those of gas-phase HHG [14], which enabled femto- and attosecond timescale [19, 128–130, 172] studies, and all-optical nanoscale XUV imaging [27, 131]. All XUV experiments that rely on post-generation beam shaping are currently challenged by the lack of suitable optical elements: Refractive optics are limited by the high absorption of materials in the XUV and were only recently demonstrated by gas expansions with a spatially varying density profile close to a resonance [169]. Diffractive XUV focusing through binary amplitude shaping has recently been demonstrated for polychromatic HHG pulses [173]. However, binary diffraction elements are challenged by low efficiencies (10% for gratings [174]), whereas purely phase shifting elements would provide higher efficiencies (41% for gratings) but their realization is impractical due to the extremely short attenuation lengths in the XUV.

The possibility to nano-structure the emitting medium in solid HHG opens up the path towards tailored emission profiles, and to directly generate XUV patterns inside structures for imaging unknown objects through diffraction with sub-fundamental-wavelength resolution. First steps have been undertaken in HHG from engineered surfaces, albeit at relatively low photon energies and from larger structures [50–53, 175–178]. In this chapter, we introduce and demonstrate XUV science of nanostructures by HHG. We show how the diffracted emission patterns can be quantitatively understood and modeled, and use this knowledge for first demonstrations to control the phase, amplitude, and polarization of the emitted XUV pulses at will. Moreover, we introduce XUV generation from complex structures and use the measured patterns to reconstruct the underlying nanoscale structures. Our results demonstrate profile retrieval in all three dimensions, paving the way towards imaging and semiconductor wafer metrology through solid-state HHG from structured materials.

5.2. Control over the phase and amplitude of the XUV

To generate diffractive high harmonics in the XUV we focused 800 nm femtosecond pulses onto a grating-structured (10 μm pitch, 5 μm linewidth, 85 nm height) fused silica sample (112 ± 3 μm thick), as shown in Fig. 5.1. Only odd harmonics orders are observed, because fused silica appears isotropic to HHG due to its small crystal-domain sizes. The absorption length in silica at the generated wavelengths is less than 20 nm [117], hence effective harmonic emission takes place only close to the interface between silica and vacuum at the rear surface, and phase matching over an extended volume of the emitted XUV is negligible. For more details on sample fabrication, see Appendix B.

When the sample is oriented such that the flat surface faces the impinging pulses (Fig. 5.2a), harmonic orders 7 (H7), 9, and 11 are diffracted onto the detector (Fig. 5.2b). At the structured rear surface, diffraction originates from a transverse phase modulation

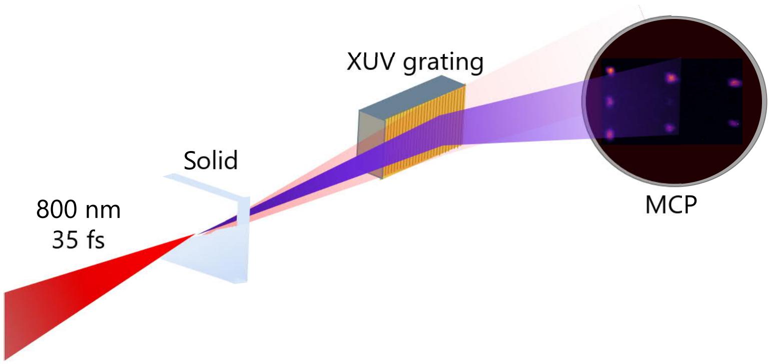

Figure 5.1: Experimental setup for generation of diffractive solid-state high-harmonics from structured solids.

of the XUV emission, which is introduced by the optical path-length difference of the grating grooves, and therefore has a periodicity equal to the pitch of the grating. We simulated diffraction patterns (Fig. 5.2d) using an analytical model (Fig. 5.2c), assuming a phase grating in the near field.

We start with describing the electric field of harmonic order q in general as $E_{xuv} = A_{\text{xuv}} e^{i\phi_{\text{xuv}}}$, with amplitude A_{xuv} and a phase ϕ_{xuv}. In general $\phi = \frac{2\pi y}{\lambda} n$, in which y is the propagation distance, λ the wavelength and n the refractive index. The wavelength of harmonic q is related to the fundamental wavelength by $\lambda_{\text{xuv}} = \frac{\lambda_{\text{IR}}}{q}$, such that we can define $\phi_{\text{xuv}} = q\phi_{\text{IR}}$. The phase of the harmonics at the interface between bottom grooves and vacuum is:

$$\phi_{\text{xuv},\sqcup} = q\phi_{\text{IR},y=0} + \phi_{\text{xuv},y=h} + \phi_{\text{arb.}}, \tag{5.1}$$

and for harmonics generated in the top grooves:

$$\phi_{\text{xuv},\sqcap} = q\phi_{\text{IR},y=h} + \phi_{\text{arb.}}. \tag{5.2}$$

It is possible that an extra phase is transferred from the fundamental to the harmonic, which we define here as $\phi_{\text{arb.}}$. We assume that this phase is the same for the top and bottom groove, thus canceling out when calculating the phase difference between the two grooves:

$$\Delta\phi_{\text{xuv}} = \phi_{\text{xuv},\sqcup} - \phi_{\text{xuv},\sqcap} = \frac{2\pi h}{\lambda_{\text{xuv}}}(1 - n_{\text{IR}}). \tag{5.3}$$

This phase difference defines a binary phase grating, with a pitch of 10 µm. The amplitude of the fundamental field has a Gaussian envelope, with a FWHM of 100 µm. The phase of the fundamental field is flat, as generation of the harmonics occurs at the focal plane. Far-field diffraction patterns are then calculated by using Fourier transformation, following Fraunhofer diffraction theory, resulting in Fig. 5.2(d).

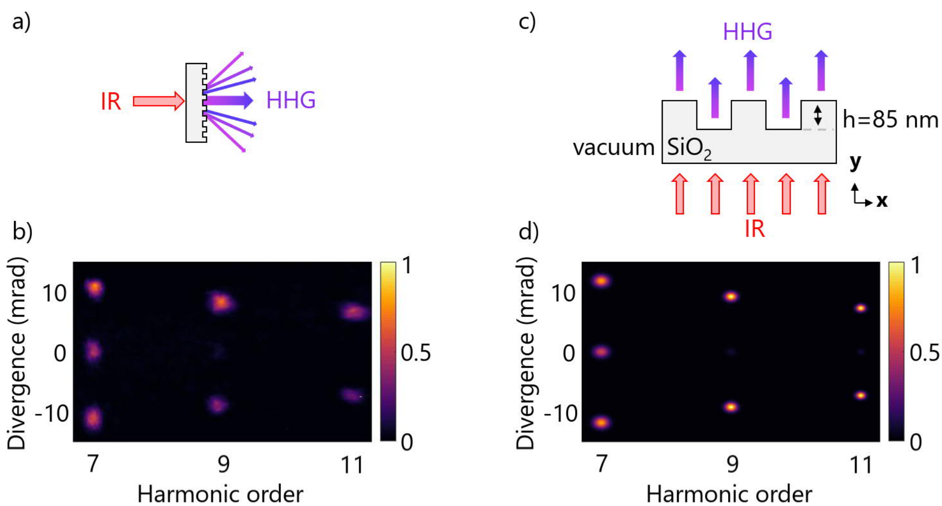

Figure 5.2: (a,b) Diffracted high harmonics generated inside the grating-structured rear surface. The color scale represents normalized intensity. (c) Analytical model used to simulate the diffraction. (d) Simulation of HHG diffraction from a near-field phase grating. The color scale represents normalized intensity.

The excellent agreement of photon-energy dependent diffraction angles and efficiencies between experiment and simulation confirms our model. The generation of HHG directly inside the diffractive grating-structured silica, which then entails a pure phase grating, leads to extremely efficient first-order diffraction. Specifically for H7, H9, and H11, the percentage of the sum of the signal diffracted into the first orders, compared to the sum of both the first and zeroth-order signals, is 70 %, 90%, and 97%, respectively. We expect to also diffract light into the third orders and higher orders, but are unable to measure these orders in the present experimental configuration. For H9 and H11 only little signal is diffracted into the zeroth order, which resembles the situation of the theoretical maximum of 41% diffraction efficiency in each first order [174].

The depth of the grooves of the grating can also be reconstructed from the measured wavelength-resolved diffraction efficiencies in Fig. 5.2b. We employ an analytical model which allows to extract the modulation depth of a binary phase grating, and therefore the height of the grooves, with prior knowledge of only the refractive index of the bulk and the central wavelength, see Fig. 5.3. The model starts with describing the unit cell of a binary phase grating [179], with pitch Δ and linewidth b, as

$$f(x) = [\mathrm{rect}(\frac{x}{b}) \circledast \delta(x + \frac{b}{2})] + [\mathrm{rect}(\frac{x}{\Delta - b}) \circledast \delta(x - \frac{\Delta - b}{2})]e^{i\phi}. \tag{5.4}$$

When convoluted with a comb function, this expression describes an infinite phase grating, in which the phase depth between two neighbouring grooves is set as ϕ. The Fourier transform of this expression gives the amplitude of each diffracted order in the far field:

$$[F(q)]_{q=\frac{m}{\Delta}} = \frac{\sin(m\phi/2)}{m\phi/2}[i\sin(m\phi/2)]. \tag{5.5}$$

By dividing the intensity of the first order, I_1, with the intensity of the zeroth order, I_0, we can solve for ϕ:

$$\phi = 2\arctan(\frac{\pi}{2}\sqrt{\frac{I_1}{I_0}}) \tag{5.6}$$

Combined with the equation for the phase, eq. 5.3, we obtain an expression for the height, given by the measured intensities of the first and zeroth order of the diffraction signal, per harmonic wavelength λ_{xuv}.

$$h = \frac{\lambda_{\text{XUV}}}{(n_{IR}-1)\pi}\arctan(\frac{\pi}{2}\sqrt{\frac{I_1}{I_0}}) \tag{5.7}$$

The three harmonic orders give an average height of 76 nm (Fig. 5.3), which is close to the value of 85 nm measured with a profilometer. This demonstrates that HHG can be utilized as a tool for direct height metrology of a periodic sample through phase control of the XUV generation.

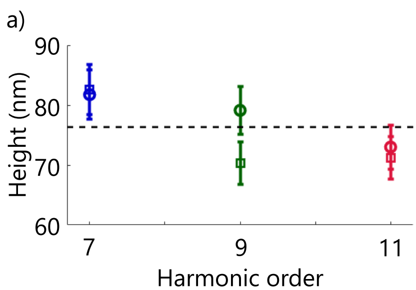

Figure 5.3: Height reconstruction, using the data from panel Fig. 5.2b

We now turn to a configuration where the sample is oriented such that the infrared pulses impinge on the structured surface first and harmonics are emitted from the rear flat surface (Fig. 5.4a). The structured front surface imprints phase modulation onto the infrared beam, which translates into amplitude modulation on the flat rear surface, leading to diffraction patterns with the same emission angles, but markedly different intensity distributions (Fig. 5.4b) compared to the previous configuration (Fig. 5.2a,b). To calculate the diffracted far-field pattern, we assume a flat phase for the fundamental, prior to interaction with the grating. The grating imprints a phase modulation onto the field, but the phase is now only determined by the wavelength of the fundamental and

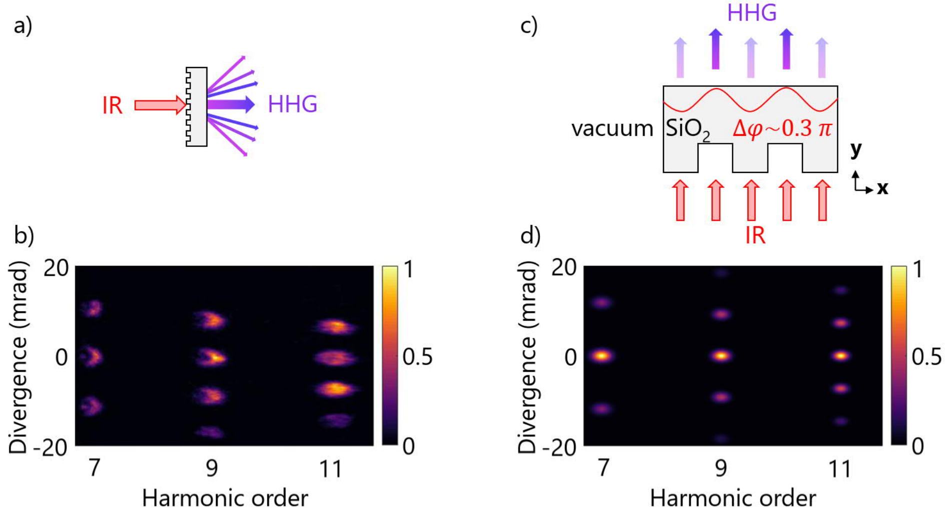

Figure 5.4: (a,b) Diffracted high harmonics generated by a phase grating imprinted infrared pulse. (c) Analytical model concept. (d) Simulation of HHG diffraction from a near-field amplitude grating. The color scale represents normalized intensity.

the refractive index at 800 nm. To determine the fundamental field amplitude and phase at the generation interface, we use Fresnel diffraction to propagate the field through the sample. This leads to a sinusoidal modulation of the amplitude and phase difference of about 0.3π rad of the fundamental at the flat side of the sample. Subsequently, amplitude and phase of the XUV field are calculated as follows:

$$E_{\mathrm{xuv}}(x) = A_{\mathrm{IR}}(x)^{q} e^{iq\phi_{\mathrm{IR}}(x)}, \tag{5.8}$$

where the harmonic field E_{XUV} is set by the amplitude of the fundamental $A_{\mathrm{IR}}(x)$ to the power of q, the harmonic order. The phase is calculated by multiplying the fundamental phase times the harmonic order. The perturbative dependence of the harmonic field on the fundamental field is justified by earlier experimental observations [40], in which HHG in silica is described by semiclassical intraband carrier dynamics, which also results in a nonlinear perturbative dependence. Far-field diffraction is then calculated using Fraunhofer diffraction, leading to the simulated pattern in Fig. 5.4d. HHG is effectively driven by a periodically modulated intensity distribution of the fundamental field, which facilitates the emission of both odd and even diffraction orders (Fig. 5.4b, due to a limited field-of-view in the detection, we did not observe the even orders of H9 and H11 for positive divergence angles), whereas even diffraction orders are absent for the XUV phase grating with 50% duty cycle in Figs. 5.2. As before, experimental intensities and simulations (Fig. 5.4b,d) show good agreement.

In both configurations, the odd diffraction orders originate from modulations with a periodicity of 10 µm, the pitch of the grating. In addition, even diffraction orders appear

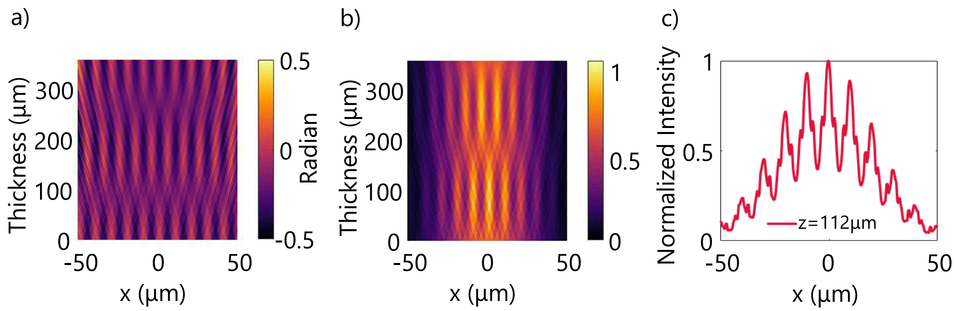

Figure 5.5: (a) Evolution of fundamental phase as a function of sample thickness. (b) Intensity distribution as a function of sample thickness. The color scale represents normalized intensity. (c) Intensity distribution at the thickness of our sample, 112 µm.

as a cause of a modulation in the fundamental near field with a periodicity of 5 µm. We attribute this faster modulation due to the Fresnel propagation that repeats the initial phase grating after regular distances [180, 181], the so-called Talbot length $z_T = 2na^2/\lambda$ (a is the pitch of the grating, n the refractive index). For our parameters this means the phase grating is imaged after a distance of 363 µm. Half way the Talbot length, at 181 µm, the grating is imaged with a π phase shift, see Fig. 5.5a. This translates to modulations in the intensity of the fundamental field which are also shifted with respect to the initial amplitude modulations, see Fig. 5.5b. At the thickness of our sample, 112 µm, the intensity distributions (Fig. 5.5c) shows modulations with a periodicity of 5 µm, causing the emission of even diffraction orders at the flat exit surface due to breaking of the original 50% duty cycle of the grating.

Additionally, the sinusoidal modulation of the amplitude imparted onto the fundamental field, determined by the geometric parameters of the grating structure and the sample thickness, gives rise to higher local power density, thus enhancing the conversion efficiency of light pulses at the fundamental frequency to HHG by about a factor of 2. Figure 5.6a shows a direct comparison between the divergence-integrated spectra generated in such configuration and spectra generated in a flat bulk material, with equal sample thickness. The enhancement is most pronounced for higher harmonic orders due to the nonlinear HHG process. For the configuration in which generation occurred in the structured surface, no significant enhancement was visible (Fig. 5.6b).

We have thus far shown the generation of structured XUV light and explained the underlying mechanism in periodic structures larger than the wavelength of the fundamental driving laser. We also demonstrated the ability to use the emitted harmonics to sense the amplitude distribution of the fundamental field at the generation interface and to reconstruct height profiles. We now turn to investigating light-matter interaction of intense femtosecond pulses with periodic structures with characteristic sizes smaller than the driving wavelength, in which the fundamental near field will be shaped by the geometry of the structure, which provides opportunities for controlling not only amplitude and phase, but also the polarization state of the emitted XUV light.

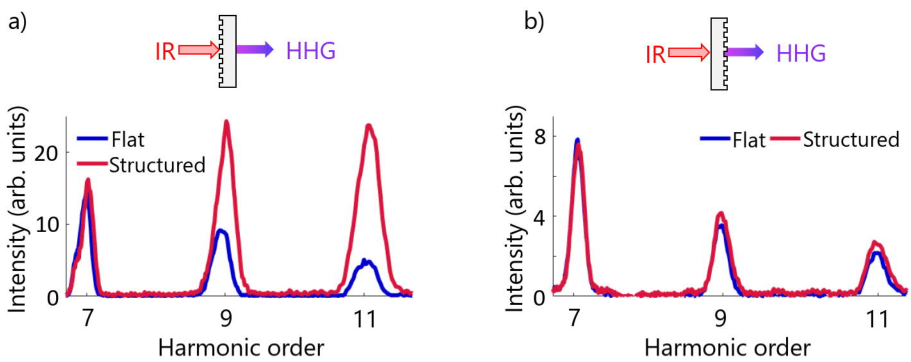

Figure 5.6: (a) Comparison of signal from flat and structured surface as generated in the configuration of Fig. 5.4. (b) Comparison of signal from flat and structured surface as generated in the configuration of Fig. 5.2.

5.3. Generation from nanostructured silica

Generation inside a nanostructured fused-silica grating with sub-fundamental-wavelength dimensions (400 nm pitch, 200 nm linewidth, 85 nm height, Fig. 5.7a) is shown in Fig. 5.7.

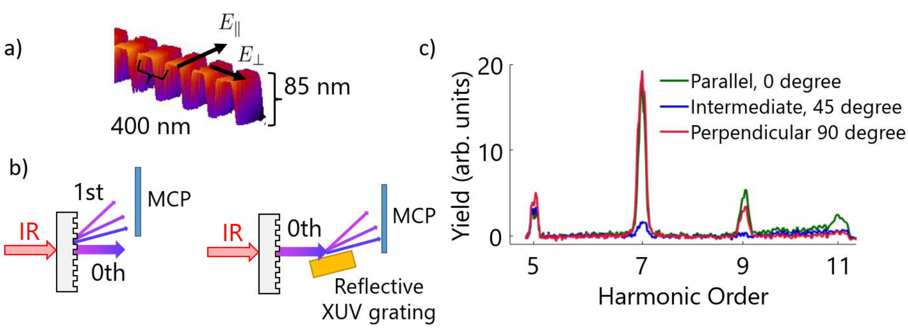

Figure 5.7: (a) AFM image of the structure. (b) Schematic of setup, for detecting zeroth and first-order diffraction. (c) Polarization-dependent HHG.

We observed first-order diffraction of the harmonics, when emission occurred on the structured side (Fig. 5.7b). This demonstrates that also with these sub-fundamental-wavelength dimensions a phase grating can be imprinted onto the XUV wavefront, similar as in Fig. 5.2b. The signal was absent when the structure was facing the incoming pulses, thus the mechanism of imprinting amplitude modulation on the fundamental wavefront (Fig. 5.4b) does not apply here, since the structural features are too small for the fundamental wavefront to diffract from. For 400-nm pulses, diffractive harmonic

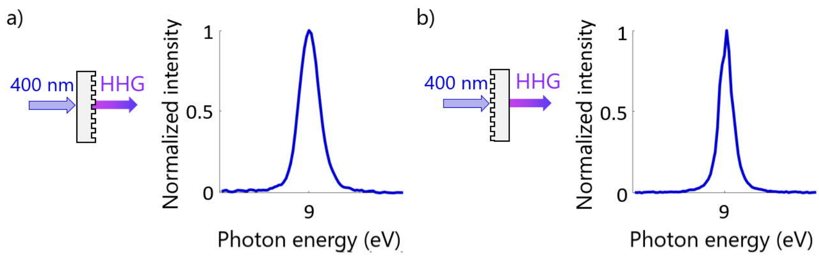

Figure 5.8: First order diffraction of H3 of 400 nm, from a fused silica grating with 400 nm pitch. (a) Generation occurs at the flat side. (b) Generation occurs at the structured side.

emission at both the flat and at the structured side is possible (Fig. 5.8). The diffractive XUV generation is caused not only by phase modification, but also by the near-field amplitude of the 800-nm pulses at the structured exit surface, which represents a powerful new control mechanism over XUV emission.

We demonstrate this by changing the near-field of the 800-nm pulses in the nanostructures at will by changing the polarization of the incoming pulses with respect to the grating grooves. We measured the polarization-dependence of HHG through detecting both the first and zeroth-order diffracted harmonics, as shown in Fig. 5.7b, left and right panel, respectively. The yield of the first diffraction orders (Fig. 5.7c) for three different polarization angles (0° (parallel with grooves), 45°, and 90° (perpendicular to grooves)) shows a significant dependence for each harmonic, demonstrating that the polarization indeed acts as a control parameter for XUV generation. In more detail, we observe that all harmonic intensities maximize at 0°, except for the zeroth-order of H7 and the first-order of H5, which minimize at this angle (see Figs. 5.9a,b). The common features among the polarization dependent intensities of the harmonics can be attributed to the effect of the sub-wavelength structure on the fundamental field distribution, which we simulated (see Appendix C) for parallel, intermediate, and perpendicular orientations, as shown in Figs. 5.9c,d,e, respectively. For a perpendicular orientation the field is localized between the grooves, whereas for parallel orientation the field is concentrated inside the grooves. Consequently, the minimum signal for intermediate polarization angles around 45° in Figs. 5.9a,b arises from a less efficient generation of the harmonics, which is caused by the splitting of the fundamental field amplitude between the top and bottom grooves. Based on the near-field simulations in Figs. 5.9c,d,e, we simulated the zeroth and first order diffracted harmonic signals, which are shown in Figs. 5.9f,g. The simulations accurately capture the increased XUV generation at 0°and 90° and a minimum signal for intermediate polarization angles around 45°. A convergence study (see Appendix C) furthermore demonstrates fully converged simulations. Thus, we have shown that HHG can indeed be controlled by modifying the fundamental near-field distribution by changing the incoming polarization, and inversely this distribution can be probed using diffracted HHG.

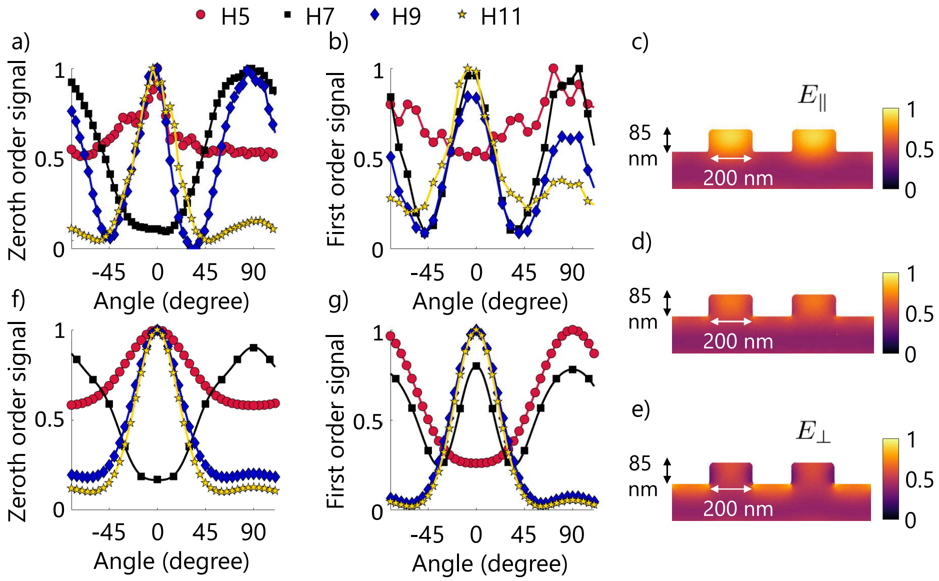

Figure 5.9: (a) Polarization-dependent zeroth-order diffraction. (b) Polarization-dependent first-order diffraction. (c,d,e) Simulation of the near-field of 800 nm, when polarized parallel, at 45°, and perpendicular to the grooves, respectively. The color scale represents the intensity, normalized to the maximum intensity of the parallel configuration. (f,g) Simulated polarization-dependent zeroth and first-order diffraction signals.

Some intensity dependencies in Figs. 5.9a,b stand out and require deeper analysis: We observed a relatively weaker modulation of H5, which is below the band gap of silica and thus generated over a much longer interaction length than other harmonics. This leads to greater contributions from the unstructured bulk of the silica as compared to generation in the vicinity of the structured surface, thus reducing the overall intensity modulations as a function of angle between polarization and grooves, as reproduced by the simulations in Figs. 5.9f,g. Another intensity dependence that requires further analysis is that of H7, which minimizes at 0°. H7 is just above the band gap of silica, so the cascaded frequency conversion steps and their interference may become relevant [182], as intermediate lower harmonics can be generated over the entire interaction length of the solid medium. We modeled H7 as interference between the direct upconversion of seven 800 nm photons, sum frequency generation of the fundamental and twice H3 for the first cascaded step, and H5 and twice the fundamental for the second cascade (see Appendix C), which reproduces the experimental data well. Inclusion of cascaded processes could possibly resolve discrepancies between experiments and simulations for other harmonics too, e.g. H9. Such a simulation would be challenged by the larger number of cascaded processes, and goes beyond the scope of our study, but may stimulate new theories.

The redistribution of field amplitudes along parallel and perpendicular components is reminiscent of a form birefringence of the nanostructured grating, which thus acts as a waveplate for the generated XUV pulses. The agreement between our simulations in Figs. 5.9f,g and experimental data in Figs. 5.9a,b lends confidence to ascribing polarization states to the emitted harmonics, which are extracted from the simulations. Table 5.1 summarizes the Stokes parameters of the zeroth and first diffraction order of all harmonics for the incident fundamental polarization angle of 45 degrees. Different harmonics exhibit various degrees of elliptical polarization. For example, the zeroth-order of H5 is almost purely linearly polarized at 45°(Stokes parameter U), and intuitively expected as H5 is emitted over the unstructured bulk where no form birefringence occurs. On the other hand, the contribution of the circular polarization component (Stokes parameter V) exceeds 70% in the first-order of H9 and H11. As the nonlinear susceptibility tensors for HHG in amorphous silica represents an isotropic medium, the elliptical polarization can only be attributed to structurally induced phase retardation between polarization components parallel and perpendicular with respect to the grating. These experiments and simulations have shown that HHG is sensitive to the geometry of the structure, and therefore can be used to investigate near-field effects. We foresee that using HHG to directly image the near-field distributions would allow to further characterize the effects of strong field confinement [52, 53], offering a new platform for ultrafast physics in nanostructured solids.

Stokes parameters	Zeroth diffraction order				First diffraction order			
	H5	H7	H9	H11	H5	H7	H9	H11
$\lvert Q\rvert^2$	0.000	0.060	0.002	0.004	0.007	0.825	0.099	0.098
$\lvert U\rvert^2$	0.996	0.562	0.606	0.537	0.943	0.065	0.200	0.174
$\lvert V\rvert^2$	0.004	0.379	0.392	0.459	0.050	0.110	0.701	0.727

Table 5.1: Polarization state of the zeroth and the first diffraction order for harmonic orders generated with 45 degree angle between polarization and grooves. The squared moduli of Stokes parameters Q, U, V (corresponding to the contributions of linear 0-90 degree, linear ±45 degree, and circular polarization states, respectively) are shown, normalized by squared modulus of the I parameter (corresponding to the total field intensity).

5.4. Imaging of nanostructures

Here we take the first step into this direction and demonstrate direct imaging of periodic and aperiodic structures through harmonic emission. We chose a complex aperiodic structure ('smiley') patterned in silica by e-beam lithography shown in Fig. 5.10a. We generated with 400 nm, for which the third harmonic dominates the diffracted signal. If HHG was more polychromatic, spectral filters would be needed to select a certain harmonic, or Fourier-transform imaging [27, 183] could resolve the HHG spectrum pixel-by-pixel. The main beam is blocked out with a beam block, leading to the diffraction pattern of the smiley structure as shown in Fig. 5.10b. The calculated diffraction pattern (Fig. 5.10c) matches well with the experimentally measured one, showing the same significant features of the diffraction pattern. In Fig. 5.11a, the diffracted pattern is generated from an array of micron-sized pillars, with 2 μm dimensions, spaced four

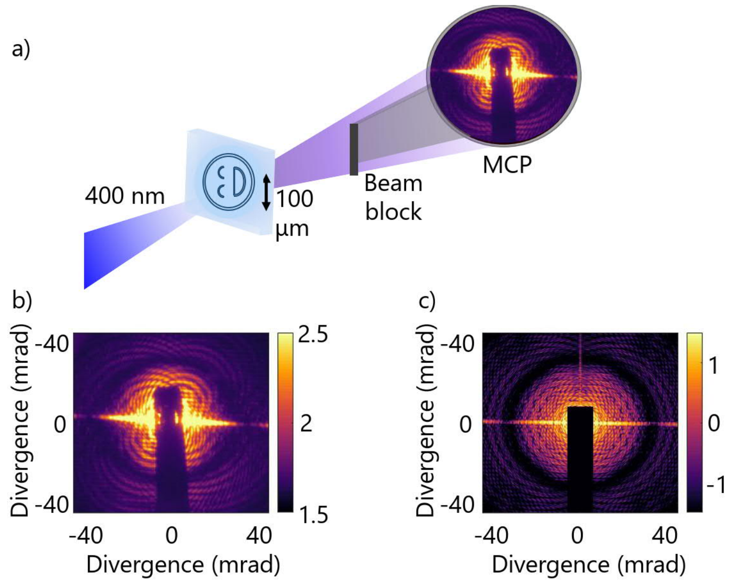

Figure 5.10: (a) Schematic of experimental setup. (b) Measured diffraction pattern of target in (a). (c) Simulated diffraction pattern of target in (a). The color scale represents intensity on a logarithmic scale.

micrometers apart. In this particular diffraction pattern, the beam block will not block out any other diffraction signal, except the zeroth order, easing the reconstruction of the structure. The image reconstruction through a phase retrieval algorithm [184, 185] in Fig. 5.11b correctly captures the orientation of the array, and the dimension as well as the spacing of the micron pillars. As a comparison, a microscope image of the pillar array is shown in Fig. 5.11c. Compared to other HHG-based imaging techniques [186], here we can generate diffractive HHG directly from the structure of interest, which offers a new imaging tool for the inspection of patterned surfaces in the XUV.

5.5. Conclusion and outlook

The control of phase, amplitude, and polarization in solid HHG from nanostructures will allow sensing and even imaging femtosecond-resolved [187] electric near-field distributions in dielectric metasurfaces [52] and nanostructures. Moreover, the opportunity to shape XUV pulse properties at will opens new perspectives for pulse shaping that are otherwise challenging to achieve by modifications after generation. In particular, the demonstrated phase control can inspire the design of new highly efficient phase diffractive elements, such as zone plates, which will be more efficient than the typically used binary elements. This approach of combined generation and shaping in a single element may soon compete with post-generation XUV shaping given the high efficiencies of XUV

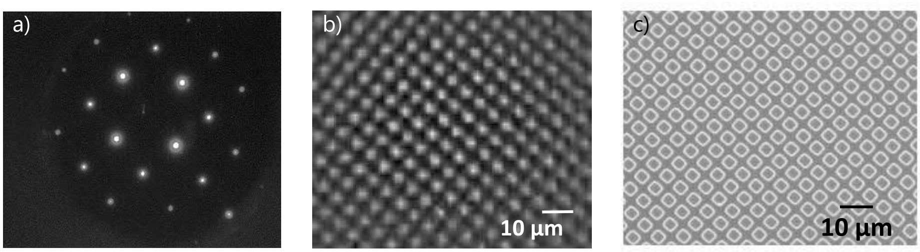

Figure 5.11: (a) Measured diffraction pattern of an array of micron-sized pillars. (b) Reconstructed surface. (c) Microscope image of the array of micron-sized pillars.

phase control [174] and the ongoing efforts to increase the efficiency of solid HHG [188, 189].

6

Efficient Extreme-Ultraviolet High-order Wave Mixing from Silica

This chapter has been submitted as a research article to Nat. Comm.

6.1. Introduction

The emission of high-order harmonics from solids [35–37, 40] under intense laser-pulse irradiation is revolutionizing our understanding of strong-field solid-light interactions [36, 37, 40, 48, 70, 96, 190], while simultaneously opening avenues towards novel, all-solid, coherent, short-wavelength table-top sources with tailored emission profiles and nanoscale light-field control [53, 191]. To date, broadband spectra have been generated well into the extreme-ultraviolet (XUV) [40, 57, 71, 188], but the comparatively low conversion efficiency still lags behind gas-based high-harmonic generation (HHG) sources [40, 188], and have hindered wider-spread applications. Here, we overcome the low conversion efficiency by two-color wave mixing. A quantum theory reveals that our experiments follow a novel generation mechanism where the conventional interband and intraband nonlinear dynamics are boosted by Floquet-Bloch dressed states, that make solid HHG in the XUV more efficient by at least one order of magnitude. Emission intensity scalings that follow perturbative optical wave mixing, combined with the angular separation of the emitted frequencies, make our approach a decisive step for all-solid coherent XUV sources and for studying light-engineered materials.

High-harmonic generation from gases has revolutionized ultrafast spectroscopy [129, 130], imaging science [27, 28], and is finding its way into first industrial applications [124, 125, 192], but is still limited by the low conversion efficiency from infrared to XUV photons. A thorough understanding of the mechanism of gas-based HHG spurred the use of sculpted multi-color drivers that favorably modify the ionization rate, and thus increase the conversion efficiency [124, 154, 158, 193, 194]. The mechanisms of solid HHG are still being debated. Different generation regimes exist, and are characterized by the choice of the driving field and generation material. Proposed mechanisms include nonlinear intraband currents [36, 40], arising from carrier acceleration by the strong field after band-gap excitation, electron-hole recollisions after carrier excursion [37, 96] creating an interband polarization, ionization-induced injection currents [70] for low-order harmonics, or treating emission as originating from dressed eigenstates in a strong static field, which under high excitation intensities drives Bloch oscillations, known as Wannier-Stark states [106]. The importance of carrier-injection dynamics in solid HHG [70], combined with the observation of enhanced gas HHG for short-wavelength drivers, which favorably modifies the ionization step [195] and thus enhances the conversion efficiency, points towards a new strategy for both enhancing the efficiency of solid HHG, as well as shedding light on the generation mechanism: two-color non-collinear XUV generation.

6.2. Experimental details

This section describes the experimental setup needed for two-color non-collinear XUV generation. The output of a Ti:sapphire amplifier (Coherent Astrella, 800 nm, 1 kHz) is split into two arms, see Fig. 6.1. In one arm, the second harmonic is generated inside a 200 µm thick β-barium borate (BBO) crystal. The second arm contains a delay line to optimize temporal overlap of the two pulses onto the sample. Half-wave plates are placed in both arms to ensure parallel polarization of both pulses. Focusing is achieved by means of a spherical mirror with focal length f=500 mm. The crossing angle of 17.5 mrad in focus is implemented by impinging onto the spherical mirror with the two beams parallel and displaced in height by 9 mm. The beam sizes are individually adjusted using irises so as to maximize the signal while preventing damaging the sample. This leads to a focal distribution of the second harmonic to be half the size of the fundamental at full-width at half maximum. The generated harmonics are spectrally dispersed along the horizontal direction with an aberration-corrected, concave, flat-field grating (1200 lines/mm) and detected by a double-stack micro-channel plate assembly, backed with a phosphor screen, which is imaged with a CMOS camera from outside the vacuum chamber.

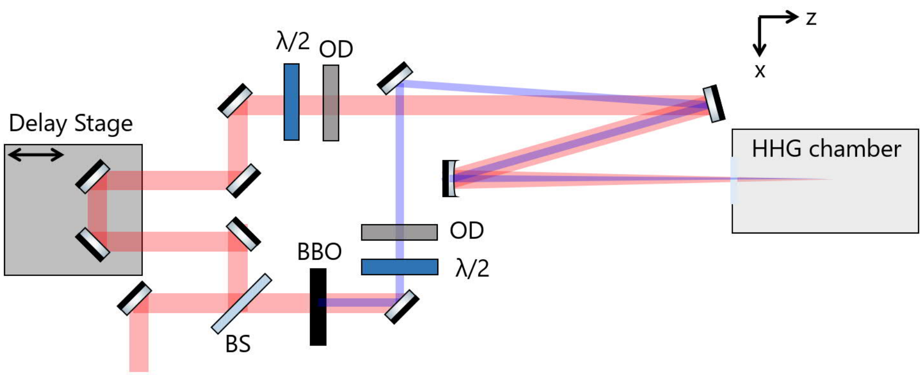

Figure 6.1: Experimental arrangement for two-color non-collinear wave mixing.

6.3. Results

6.3.1. Non-collinear two-color wave mixing

Similar to non-collinear HHG in gases [196, 197], the angle between fundamental (800 nm) and second harmonic (SH) (400 nm) driving pulses (Fig. 6.2) provides an angular separation of the photon channels and prevents their overlap and interference, unlike in collinear two-color HHG [198]. Non-collinear HHG leads to an emission pattern (Fig. 6.2) of harmonic wave mixing orders (WMOs) labeled (n, m). Three selection rules must be considered to understand non-collinear wave mixing spectra driven by the fundamental and its second harmonic, and to assign each harmonic WMO to a unique combination of photons.

Both wavelengths contribute to the emitted photon energies via an integer number of photons. From a simple energy conservation standpoint, the expected emission takes place at photon energies: $q\omega_f = n\omega_f + m2\omega_f = (n+2m)\omega_f$, where $q = n+2m$ is the harmonic order, ω_f is the angular frequency of the fundamental laser field, and n and m are the numbers of photons from the fundamental and its second harmonic, respectively. This yields a discrete spectrum, shown in Fig. 6.2b. Emission corresponding to even harmonics of the fundamental is present, despite the fact that fused silica is a centrosymmetric material. In fact, in a two-color field of commensurate frequencies, the parity conservation rule, which requires the total number of photons $n+m=$ to be odd, allows for generation of even harmonics of the fundamental through the addition (subtraction) of an odd amount of photons. The third conservation rule needed for a description of the full far-field profile shown in Fig. 6.2b, is conservation of the momentum. The harmonic spectrum spans less then an octave in energy, resulting into a unique mapping of each wave-mixing order (WMO) onto its emission angle β for a crossing angle α between fundamental and the second harmonic,

$$\beta(n,m) = \frac{2m\sin\alpha}{n+2m\cos\alpha}. \tag{6.1}$$

A small-angle approximation is used in Eq. 6.1.

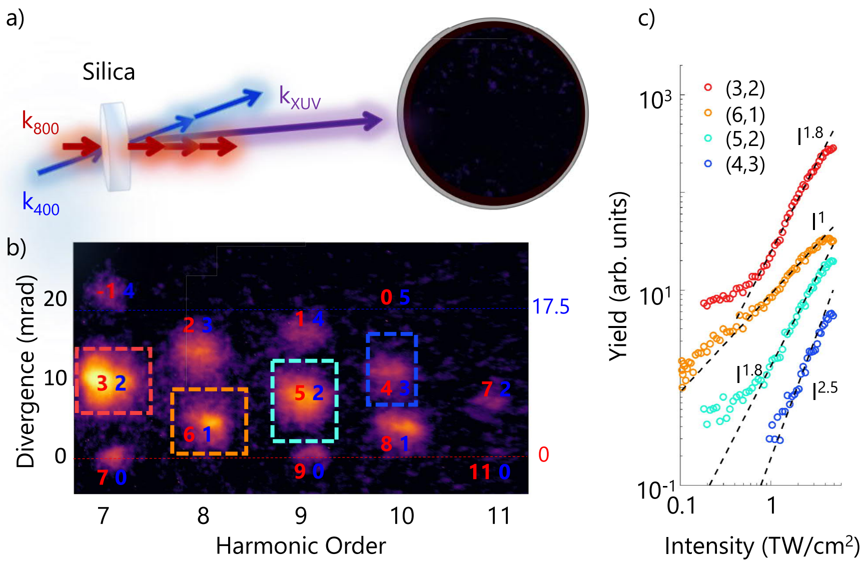

Figure 6.2: a) Experimental arrangement. b) Far-field spectrum of XUV wave mixing in silica. WMOs are spectrally dispersed in the horizontal direction and propagate freely in the vertical direction. WMOs generated only from 800 nm or 400 nm propagate at 0 mrad or 17.5 mrad, respectively. Harmonic orders refer to multiples of the 800-nm fundamental. c) Yield of different WMOs as a function of the intensity of the 400-nm pulse. The dashed lines are power laws, whose exponent is indicated in the plot. The different lines are vertically offset for clarity. The intensity of the 800-nm pulses was 11 TW/cm^2.

The emission patterns in Figs. 6.2a,b show strongly enhanced WMOs compared to the angularly separated emission from the respective fundamental beams, which are indicated by dashed lines in Fig. 6.2b. The separation of fundamental and SH photon channels in each WMO allows for identifying the effect of intensity scaling of the pulses on the harmonic emission, as shown in Fig. 6.2c for the scaling of the 400-nm pulse intensity - a first step in investigating and optimizing the photon-yield enhancement apparent in the WMOs. The yield of all WMOs faithfully follows a power-law trend over a large intensity range. The exponents of these power-law scalings (i.e. the slopes in a log-log plot) are close to the number m of 400-nm photons involved, which would be the exponent for the scaling of the yield as a function of intensity in perturbative optical wave mixing.

6.3.2. Simulation of two-color driven solid HHG

In order to understand the origin of the enhanced WMOs (Fig. 6.2b) and the perturbative intensity scalings (Fig. 6.2c) we solve the semiconductor Bloch equations [109] to simulate solid-state harmonic generation. The field-driven carrier population exchange between the bands leads to the generation of an interband polarization and an intraband current, see Chapter 2 for more details. This model was solved for a grid of points, which was spanned by the crossed 800-nm and 400-nm pulses that form a spatial interference grating. The resulting spatially modulated XUV emission was then propagated to the far-field by Fraunhofer diffraction (Fig. 6.3b), resulting in an excellent reproduction of the experimental wave mixing pattern (Fig. 6.3a).

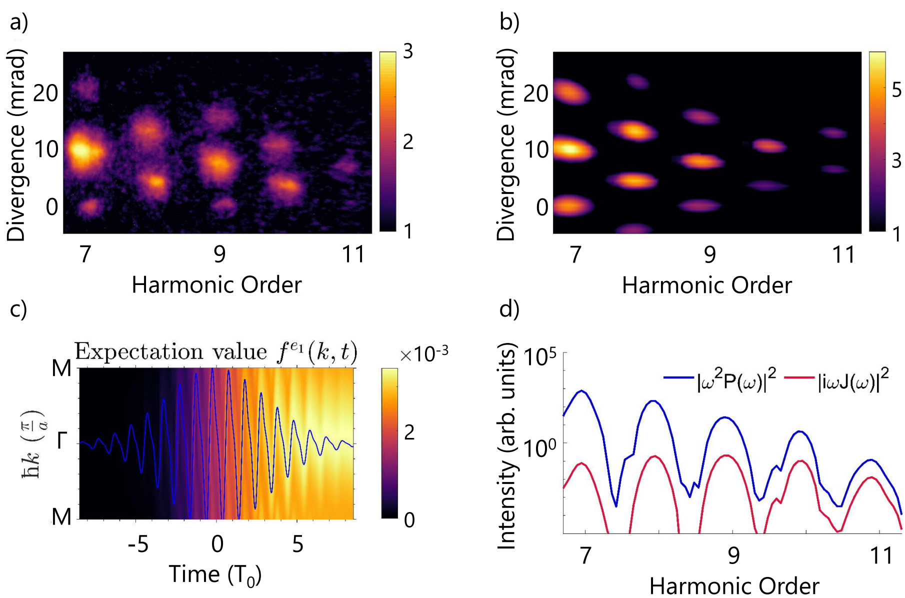

Figure 6.3: a) Recorded far-field spectrum, the color axis represents the yield on a logarithmic scale. b) Simulated far-field spectrum, the color axis represents the yield on a logarithmic scale. c) Simulated electron population $f^{e_1}(k,t)$ (normalized magnitude given by color axis) of the first conduction band along the Γ-M crystal direction, in momentum and time space. The blue line represents the vector potential of the laser pulse. T_0 denotes the cycle duration of the 800-nm pulse (2.7 fs). d) Comparison between the contributions of the interband polarization (blue) and intraband current (red).

Zooming into the attosecond electron dynamics in k-space that drive HHG, we observe that the intense two-color laser field excites carriers from the valence band to the first conduction band not just at the Γ-point but all across k-space. Simultaneously, the field accelerates the carriers along the energy bands, resulting in carrier trajectories in k-space that trace out the vector potential of the field (Fig. 6.3c). Due to the high ponderomotive energy the carriers are accelerated beyond the first edge of the Brillouin zone and undergo Bloch oscillations. The concentration of carriers at a given k-point undergoes rapid changes in time, inducing a high-frequency interband polarization that radiates light at high photon energies, see Fig. 6.3d. The radiation due to the carrier acceleration inside the bands, the intraband current, is significantly lower than the radiation from interband polarization for the harmonic energies measured in this experiment.

To identify which bands contribute most to the signal, we calculate the separate contributions of the interband polarization (Fig. 6.4a) and the intraband current (Fig. 6.4b)). Overall, the polarization dominates the emission in the spectral region around the bandgap (H5-H11). The main contribution of the intraband current originates from the carriers inside the first conduction band. The main contribution of the polarization is generated between the valence and the lowest lying conduction band. Both the interband and intraband mechanisms have in common that they are induced by laser-driven motion of carriers inside the bands. To identify if this laser-driven carrier motion gives rise to the perturbative intensity scalings, we model the harmonic emission originating only from the electron group velocity, which we describe semi-classically [34, 58] using a time-dependent crystal momentum which traces out the shape of the band during acceleration.

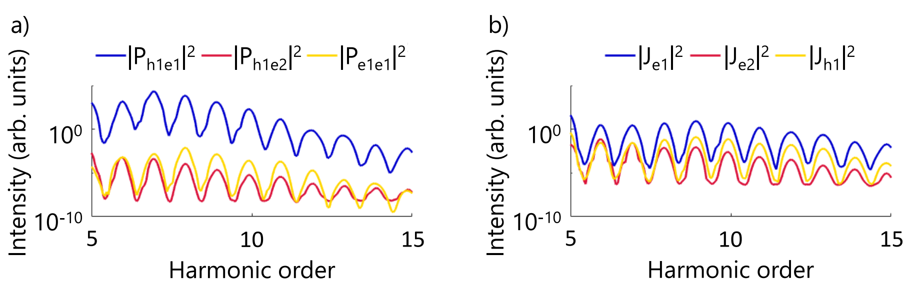

Figure 6.4: a) Separate contributions of the interband polarization. b) Separate contributions of the intraband current. The valence band and the two lowest lying conduction bands are denoted by the subscripts h_1, e_1, and e_2, respectively.

6.3.3. Perturbative intensity scaling in high-order wave mixing

A detailed investigation of the experimental (open circles) and semi-classically simulated (dashed lines) yields of the WMOs as a function of intensity of the driving fields is shown in Fig. 6.5. Figure 6.5a shows a scaling of the 400-nm pulses, wherein the intensity of the fundamental 800-nm field is kept constant. The dashed lines in Fig. 6.5 show that the simulated trend of a specific harmonic order (n, m) reproduces the highly nonlinear dependence of the scaled driving field. We observe saturation of the XUV yield at high intensities, when approaching the damage threshold.

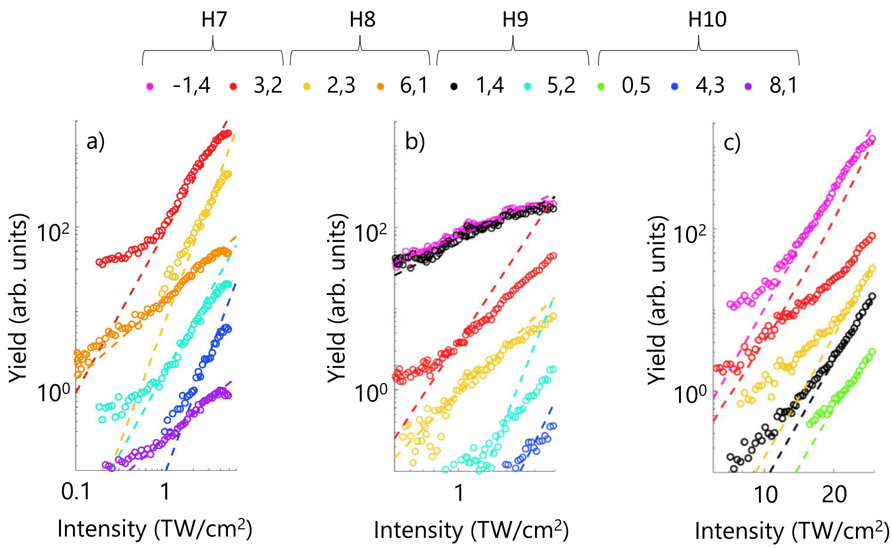

Figure 6.5: Experimental (open circles) and simulated (dashed lines) intensity scaling of different harmonic orders, in three cases: a) only the intensity of the 400-nm pulse is scaled (the ratio I_{400}/I_{800} varies between 0.01:1 to 0.4:1 from left to right on the horizontal intensity axis, I_{800}=11.0 TW/cm^2) b) only the intensity of the 800-nm pulse is scaled (the ratio I_{800}/I_{400} varies between 0.06:1 to 0.7:1 from left to right on the horizontal intensity axis, I_{400}=5.4 TW/cm^2), and c) the total intensity of two colors is scaled (the ratio I_{400}/I_{800} is 4.3:1). The color coding is consistent across the panels.

Next, experiments and simulations were performed for constant intensity of the 400-nm pulse, while the energy of the fundamental pulse is increased in steps. The behaviour in both experiment and simulations resembles that of a perturbative process. At the higher intensities, the fundamental and the SH foci may have lost some overlap, which leads to an overestimation of the 800-nm intensity involved in the wave mixing process and therefore lowers the power dependence. WMOs that contain more 800-nm photons deviate more severely from a pure power law, as observed for WMOs (4,3) and (5,2). Figure 6.5c shows a scaling of the total intensity, where the energy of the two pulses is increased independently in steps, to keep the ratio of intensities constant across the scan. The experimental data again show good agreement with semi-classical predictions, and reproduce the nonlinear dependence. More specifically, most orders follow a power law of 5 for these 5$^{\text{th}}$ order processes shown in Fig. 6.5c. The yield as a function of intensity is reproduced well for the entire intensity range. The scaling law of WMO (3,2) systematically shows a lower power dependence, possibly caused by a drift in the beams at higher intensities, which leads to an overestimation of the intensity. Intensity scalings of WMOs that contain fewer 800-nm photons are less affected by the drift.

The good agreement between experiments and simulations in Fig. 6.5 confirms that the laser-driven carrier motion drives the XUV generation of solid-state HHG, resulting in a perturbative scaling for large intensity ranges. This has important implications for XUV sources based on solid HHG. The perturbative response causes the yield of solid HHG as a function of driving intensity to rise with an exponent determined by the number of photons (n, m) involved in HHG. This enables selective enhancement of individual or a selection of WMOs, depending on the relative strength of the two driving fields. Together with the natural angular separation of WMOs, this illustrates that XUV wave mixing in solids can help to realize an all-solid single-element XUV generator and multi-wavelength beamsplitter, where different energy emissions are mapped onto different emission angles. Further separation of the remaining energies in a beam could be realized by the simple addition of a hard aperture, without the need for lossy metal filters.

6.3.4. Efficient two-color driven solid high-harmonic generation

Additionally, we deduce from experimental wave-mixing patterns a dramatic yield enhancement for WMOs, as compared to single-color harmonics. In Fig. 6.3a, WMO (3,2) is the most intense emission, whereas (5,2) is the most intense at a photon energy of 14 eV, and (7,2) is the most intense at 17.1 eV.

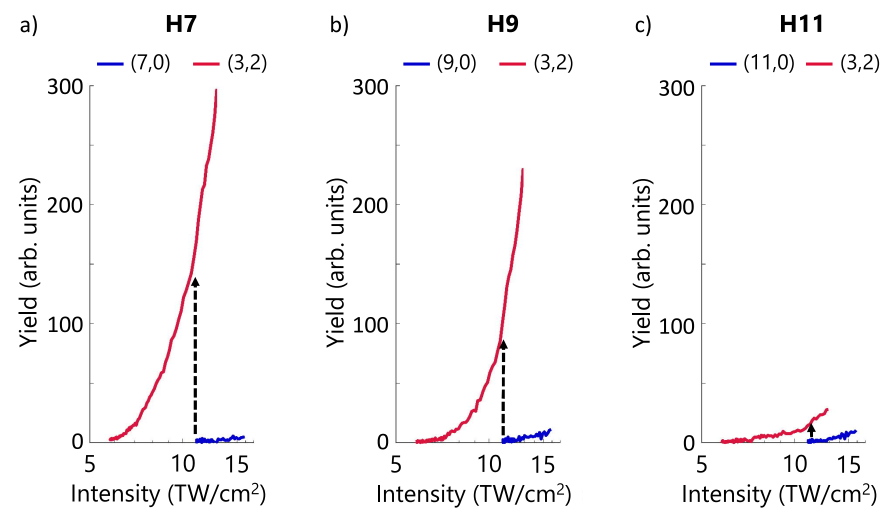

Figure 6.6: The yield of several harmonic orders (of the fundamental) at a) 10.9 eV, b) 14.0 eV, and c) 17.1 eV photon energy, as a function of total driving intensity. The blue curves represent on-axis harmonics, in which the 800-nm intensity is fixed around 11.0 TW/cm^2 and the 400-nm intensity is increased from 0 TW/cm^2 to about 5 TW/cm^2. The red curves represent WMOs at the same photon energies (10.9 eV, 14.0 eV, and 17.1 eV, respectively) in which the 400-nm intensity is fixed around 5.4 TW/cm^2 and the 800-nm intensity is increased from 0 to 7.5 TW/cm^2.

In order to estimate how much brighter the WMOs are, we compare the yield of a WMO with the yield of an on-axis harmonic generated at the same photon energy and total intensity, see Fig. 6.6. To obtain the fairest comparison, we compare scans where HHG is exclusively driven by the fundamental 800 nm pulses and in which the total intensity is build up from both driving wavelengths. Both scans were taken under similar experimental conditions. More specifically, we compare scans where the intensity of the 800-nm pulse is around 11.0 TW/cm^2 and the intensity of the 400-nm pulse is varied (blue lines in Fig. 6.6). At this 800 nm intensity, the efficiency of HHG driven by 800 nm alone is close to maximal and the main on-axis harmonics (orders (7,0), (9,0), and (11,0)) are always present, and their yield does not change significantly by addition of the second color. Scans in which the intensity of the 800-nm pulses is scaled and the intensity of 400 nm is kept constant (red lines in Fig. 6.6) start at lower intensity of the 800 nm pulses and the WMOs show a dramatic increase in yield. Comparing the yield of the WMOs as a function of total driving intensity (fundamental and SH intensity combined) with the yield of on-axis harmonic orders at the same photon energy and total driving intensity, provides the enhancement factors. The yield of order (7,0) is only a few arbitrary units at an intensity of 11.0 TW/cm^2. At the same total intensity, which now consist of both fundamental and SH intensity, the signal of WMO (3,2) has a yield of about 170 (arbitrary units), leading to an enhancement factor of 85. An enhancement factor of about 50 is found for H9, shown in Fig. 6.6b, in which the on-axis harmonic (9,0) has a single-digit yield, whereas the WMO (5,2) shows a yield of around 100. For H11 the enhancement is least pronounced, the signal of the WMO (7,2) is about 7 times larger then the on-axis harmonic (11,0). Overall we are confident to report an increase of the WMOs with at least one and up to two orders of magnitude compared to the on-axis harmonics for H7 and H9, and about half an order of magnitude for H11. Extrapolating from the conversion efficiencies of 10^{-6}-10^{-7} that have been reported for silica and single-color HHG with a near-infrared driver in the same photon energy range [188], this places the conversion efficiency of wave mixing from silica well into the 10^{-5}-10^{-6} range, which is comparable to gas-phase sources.

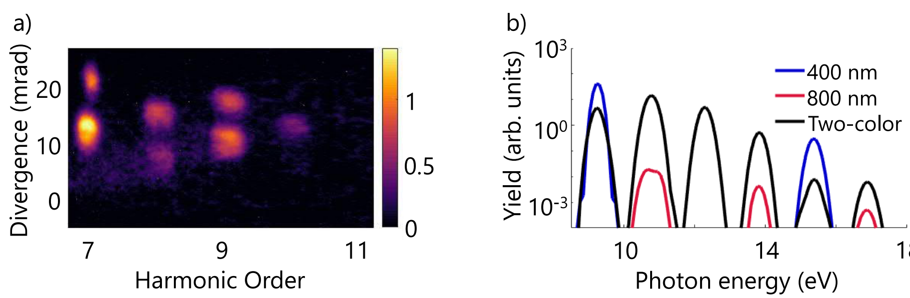

Figure 6.7: Comparison of 800-nm 400-nm driven solid-state high-harmonic generation a) Wave mixing with equal 400-nm and 800-nm intensity of 5.4 TW/cm^2. The color axis represents harmonic yield on a logarithmic scale. b) Simulated spectra, comparing 400-nm, 800-nm and two-color driving with equal intensity.

The aforementioned laser-driven carrier motion alone - which is a hallmark of mechanisms discussing both intraband currents and interband polarizations - does not account for this yield enhancement. For a more in-depth investigation what causes this unusual high efficiency of WMOs, we first verify experimentally the relative importance of both driving wavelengths. The separation of fundamental and SH photon channels in WMOs allows to identify that harmonic generation is more efficient for short-wavelength drivers. If we generate with both the fundamental and SH field at equal intensities (each 5.4 TW/cm^2), we observe that the dominant harmonic emission occurs within WMOs that are along the 400-nm divergence direction shown in Fig. 6.7a, signaling a dominant contribution of the 400-nm field to the WM pattern. Simulations for equal intensity of 800-nm, 400-nm or two-color pulses in Fig. 6.7b indeed confirm that aiding HHG by adding a shorter wavelength leads to the highest harmonic emission.

Comparing the momentum and time-resolved photocarrier excitation for 800-nm and 400-nm pulses in Figs.6.8a,b, we make two observations: First, the use of a short driving wavelength increases the ionization probability and thus the number of excited carriers. Second, the shorter driving wavelength accelerates carriers across k with a higher frequency, leading to enhanced carrier concentration around the Γ-point, where the band curvature facilitates both large carrier velocity and acceleration. This combination of increased photoexcitation, and high-frequency light-induced carrier motion results in a larger polarization for shorter driving wavelengths, giving more efficient high-order harmonic emission in the XUV, shown for 800 nm and 400 nm in Figs. 6.8c,d, respectively. Mixing two driving fields additionally leads to the advantageous combination of high yield and broad spectral coverage. The driving force of enhanced carrier concentration is most clearly seen from the k-resolved and energy-resolved polarizations in Figs. 6.8c,d. Driving HHG with 400 nm (Fig. 6.8b) supports Floquet-Bloch states [103] where the bands are dressed with multiples of the driving photon energy. Transitions between such states gives rise to the polarization signals at energies of multiples of the k-dependent band energies, clearly visible in Fig. 6.8d. This contrasts to the situation with 800 nm, where the strong driving and longer wavelength allows for the carriers to accelerate beyond the Brillouin zone edge. Therefore Wannier-Stark states - the eigenstates in a quasi-static electric field of an electron undergoing Bloch oscillations - are a more appropriate basis where dressing by multiples of the Bloch frequency occurs [106]. This illustrates that the shorter driving field operates further in the multiphoton regime providing assistance to more efficient carrier excitation and thus overall boosting HHG emission intensity. Microscopically, this has important ramifications that can stimulate new theories: While Floquet-Bloch dressing with 400 nm drivers supports a delocalized excitation due to dressing of the bands and thus encompassing many unit cells, the strong 800 nm driver leads to subsequent spatial localization due to Wannier-Stark dressing, and emission frequencies given by the energy differences of the localized Wannier-Stark states.

6.4. Conclusion and outlook

In conclusion, we have demonstrated efficient extreme-ultraviolet two-color non-collinear high-order wave mixing in silica. Our theory based on semiconductor Bloch equations

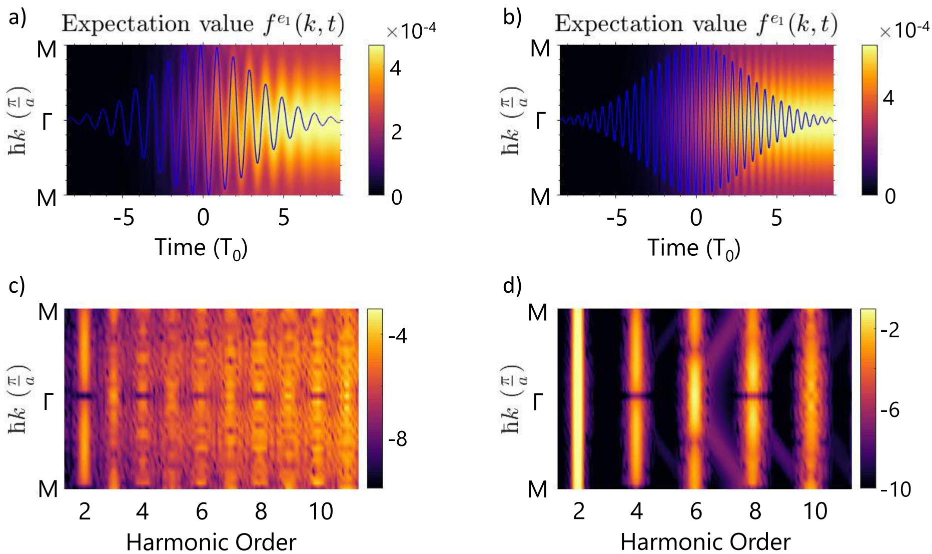

Figure 6.8: Comparison of 800-nm 400-nm driven solid-state high-harmonic generation. a) Electrons in the first conduction band as a function of time and crystal momentum for an 800-nm pulse (vector potential represented by the blue line), and b) for a 400-nm pulse. c) Energy- and momentum-resolved polarization for 800 nm, and d) for 400 nm, both for an intensity of 1.6 TW/cm^2. The color bar represents harmonic yield on a logarithmic scale. Harmonic orders refer to multiples of the 800-nm fundamental, even orders of the driving frequencies cancel out in the emission spectrum due to symmetry.

revealed that both Floquet-Bloch dressing followed by interband and intraband dynamics, that can rather be rationalized as dressed Wannier-Stark states, compete during intense laser-irradiation promoting high-efficiency carrier excitation and thus boosting the HHG emission intensity. The resulting brightness enhancement turns solid HHG into a competitive source, especially in combination with the recently pioneered wavefront shaping of solid HHG through nanostructures [191]. Moreover, our simulations show that harmonics can be understood as signatures of laser dressing and Floquet engineering of materials [199, 200], a topic that has recently gathered much attention due to the opportunity to modify electronic structures of solids at will purely through light-matter interaction [201, 202]. In addition, the multiband dynamics that drive wave mixing in this study correspond to a field-driven attosecond electron wave packet motion in the crystal lattice. The simultaneous recording of multiple experimental observables from solid HHG may thus allow for the reconstruction of this attosecond electron motion as previously achieved in molecules [128], and become a valuable tool for investigating laser-driven phase transitions and strongly correlated electron dynamics trough high-harmonic spectroscopy [203], with the possibility to add picometer spatial resolution as demonstrated for solid HHG recently [204].

7

Transient High-Harmonic Spectroscopy in MgO

7.1. Introduction

The experimental discovery of high-harmonic generation (HHG) from solids [36] has provided a new way to study strong-field light-matter interaction at timescales, spatial dimensions, and intensities that before were inaccessible. Solid HHG enables the generation of THz [37] to extreme-ultraviolet [40] wavelengths, with structured wavefronts [50, 191] through generation from nanostructured solids [51–53, 176, 191], and is demonstrated in a wide variety of materials, such as ZnO [36, 42], SiO_2 [40, 70, 171], MgO [43], and Al_2O_3 [71]. Moreover, solid HHG was demonstrated as a spectroscopy technique to probe directly the strong-field light induced electron dynamics [41, 57], electronic band structure [39, 40, 54], and valence electrons characteristics [204]. However, further developments of solid-HHG-based spectroscopy techniques are slowed down by the inherently low conversion efficiency of the process [40, 188]. To compensate for the low signal-to-noise, the repetition rate of the driving laser could be increased [59, 188, 205] to boost the HHG photon flux. Additionally, HHG at MHz/GHz repetition rates can be realized in enhancement cavities, which has been demonstrated successfully for the generation of high harmonics from gases in an intracavity configuration [206, 207]. However, in gas HHG the generation medium becomes ionized, which eventually leads to a plasma buildup in the interaction region and reduces the conversion efficiency of HHG due to phase mismatch. The highest repetition rate is therefore limited to the time it takes for the gas within the interaction volume to be refreshed. The situation in solid HHG is different, since the medium is not ionized, but merely excited with a carrier population that may relax back to the ground state on ultrafast timescales, depending on the generation medium and excitation conditions. Therefore, the effect of the excited carrier population on the solid HHG process has to be identified and understood, in order to ensure that accumulated electronic changes upon exposure do not irreversibly damage the solid and decrease the HHG efficiency between subsequent laser pulses.

Pump-probe experiments in ZnO [187] have shown that excitation of the sample decreases the overall HHG efficiency. The given explanation states that the valence band electron population depletes and reduces the interband recombination probability, resulting in less efficient HHG. However, the increased conduction band population was also shown to enhance the intraband current [187], in agreement with earlier work [208]. Additionally, pump-probe experiments in monolayer MoS_2 [209] demonstrate a reduction in the HHG efficiency, due to a decrease in coherence time of the electron-hole pairs, necessary for an interband polarization and hence HHG. The relative importance of interband and intraband electron dynamics in the process of HHG is strongly dependent on driving wavelength, intensity, and the material under investigation. Therefore, different generation conditions are expected to result in different responses of HHG in the presence of an excited carrier population. Moreover, in a quantum mechanical framework, the excitation of a material with a pump-pulse can generate a superposition state of a ground state and an excited state. Subsequent HHG from the excited material with a probe-pulse is sensitive to the emission of the superposition state, but is not able to disentangle the phase and amplitude contributions of the ground and excited state. Phase and amplitude information of HHG from an excited state can be extracted using transient grating high-harmonic spectroscopy [135, 210–212], as demonstrated for gas and molecular HHG.

Here we transpose the technique of transient high-harmonic spectroscopy to solid materials, to identify phase and amplitude of solid HHG in the presence of an excited carrier population. The high density of solids complicates this technique, since macroscopic propagation effects on the fundamental driver cannot be neglected and will affect the phase and amplitude of the HHG. Therefore, we additionally measure the effect of an excited carrier population on the fundamental wavefront, to isolate the macroscopic contributions. The remaining phase and amplitude contributions originate from the microscopic HHG process itself. We elaborate on both the macroscopic and microscopic contributions through simulations and additional measurements. In addition, we compare results of the technique performed in SiO_2 and discuss the differences. Overall we demonstrate that the combined measurement of transient grating spectroscopy on the HHG and on the fundamental allows to extract absolute phase and amplitude information of excited state HHG. Extracting both amplitudes and phases will allow for measuring transient modifications of the solids, such as band gap renormalizations and lattice expansions, and possibly even transient band structures [55] by linking the observed quantities to a theoretical model.

7.2. Experimental details

The concept of transient-grating high-harmonic spectroscopy is shown in Fig. 7.1. The setup is used to study the effect of an excited carrier population on HHG and to simultaneously compare to the properties of HHG in an unexcited configuration. To obtain an excited carrier population, we cross-illuminate the solid sample (MgO) by two 266-nm pulses. The interference of the two pulses results in a transient grating and creates

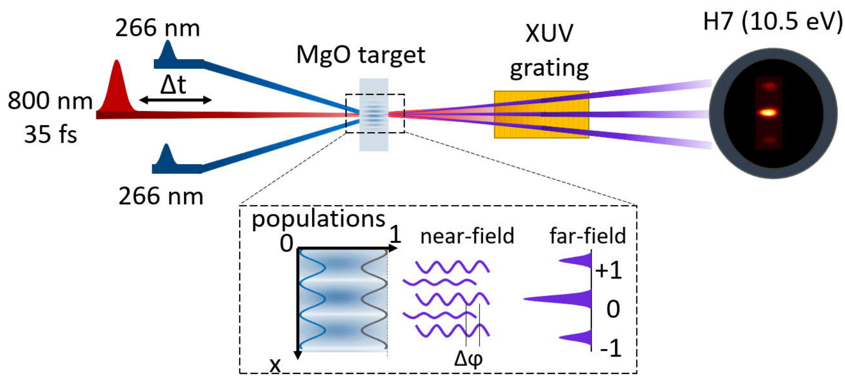

Figure 7.1: Experimental concept for transient-grating high-harmonic spectroscopy.

regions across the sample with and without an excited carrier population due to two-photon absorption. A time-delayed 800-nm pulse interacts with both regions and generates harmonics (dominated by H7), which are dispersed by an XUV grating and detected by a double-stack multi-channel plate (MCP) assembly backed with a phosphor screen. The excited carrier population influences the phase and the amplitude of the harmonic generation at the sample plane (near-field). The modulation at the sample plane is translated into a diffraction pattern in the far-field, resulting in the appearance of the first diffraction orders of each detected harmonic.

The phase and amplitude modulation of the harmonic near-field is a combination of contributions from the microscopic generation process and the macroscopic propagation. Since the attenuation lengths of H7 and H9 are about 33 nm and 20 nm for SiO_2 [117] and about 10 nm and 8 nm for MgO [118], respectively, we only take into account how the propagation modulates the fundamental driving wavefront. Subsequently, we determine this modulation by measuring the diffraction from the 800-nm fundamental from the transient grating, and determine how this is translated onto the harmonics. The total phase and amplitude modulation is retrieved through analysis of the diffracted harmonics. The experimental configuration and details of transient grating spectroscopy are described in the following section.

Transient grating spectroscopy on HHG

In more detail, the optical setup to perform transient-grating high-harmonic spectroscopy is shown in Fig. 7.2. The output of a Ti:sapphire amplifier (Coherent Astrella, 800 nm, 1 kHz, 35 fs) is split into two arms by a beamsplitter (BS). The first 800-nm arm (reflected by the BS) is used to generate the high harmonics and serves as the probe beam in this configuration. The 800-nm pulses are guided across a delay stage, to allow for control over the temporal delay between the 800-nm pulses and the transient grating. The second 800-nm arm (transmitted by the BS) is used to generate the transient grating in the sample. First, the 800-nm beam is partially converted into a second harmonic (SH, 400 nm), by frequency doubling inside a 200 μm thick β-barium borate (BBO) crystal, which is cut at an angle of 29.9 degrees. Subsequently, a calcite plate is used to compensate for the accumulated group delay between the 800-nm and 400-nm pulses. Next, a half-wave plate ($\lambda/2$) for 800 nm is used, to rotate the polarization of the 800-nm pulses such that they are aligned with the polarization of the 400-nm pulses. A second 100 μm β-BBO crystal, cut at an angle of 44.3 degrees, is used to convert the 800-nm and 400-nm pulses into 266-nm pulses, equivalent to the third harmonic (TH) of 800 nm. Two 266-nm high reflector mirrors guide the beam towards a beamsplitter, which produces two 266-nm arms. The first 266-nm arm (transmitted through the BS) is guided across a delay stage, and at the same time is lowered by about 1.5 cm in the vertical direction, hence we refer to this arm as the 'bottom' arm. The second 266-nm arm (reflected by the BS) is maintained at the same height and we refer to this arm as the 'top' arm. The vertically offset 266-nm arms are reflected to two D-shaped mirrors, which are placed alongside the beam path of the 800-nm beam. From that point on, the 266-nm beams and the 800-nm beam propagate parallel to each other. The 266-nm beams are vertically offset from the 800-nm, one 266-nm beam above and the other one below the 800-nm (this is represented in Fig. 7.2 by the horizontally displaced 266-nm arms). Next, the three beams are reflected by an DUV enhanced flat aluminum mirror onto an aluminum coated spherical mirror with a focusing distance of 75 cm, which focuses the pulses onto

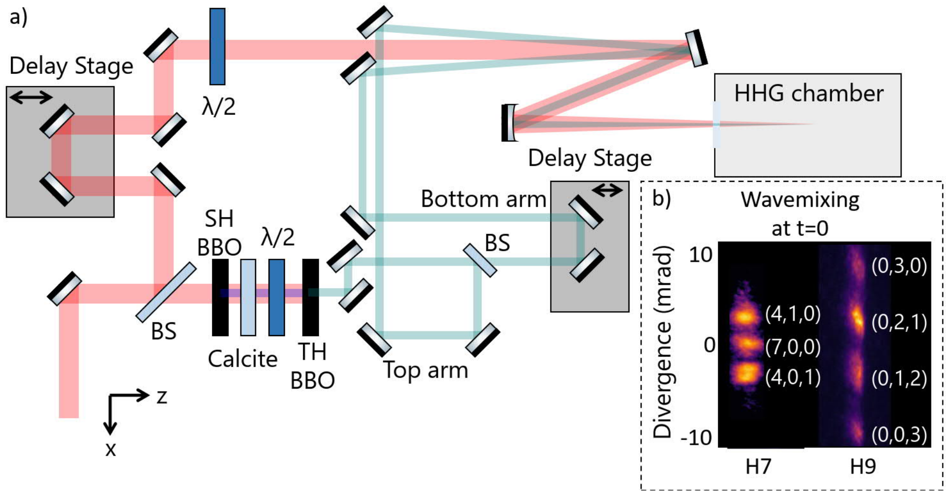

Figure 7.2: a) Experimental configuration to obtain a transient-grating for high-harmonic spectroscopy. b) Wave mixing of H7, which only appears if the 800-nm and 266-nm pulses overlap in time and space, and of H9, which is present if the 266-nm pulses overlap in time and space. The corresponding number of photons of the 800-nm pulse, the bottom 266-nm pulse, and the top 266-nm pulse are denoted in between the brackets, respectively.

the sample, located in the center of the HHG chamber. The generated harmonics (H7 and H9) are spectrally dispersed with an aberration-corrected concave flat-field grating along the horizontal direction, and freely propagate in the vertical direction. A double-stack micro-channel plate assembly, backed with a phosphor screen, detects the harmonics. Finally, a CMOS camera outside of the vacuum chamber images the phosphor screen.

To obtain a transient grating inside the sample the two 266-nm pulses require to be overlapped in time and space, which can be confirmed by the observation of wavemixing in H9, shown in Fig. 7.2b. Each 266-nm pulse will generate a third harmonic (which adds up to H9 of 800 nm) in the sample, visible at ± 9 mrad. If the two 266-nm pulses overlap in time and space, additionally the wavemixing signal between the two pulses appears at ± 3 mrad. The wavemixing orders are a combination of two photons of one 266-pulse and one photon of the other 266-pulse, which will add up to a total energy consistent with H9 of 800 nm. The ninth harmonic order, generated by the fundamental 800-nm pulses only, is very low in signal and is therefore not visible in Fig. 7.2b at 0 mrad. By maximizing the yield of the wavemixing signal, the overlap of both 266-nm pulses can be optimized. In addition, the 800-nm pulse needs to keep spatial overlap with the transient grating. In this experiment, we have stabilized one of the mirrors in the 800-nm beam path, with a feedback loop using input from the spatial position of the focus of the 800-nm arm. The signal for the feedback loop was obtained by placing a 150 μm quartz plate just before the input window, to reflect out the focus of the 800 nm. If the 800-nm pulse and two 266-nm pulses overlap in time, wavemixing in H7 is observed, see Fig. 7.2b. The wavemixing signal originates from the addition of one 266-nm photon from one beam and four 800-nm photons, adding up to H7, and appears at ± 3 mrad. In addition, a wavemixing signal appears at 0 mrad from the addition of one 266-nm photon of each arm and one 800-nm photon, which therefore overlaps with the signal of H7 generated by 800 nm only. The yield of the wavemixing signal will depend on the relative intensity of the 800-nm and the 266-nm pulses, as will be discussed later on in this chapter. If the 800-nm and 266-nm pulses have optimal overlap in time and space, the yield of the wavemixing signal will be optimized, and can therefore be used as an alignment tool.

Transient grating spectroscopy on the fundamental wavefront

To identify the effect of the transient grating on the fundamental wavefront, we reflect the recombined pump and probe pulses with an additional DUV enhanced aluminum mirror, placed just before the input window, onto an MgO sample outside of the vacuum chamber, as shown in Fig. 7.3a. The sample is positioned in the focus of the 266-nm and 800-nm pulses. A filter to remove the 266-nm pump pulses is placed in the propagation path, such that the isolated 800-nm wavefront can be measured with a camera. The temporal and spatial overlap of the 266-nm pulses can be confirmed by the observation of self-diffraction (SD) [213] of the 266-nm pulses, as shown in Fig. 7.3b. If the 266-nm pulses overlap in time and space, they will induce a transient grating. Subsequently each 266-nm pulse can diffract from this transient grating itself, resulting in two additional 266-nm beams, vertically offset to the zeroth order of the 266-nm beams. The intensity of the 266-nm pulses is high enough to locally modify the material properties of the sample. If the delayed 800-nm pulse overlaps with this locally modified region, small intensity modifications to the 800-nm wavefront can be observed, as visible in the difference in signal distribution in the zeroth order, before and after time zero, in the bottom panels of Fig. 7.3c. The observation of these small modifications can be used to ensure spatial overlap. Next, the effect of the transient grating on the fundamental

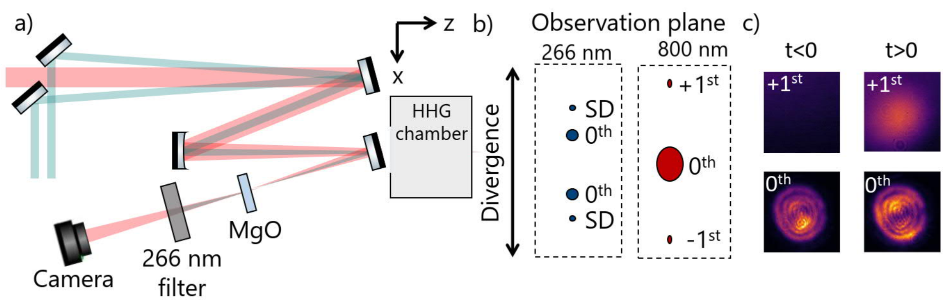

Figure 7.3: a) Experimental configuration to measure the effect of the transient-grating on the fundamental wavefront. b) Observation of self-diffraction (SD) of 266-nm ensures overlap between the two 266-nm pulses. Subsequently the fundamental field is diffracted. c) Measured first and zeroth order diffraction of the fundamental, before and after time zero.

wavefront can be identified. In the case of MgO, the transient grating results in a refractive index modulation, which translates into a phase modulation onto the fundamental wavefront. As a result, diffraction of the fundamental beam can be observed, as shown in Fig. 7.3b. The yield of both the zeroth diffraction order and the first diffraction order are measured with a camera for a range of time delays. Before time zero, no diffraction is present. After time zero, the first diffraction order appears, and additionally the zeroth order wavefront shows modulations (Fig. 7.3c). For visualization the first order signal is multiplied by 100, in order to compare with the zeroth order signal. The diffraction angle of the first orders depends on the parameters of the transient grating, described in the next section.

7.3. Theoretical background

This section describes the underlying theoretical background of the transient grating. In addition, the extraction of the relative phase and amplitude from the experimental data is presented.

Transient grating parameters

The transient grating [214] is formed by the interference between two crossing beams, as shown in Fig. 7.4a. The interference leads to a spatially modulated distribution of the 266-nm intensity, which results in an excited carrier population through two-photon absorption. To obtain the intensity distribution of 266-nm at the sample plane, we will first determine the total electric field. We formulate the electric fields polarized along the $\hat{z}$-direction as,

$$E_1(\mathbf{r},t) = E_1 e^{i(\mathbf{k}_1\cdot\mathbf{r}-\omega t+\phi_1)}\hat{\mathbf{z}} \tag{7.1}$$

$$E_2(\mathbf{r},t) = E_2 e^{i(\mathbf{k}_2\cdot\mathbf{r}-\omega t+\phi_2)}\hat{\mathbf{z}} \tag{7.2}$$

where E_1 and E_2 are the amplitudes of the fields and the phase of the fields is determined by the three contributions in the exponential. The first term is set by $\mathbf{k}_1$ and $\mathbf{k}_2$, which represent the wave vectors, and the propagated distance $\mathbf{r}$. The second term is set by the central frequency ω of the beam. The last term represents a general phase offset ϕ_1 and ϕ_2, for each beam respectively, which we set to zero for simplicity further on. In the experimental configuration the two beams have the same wavelength and cross each with an angle θ with respect to the propagation plane. Based on the symmetry in the x direction and the asymmetry in the y direction, we can write out the wave vectors of each wave as: $\mathbf{k}_1 = (k_{1,x}, k_{1,y})$ and $\mathbf{k}_2 = (k_{2,x}, k_{2,y}) = (k_{1,x}, -k_{1,y})$. The electric fields can therefore be written as,

$$E_1(x,y,t) = E_1 e^{i(k_{1,x}x+k_{1,y}y-\omega t)}\hat{\mathbf{z}}, \tag{7.3}$$

$$E_2(x,y,t) = E_2 e^{i(k_{1,x}x-k_{1,y}y-\omega t)}\hat{\mathbf{z}}. \tag{7.4}$$

We assume the same field amplitude $E_1 = E_2 = E_i$ for both waves, and obtain an expression for the total field by adding up both contributions,

$$E_{\text{total}}(x,y,t) = 2E_i\cos(k_{1,y}y)e^{i(k_{1,x}x-\omega t)}\hat{\mathbf{z}}. \tag{7.5}$$

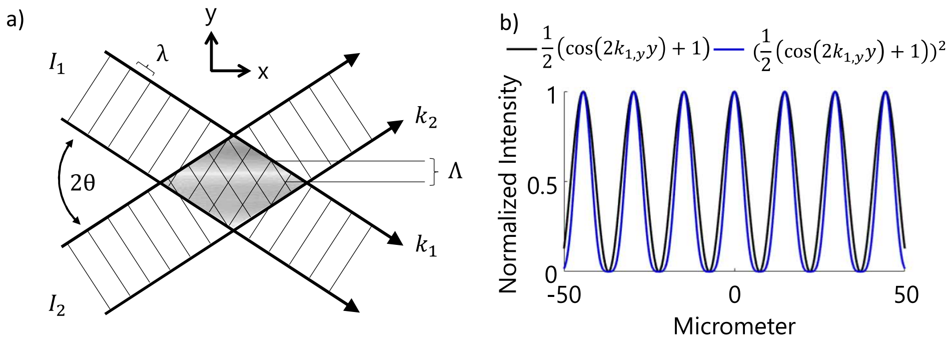

Figure 7.4: a) Two crossing beams leading to a transient-grating. b) Intensity distribution at the sample plane (black line). The excited carrier population, induced by two-photon absorption, is described by the distribution given by the blue line.

The amplitude of the total field is spatially modulated along the y-direction, $E_0 = 2E_i\cos(k_{1,y}y)$. The resulting total intensity distribution is defined as,

$$I \propto |E_0|^2 \propto |2E_i|^2 \cos^2(k_{1,y}y) \propto 4|E_i|^2 \left(\frac{1+\cos(2k_{1,y}y)}{2}\right). \tag{7.6}$$

The wave vector $k_{1,y} = \sin(\theta)\frac{2\pi}{\lambda}$ is set by the crossing angle θ and the wavelength λ. The resulting periodicity of the spatial modulation equals $\Lambda = \frac{\lambda}{2\sin(\theta)}$. As an example, if the crossing angle equals 9 mrad, the resulting intensity modulation (black line) induced by the transient grating has a 14.8 µm pitch, which is depicted in Fig. 7.4b. The focus sizes of the beams in our experiment are around 150 µm, such that the fundamental is exposed to multiple periods of the grating and thus diffracts. The excitation of an electron across the bandgap of MgO (7.8 eV) can only occur through two-photon absorption. Effectively the distribution of the excited carrier population (blue line) equals I^2, such that the spatial modulation is described by $\left(\frac{1+\cos(2k_{1,y}y)}{2}\right)^2$, see Fig. 7.4b.

Relative phase and relative amplitude

The observed diffraction of the generated harmonic is caused by a phase and amplitude modulation of the harmonic field at the sample plane, induced by the transient grating. This section describes how to reconstruct the relative phase and amplitude using the diffraction signals of the generated harmonics. The illumination of the sample with a transient grating results in regions with an excited carrier population (excited state) and regions that remain unexcited (ground state). We define the transient amplitude and phase of the ground state emission as d_g and ϕ_g and for the excited state as d_e and ϕ_e. Also we introduce the relative amplitude $d_r = \frac{d_e}{d_g}$ and the relative phase as $\Delta\phi = \phi_e - \phi_g$. The total harmonic intensity, as a function of time, from the ground state and the excited state is given by:

$$\begin{aligned} I_{\text{total}}(t) &= |E_g + E_e|^2 \\ &= |d_g \mathrm{e}^{i\phi_g} + d_e \mathrm{e}^{i\phi_e}|^2 \\ &= d_g^2 + d_e^2 + d_g d_e (\mathrm{e}^{i\phi_g - i\phi_e} + \mathrm{e}^{-i\phi_g + i\phi_e}) \\ &= d_g^2 + d_e^2 + 2 d_g d_e \cos(\Delta\phi) \\ &= d_g^2 (1 + d_r^2 + 2 d_r \cos(\Delta\phi)) \end{aligned} \tag{7.7}$$

The intensity of the unexcited sample is equal to d_g^2. If we normalize the total signal to the ground state intensity, we obtain the following expression:

$$\frac{I_{\text{total}}}{I_0}(t) = 1 + d_r^2 + 2 d_r \cos(\Delta\phi) \tag{7.8}$$

As elaborated on in the previous section, due to the two-photon excitation, we obtain a spatially modulated distribution of an excited-state population that is proportional to the function $(\frac{1}{2}(\cos(kx)+1))^2$, with the wave vector $k = 2k_{1,y}$. The excited fraction is normalized to the maximum induced carrier population, and therefore oscillates between 0 and 1. We are using the expression $\cos^2(x) = \frac{1+\cos(2x)}{2}$ to rewrite the spatial distributions of the ground state and the excited state to

$$\begin{aligned} E_g(x) &= d_g \mathrm{e}^{i\phi_g} \left(1 - \frac{1}{4}(\cos(kx)+1)^2\right) \\ &= d_g \mathrm{e}^{i\phi_g} \left(\frac{5}{8} - \frac{1}{2}\cos(kx) - \frac{1}{8}\cos(2kx)\right) \end{aligned} \tag{7.9}$$

$$\begin{aligned} E_e(x) &= d_c \mathrm{e}^{i\phi_c} \left(\frac{1}{4}(\cos(kx)+1)^2\right) \\ &= d_c \mathrm{e}^{i\phi_c} \left(\frac{3}{8} + \frac{1}{2}\cos(kx) + \frac{1}{8}\cos(2kx)\right) \end{aligned} \tag{7.10}$$

The modulation of the ground state and the excited state will result in a diffraction pattern of the harmonic signal in the far-field, which oscillates with spatial frequency ξ, and is determined by a Fourier transform. We add up the two signals and obtain the following expression for the far-field distribution,

$$\begin{aligned} \mathscr{F}(E_g + E_e)(\xi) = &\left(d_g \mathrm{e}^{i\phi_g}\frac{5}{8} + d_e \mathrm{e}^{i\phi_e}\frac{3}{8}\right)\delta(\xi) + \\ &\frac{1}{4}\left(d_e \mathrm{e}^{i\phi_e} - d_g \mathrm{e}^{i\phi_g}\right)\left(\delta(\xi - \frac{k}{2\pi}) + \delta(\xi + \frac{k}{2\pi})\right) + \\ &\frac{1}{16}\left(d_e \mathrm{e}^{i\phi_e} - d_g \mathrm{e}^{i\phi_g}\right)\left(\delta(\xi - \frac{k}{\pi}) + \delta(\xi + \frac{k}{\pi})\right) \end{aligned} \tag{7.11}$$

The intensity of the zeroth diffraction order is given by,

$$\begin{aligned} I_{m=0}(t) &= \left|\left(d_g \mathrm{e}^{i\phi_g}\frac{5}{8} + d_e \mathrm{e}^{i\phi_e}\frac{3}{8}\right)\right|^2 \\ &= \frac{d_g^2}{16}\left(\frac{9}{4} + \frac{25 d_r^2}{4} + \frac{30}{4} d_r \cos(\Delta\phi)\right) \end{aligned} \tag{7.12}$$

The intensity of the first diffraction order is given by,

$$\begin{aligned} I_{m=1}(t) &= \left|\frac{1}{4}\left(d_e \mathrm{e}^{i\phi_e} - d_g \mathrm{e}^{i\phi_g}\right)\right|^2, \\ &= \frac{d_g^2}{16}\left(d_r^2 - 2 d_r \cos(\Delta\phi) + 1\right). \end{aligned} \tag{7.13}$$

Due to the two-photon absorption and the resulting spatial distribution, second order diffraction will also appear in the far-field. The second order will be absent in the case of a one-photon absorption process [135]. The intensity of the second order diffraction peak is given by,

$$\begin{aligned} I_{m=2}(t) &= \left|\frac{1}{16}\left(d_e \mathrm{e}^{i\phi_e} - d_g \mathrm{e}^{i\phi_g}\right)\right|^2, \\ &= \frac{d_g^2}{16^2}\left(d_r^2 - 2 d_r \cos(\Delta\phi) + 1\right). \end{aligned} \tag{7.14}$$

Using the expression for the zeroth (Eq. 7.12) and first order diffraction (Eq. 7.13), we can solve for the product of the relative amplitude and phase,

$$d_r \cos(\Delta\phi) = \frac{16(I_{m=0} - \frac{25}{4} I_{m=1}) + 4}{20}. \tag{7.15}$$

In addition we can solve for the square of the relative amplitude, by substitution of Eq. 7.12 into Eq. 7.15,

$$d_r^2 = 16 I_{m=1} + 2 d_r \cos(\Delta\phi) - 1. \tag{7.16}$$

The product of the relative amplitude and phase (Eq. 7.15) can be calculated using the measured intensity of the zeroth order ($I_{m=0}$) and the first order ($I_{m=1}$) diffraction. Subsequently, the retrieved value of Eq. 7.15 can be substituted into Eq. 7.16 to solve for the square of the relative amplitude d_r^2. Knowing d_r^2 and $d_r \cos(\Delta\phi)$, we can determine the relative amplitude d_r and relative phase $\Delta\phi$.

The relative amplitude and phase relate to the properties of the harmonic field at the generation plane. The phase and amplitude of the harmonic field, described for harmonic order q, are proportional to the properties of the 800-nm field that generates the harmonic radiation at the ground state and excited state region,

$$
\begin{aligned}
E_{g,q} &= d_{g,q}\mathrm{e}^{i\phi_{g,q}} \propto (E_{g,800})^q = (d_{g,800})^q \mathrm{e}^{iq\phi_{g,800}},\\
E_{e,q} &= d_{e,q}\mathrm{e}^{i\phi_{e,q}} \propto (E_{e,800})^q = (d_{e,800})^q \mathrm{e}^{iq\phi_{e,800}}.
\end{aligned}
\tag{7.17}
$$

More specifically, the amplitude and the phase of the 800-nm field for both the ground state and the excited state region have to be determined. Due to the two-photon excitation, the material properties of the excited region may change compared to the unexcited ground state region, which could influence the phase and amplitude of the fundamental field during the propagation through the MgO sample. In particular, a refractive index modulation induces a phase modulation onto the fundamental wavefront, which additionally modifies the amplitude distribution of the fundamental wavefront, as will be elaborated on later in this Chapter. The exact dependence of the harmonic amplitude on the fundamental field strength is not known, therefore we make a perturbative approximation, such that the harmonic amplitude is raised to the power of the harmonic order q. Additionally, the phase of the fundamental field that is transferred to the harmonic order is also proportional to q. In addition to the fundamental field properties, an additional amplitude and phase component contribute to the harmonic field, induced by the HHG process itself. For example, the presence of an excited carrier population could modify the efficiency of the HHG process and introduce an associated extra phase contribution. We refer to this amplitude for the ground and excited state HHG process as, $d_{g,\mathrm{HHG}}$ and $d_{e,\mathrm{HHG}}$, respectively. The phases induced by the HHG process are defined as $\phi_{g,\mathrm{HHG}}$ and $\phi_{e,\mathrm{HHG}}$, for the ground state and the excited state respectively. The total harmonic near field of the ground and excited state region can therefore be described as,

$$
\begin{aligned}
E_{g,q} &= (d_{g,800})^q d_{g,\mathrm{HHG}}\mathrm{e}^{iq\phi_{g,800}+i\phi_{g,\mathrm{HHG}}},\\
E_{e,q} &= (d_{e,800})^q d_{e,\mathrm{HHG}}\mathrm{e}^{iq\phi_{e,800}+i\phi_{e,\mathrm{HHG}}}.
\end{aligned}
\tag{7.18}
$$

Finally, we define the relative amplitude and relative phase of the harmonic field at the generation plane by dividing $E_{e,q}$ with $E_{g,q}$,

$$
\frac{E_{e,q}}{E_{g,q}} = E_{r,q} = d_{r,q}\mathrm{e}^{i\Delta\phi_q}
\tag{7.19}
$$

After substitution of Eq. 7.18 into the expression of Eq. 7.19, we find the final expressions for the relative phase and relative amplitude of the harmonic field,

$$
\begin{aligned}
\Delta\phi_q &= q\Delta\phi_{800} + \Delta\phi_{\mathrm{HHG}},\\
d_{r,q} &= (d_{r,800})^q d_{r,\mathrm{HHG}}.
\end{aligned}
\tag{7.20}
$$

In more detail, the total relative phase $\Delta\phi_q$ is given by the combination of the macroscopic phase from the fundamental field $\Delta\phi_{800}$ multiplied by the harmonic order q, and from the phase that originates from the microscopic HHG process, $\Delta\phi_{\mathrm{HHG}}$. For the total relative amplitude d_r, both the amplitude of the generation process and the properties of the fundamental field have to be taken into account. Since the exact dependence of the harmonic amplitude on the fundamental field is not known, the expression for the relative amplitude $d_{r,q}$ is an approximation. In contrast to the approximated amplitude, the phase expression is exact.

7.4. Results

7.4.1. Transient grating spectroscopy of harmonic 7 in MgO

The generation of harmonics in MgO using 800-nm pulses is dominated by the emission of H7 (10.8 eV). In the presence of the transient grating (TG), induced by 266-nm pulses with a total intensity of 2 10^{11}W/cm^2, an excited carrier population modulates the H7 near-field and TG diffraction orders appear in the far-field. The signal of the diffracted harmonic is determined as a function of the time delay between the 800-nm pulse and the TG, as shown in Fig. 7.5a. The intensity of each diffraction order is normalized to the total signal of H7 at negative time delays, which corresponds to 800-nm pulses arriving at the sample before excitation. The intensity can therefore be compared directly to an unexcited (ground state) configuration. Remarkably, the total intensity of harmonic 7 (black line) is higher in the presence of an excited carrier population. The zeroth order diffraction first shows a decrease in signal and slowly recovers back to unity for larger time delays. The diffraction signals decay exponentially, with a mean decay time of 73 ps (± 3 ps), indicating that the excited carrier population decays on the same timescale. The decay time is on the same order of magnitude compared to earlier findings of a free-carrier population in MgO [215], which reports a mean decay time of 50 ps (± 5 ps).

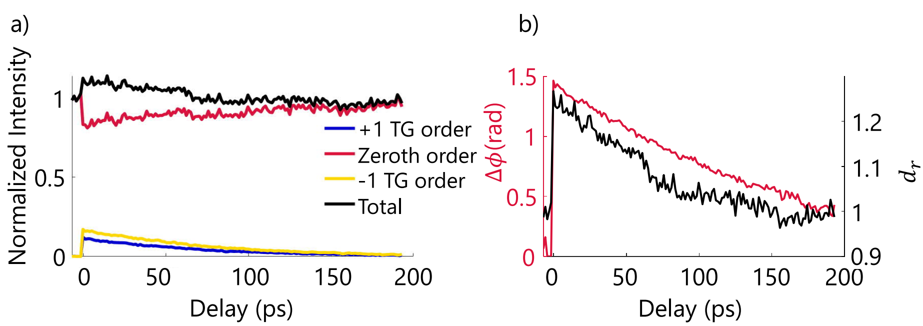

Figure 7.5: a) Zeroth order (red) and transient grating (blue and yellow) diffraction orders of H7 in MgO. The total signal is denoted by the black line. b) Reconstructed relative phase and amplitude.

As described in the theoretical background, we can retrieve the relative phase and amplitude of the harmonic field at the sample plane using the intensity of the zeroth and the first TG diffraction orders, which is depicted in Fig. 7.5b. The relative phase peaks at about 1.5 radian just after time zero, and decays over time as the excited carrier population relaxes. The relative amplitude shows a similar trend, starting at a peak value of 1.25. The relative amplitude is defined as the ratio between the excited state and the ground state amplitude, therefore we can conclude that the harmonic intensity (d_r^2) of the excited region is more than 50% higher. Before the excitation, the relative phase difference and relative amplitude are zero and one, respectively, as the entire sample is unexcited and can be described by the ground state. At the moment the carrier population has fully relaxed back to equilibrium, we expect to get back to the values before time zero. Indeed, the relative amplitude decays back to unity. However, the relative phase shows an offset of 0.5 radian. Since the total signal at large delays has not fully recovered back to the initial signal level and there is still some signal present in the ± first TG orders, a non-zero relative phase is reconstructed.

These results indicate that if the excited carrier population increases, the diffraction efficiency and the total signal also increase. We confirm this observation with another measurement, shown in Fig. 7.6a, where we determine the dependence of the diffraction signals on the 266-nm intensity. The time delay between the 800-nm probe pulse and the transient grating is set at 3 ps. Next, the 266-nm intensity is increased in steps, which results in an growing excited carrier population. We observe that a higher 266-nm intensity will lead to a higher diffraction efficiency and that the total signal is also enhanced. The reconstructed relative phase and amplitude of the diffracted signals as a function of 266-nm intensity is presented in Fig. 7.6b. As expected, for low 266-nm intensity (little excitation), there is little difference between the ground state and the excited state, such that the relative phase and amplitude equal zero and one, respectively. As the 266-nm intensity increases, the excited carrier population grows, and the relative

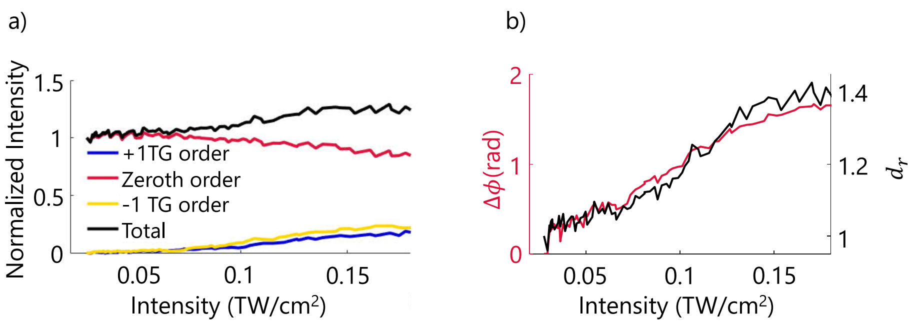

Figure 7.6: a) Zeroth order (red) and transient grating (blue and yellow) diffraction orders of H7 in MgO, as a function of 266-nm intensity. The total signal is denoted by the black line. b) Reconstructed relative phase and amplitude.

phase and amplitude also increase. This observation can be explained by two reasons. On the one hand, the excited carrier population will induce refractive index changes, which can modify properties of the fundamental wavefront due to propagation effects. These properties will be transferred to the harmonic generation. On the other hand, the presence of an excited carrier population changes the generation conditions of the HHG process, and results in modified generation efficiency with corresponding phase modifications. Since both processes are influenced by the excited carrier population, we now perform independent measurements on the transient diffraction of the fundamental 800-nm pulses in order to decouple the different contributions from each other.

7.4.2. Macroscopic propagation contributions

To identify the contribution to the relative phase and amplitude due to propagation effects, we need to determine the phase and amplitude of the fundamental wavefront at the generation plane, in the presence of a transient grating. In order to do so, we generate a transient grating in MgO and measure the diffraction of the fundamental 800-nm wavefront, as described in Fig. 7.3. The decay time of the excited carrier population in Fig. 7.5a corresponds to the decay times of a free-carrier population, which induces a refractive index change [8, 215], defined in SI units as,

$$\Delta n = -\frac{\Delta N_c e^2}{\epsilon_0 m \omega^2}, \tag{7.21}$$

with ΔN_c the carrier population in the conduction band, e the electronic charge, ϵ_0 the vacuum permittivity, m the effective electron mass, and ω the angular frequency of the excitation pulse. The induced refractive index change translates into a phase modulation imprinted onto the fundamental wavefront, upon propagation through the MgO sample. The accumulated phase in the near-field results in diffraction of the fundamental wavefront in the far-field. The zeroth and first order diffraction were measured as a function of time delay, as shown in Fig. 7.7a. The intensity of the 266-nm pulses in this experiment is estimated at 2.3 10^{11}W/cm^2, which is different from the transient grating used in Fig. 7.5a. Therefore we abstain from comparing absolute values, and focus on comparing qualitative trends. As expected, no diffraction appears for negative time delays, at which no excited carrier population is present. After time zero, the zeroth order shows a small dip in signal and we see the first diffraction order appear, which is multiplied by a factor of 100 for visualization. The diffraction into the first orders cannot account for the total observed decrease in the zeroth order signal, which therefore might be caused by induced nonlinear absorption of the fundamental due to the presence of the excited carriers. The first order diffraction signals show an exponential decay with a mean decay time of 34 ps ± 4 ps. The peak diffraction efficiency into the first order (just after 0 time delay) is calculated to be 2.7 10^{-3}. The diffraction efficiency from a near-field phase modulation, induced by two-photon absorption and corresponding transient grating parameters, is calculated using rigorous coupled wave analysis (RCWA) simulations. The measured diffraction efficiency corresponds to a refractive index modulation of -2.7 10^{-4}, which leads to an accumulated negative phase of -0.21 rad due to propagation through the 100 μm MgO sample, calculated using the relation $\Delta\phi = \frac{\Delta n x}{\lambda}$, where x corresponds to the thickness of the sample.

Earlier work on structured solid HHG, presented in Chapter 6, has shown that a phase modulation imprinted onto the fundamental wavefront results in an additional amplitude modulation [191]. In accordance to those findings, we calculate the phase and amplitude of the fundamental after propagation through the sample using Fresnel diffraction. As a first assumption, we assume all accumulated phase, as calculated by the RCWA simulations, is imprinted on the fundamental field at the first interface, which corresponds to an upper limit estimate of the amplitude and phase modulations. The spatial phase modulation of the fundamental wavefront at the first interface follows a two-photon excitation distribution as given by Eq. 7.6, since the induced phase modulation originates from a refractive index modulation (Eq. 7.21), which is determined by the excited carrier population. Subsequent propagation through the sample, reveals that indeed an additional amplitude modulation is present in the 800-nm near-field at the sample exit surface. The amplitude and phase modulations are shown in Fig. 7.7b. In more detail, the spatial distribution of the phase modulation preserves it shape, although the relative phase reduces slightly in magnitude from -0.21 rad to about -0.17 rad. The amplitude modulation is visible on top of the Gaussian envelope of the 800-nm wavefront.

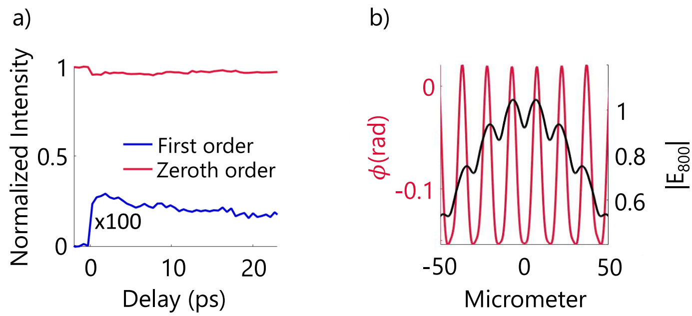

Figure 7.7: a) Zeroth and first diffraction orders of fundamental wavefront from a carrier population induced phase grating. b) Propagated near-field of 800-nm at the generation plane, showing both phase and amplitude modulation.

In Figure 7.8 we compare the phase and amplitude modulation that is contributed to the XUV by the spatially modulated fundamental with the experimentally reconstructed total relative phase and amplitude in the XUV presented in Fig. 7.6. Since the intensity of the 266-nm pulses was different in the measurements, and the experiment was performed at a different time, we refrain from any absolute comparisons. Nevertheless, we will compare the trends of the relative phase and amplitude we observe. First we compare the modulation of the phase in Fig. 7.8a. The XUV phase modulation is constructed by imprinting the peak relative phase difference in Fig. 7.6b onto the spatially modulating two-photon absorption distribution, presented in Fig. 7.4b. The contribution of the fundamental to the XUV phase modulation is constructed by multiplying the spatially resolved phase modulation in Fig. 7.7b with a factor of 7, corresponding to the harmonic order. The spatial phase modulation of the XUV and the contribution of the fundamental to the XUV match in terms of periodicity and shape of the distribution, see Fig. 7.8a. However, the absolute value of the phases are noticeably different, since the XUV phase shows a stronger phase modulation than the contribution of the fundamental. The remaining offset can have two origins. Either the difference originates from the experimental conditions not being identical, or the difference originates from an additional phase modulation originating from the microscopic HHG process. Further measurements will have to be performed, to identify what causes the observed phase offset. A similar analysis is performed for the amplitude comparison, see Fig. 7.8b. The XUV amplitude is presented as the absolute value of the harmonic near field, which is constructed using the peak relative amplitude obtained from Fig. 7.5b. For visualization, the ground state amplitude is defined as one, such that the excited state amplitude corresponds to the relative amplitude. The amplitudes are then imprinted onto the spatial modulation induced by two-photon absorption, as described in Eq. 7.9 and Eq. 7.10. To obtain the contribution of the fundamental to the XUV amplitude modulation, the amplitude modulation presented in Fig. 7.7b is divided by the Gaussian envelope of the fundamental wavefront. To convert the fundamental amplitude modulation to the harmonic near-field modulation, we use a perturbative approximation and raise the amplitude distribution to the power of 7, the harmonic order. Moreover, the transferred fundamental field distribution indicates a lower amplitude at the ground state regions, compared to the initial field strength, which would correspond to 1. Therefore, we refrain from defining a relative amplitude for the contribution of the fundamental to the XUV, as the ground state region does not have the same amplitude as before excitation. We observe that the modulation due to the fundamental is on the same order of magnitude as the XUV amplitude, however the spatial trends do not match well. The near-field propagation of the fundamental wavefront does not resemble an amplitude modulation that follows a two-photon absorption distribution. Additionally, the fundamental amplitude modulation is most likely an overestimation, as it is calculated while assuming all phase modulation is imprinted on the front surface of the sample. The discrepancy of the amplitude modulation could be accounted for by the modified microscopic HHG efficiency in the presence of an excited carrier population, which will follow a two-photon excitation spatial modulation. Overall, the phase and amplitude modulations of the fun-

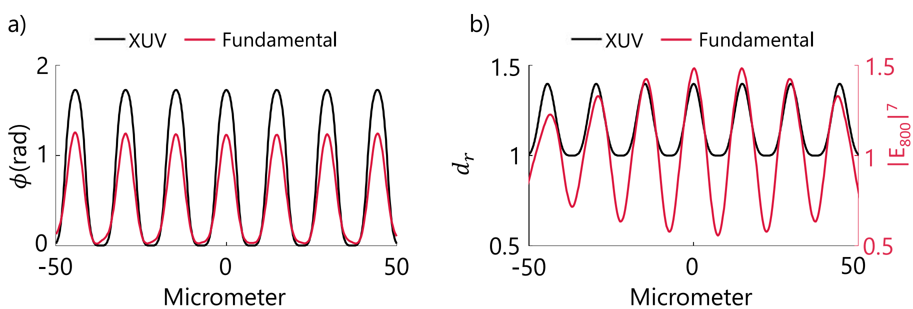

Figure 7.8: a) Comparison of the phase modulation reconstructed from the XUV measurements (as presented in Fig. 7.6) and from the contribution of the spatially modulated fundamental to the XUV (as presented in Fig. 7.7), shown as the black and red line, respectively. The phase discrepancy might be accounted for by an intrinsic phase originating from the microscopic HHG process. b) Comparison of the XUV amplitude modulation and the fundamental amplitude modulation. The XUV amplitude modulation (as reconstructed from the data in Fig. 7.6b) follows a two-photon excitation spatial modulation. A perturbative approximation is made, to approximate the effect of the fundamental field modulation (as obtained from Fig. 7.7b) onto the harmonic near-field modulation. The mismatch in amplitude modulation might again originate from the microscopic HHG process.

damental wavefront will have a contribution to the overall relative phase and amplitude of the XUV, which can not be neglected. How much the contribution is exactly, will have to be determined in future measurements, in which the transient grating has the exact same parameters in both the measurement on harmonic diffraction as the measurement on the fundamental wavefront diffraction.

7.4.3. Microscopic generation contributions

The results presented so far demonstrate that a transient grating of excited carrier population modifies the harmonic near-field, of which a fraction originates due to propagation effects of the fundamental wavefront. Although further experiments have to determine the exact fraction, we elaborate in this section on the remaining contribution to the relative phase and amplitude originating from the HHG process itself. To isolate the contributions of the fundamental propagation and the microscopic generation process, we block one of the 266-nm beams and perform a pump-probe measurement with only one excitation pulse, see Fig. 7.9. If only one 266-nm pulse illuminates the sample, we do not induce a transient grating and there will be no modulation of the fundamental wavefront due to propagation effects. Effectively, the pump-probe measurement probes only the relative phase and amplitude contribution originating from a modulated microscopic HHG process. We compare the intensity of the zeroth order diffraction of H7 for three different situations, see Fig. 7.9. Each intensity is normalized to the signal at negative time delays, corresponding to an unexcited sample. The signal of the zeroth order drops in the configuration where both 266-nm arms form a transient grating in the sample (red line, denoted by TG). In addition, the trend is shown for the pump-probe scheme (blue line), which also shows a drop compared to the unexcited trend (black line), corresponding to an 800-nm only configuration.

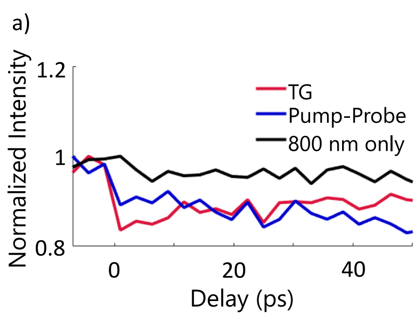

Figure 7.9: a) Intensity of the zeroth diffraction order of H7 for three different measurement configurations: both 266-nm arms are present (red line) and form a transient grating, only one 266-nm arm is present (blue line), which is a regular pump-probe measurement, and no 266-nm is present (black line) to compare with the 800-nm only trend.

The drop in signal in a pump-probe configuration suggests that the harmonic generation from an excited sample decreases the total signal, due to a combination of amplitude and phase contributions. Earlier work on transient-grating spectroscopy in molecules

[135, 210–212] explains that a drop in zeroth order diffraction in a pump-probe configuration can be caused by the destructive interference between the excited state and the ground state. In the case of molecules, the excitation from the ground state to the excited state is associated with a certain excitation probability. Effectively, only a fraction of the molecules is excited, and the generation target is described by a combination of ground state and excited state components, which possess a different phase and amplitude. A pump-probe configuration measures the interference between the excited state and the ground state, which can either be constructive or destructive, depending on the relative phase between the states. In gas-based HHG, the relative phase difference between the states can be related to the properties of the electron dynamics upon generation. In an excited state, the electron experiences a different ionization potential, which translates into a phase offset compared to the ground state excitation. Additionally, the efficiency of the HHG process is higher for the excited state due to the different ionization potential.

For solid-based HHG a similar mechanism could explain the observed drop in zeroth order diffraction. Upon illumination by a 266-nm pulse, only a fraction of the MgO unit cells obtain an excited carrier population. We perform a preliminary simulation, to investigate the effect of an excited carrier population on the efficiency of the HHG process, see Fig. 7.10. The HHG process is simulated by the interaction of an 800-nm pulse interacting with a two-level system (0 eV and 7.8 eV, representing MgO), defined in the adiabatic basis using Houston states, which is described in more detail in Chapter 2, section 3.2 of this thesis. To mimic an excited population, the initial population of the levels was altered to match the refractive index change, retrieved from the results presented in Fig. 7.7. Using Eq. 7.18, the retrieved refractive index change corresponds to a conduction band carrier population of $1.5\ 10^{19}\ e/\mathrm{cm}^3$. Based on the density of MgO ($5\ 10^{22}$ units/cm^3) and the presence of eight valence electrons per unit MgO, we calculate an excitation fraction of 0.26%. The harmonic spectra were calculated for both an excited and unexcited configuration, see Fig. 7.10. The excited configuration generates an enhanced HHG signal compared to the unexcited configuration. The already present carrier population results in an increased HHG signal, since the amplitude of both the interband polarization and intraband current depend on the carrier density within a level. Even though this simulation shows that an excited carrier population increases the yield of the HHG process compared to an unexcited sample, these results are insufficient to explain our experimental results. In particular, the simulation presented is based on a single-electron interaction, whereas in reality the interaction of many electrons with the strong-light field generates high-harmonics. Especially the effect of an excited carrier population on the decoherence time of the electron-hole pairs involved in the generation has to be identified, as this will also determine the magnitude of the interband polarization and hence the HHG efficiency. Moreover, it is not included to what extent an excited unit cell of MgO affects neighbouring unit cells, and therefore how the electronic band structure of MgO is modified by an excited carrier population. Besides the amplitude of the HHG signal, more advanced simulations should provide phase information of the HHG, for both the excited and unexcited configuration. The origin of the corresponding phase difference is possibly directly related to any changes in the band gap, equivalent to the change in ionization potential for the molecular case. To cor-

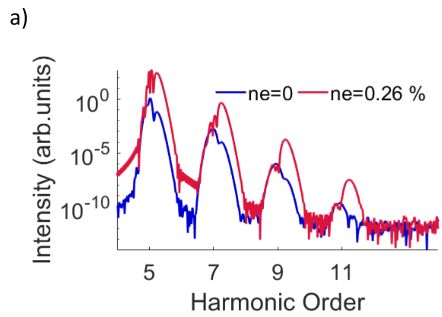

Figure 7.10: a) HHG spectrum of MgO calculated in the Bloch basis for an unexcited (blue) and excited (red) configuration, corresponding with an initial conduction band population of 0.26%.

rectly calculate the effect of an excited carrier population on the HHG process advanced simulations have to be performed. Specifically using models that take into account the modification of the electronic landscape of MgO in the presence of an excited carrier population and multi-electron interactions, such as dephasing of the carrier population.

7.4.4. Comparison with Silica

The decay dynamics of the excited carrier population in MgO show a decay time of 73 ps (± 3 ps) in Fig.7.5a, which means that a laser with GHz repetition rate could be used to drive solid HHG in MgO and to increase the photon flux. Another material which has shown to generate efficient harmonics in the XUV [40] is SiO_2, of which the free-carrier population was shown to decay on the order of 100 fs [215], and subsequently forms a self-trapped exciton population, which is hypothetically even compatible with THz repetition rate drivers. In contrast to MgO, free-carriers in SiO_2 can form trapped exciton states [215], of which the effect on HHG is not known. Therefore, the transient-grating spectroscopy was also attempted in SiO2, but no transient-grating signal was observed. Due to the larger band gap of SiO_2 (9.6 eV), excitation with 266-nm photons can only occur through three-photon absorption, which is significantly less efficient compared to two-photon absorption. The comparison between the wavemixing signals of H7 in MgO and SiO_2 in Fig. 7.11a show a significantly different distribution. The same intensity of 800 nm (5 TW/cm^2) and 266 nm (0.23 TW/cm^2) was used in both samples. In MgO, the wavemixing signal is dominated by the 0-mrad and ± 4-mrad signal. The wavemixing at 0 mrad originates from a combination of the main generation of H7 from 800-nm photons, and in addition the wavemixing signal with one photon of each 266-nm arm, combined with one 800-nm photon. The signal at ±4 mrad is constructed by the combination of four 800-nm photons and one 266-nm photon. Interesting to observe is that in SiO_2 the wavemixing signal is dominated by two-266-nm photon and one 800-nm photon mixing, which corresponds to the signal at ± 10 mrad. In SiO_2 the absorption of 266-nm is lower, due to the larger bandgap, such that the remaining intensity after propagation through the sample at the back surface is higher than in MgO. In addition, for the

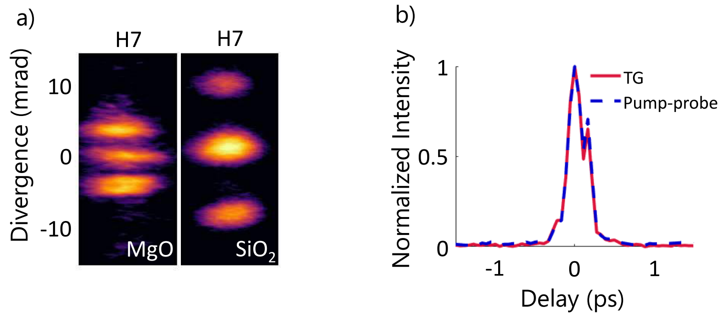

Figure 7.11: a) Wavemixing of H7 in MgO and SiO2 at zero time delay. b) Delay trace of the signal at -10 mrad with two 266-nm arms (TG) and only one 266-arm (pump-probe).

chosen 800-nm intensity, the main generation of H7 is also less efficient than in MgO. To identify if there are any electron dynamics that influence the HHG process, we compare a transient-grating and pump-probe configuration in SiO_2 in Fig. 7.11b. In the case of a transient-grating configuration, the wavemixing signal at $\pm$ 10 mrad overlaps with the angle at which a transient-grating signal would appear. The intensity of the signal at -10 mrad is tracked as a function of time delay, corresponding to the red line in Fig. 7.11b. In the case that one 266-nm arm is blocked, we only track the wavemixing component, and obtain the blue line. The identical shape of the intensity trace in time, shows that no additional transient-grating signal is discernible, and the entire signal is dominated by wavemixing. The 266-nm pulses are not capable of producing a significant excited carrier population. Therefore, a higher photon energy should be used for photoexcitation to explore the dynamics of an excited carrier population in SiO_2.

7.5. Conclusion and outlook

In conclusion, we have demonstrated transient-grating high-harmonic spectroscopy in MgO to determine the effect of an excited carrier population on the solid HHG process. The method enables the reconstruction of the relative amplitude and phase modulation of the harmonic near-field, which originates from an excited carrier population that is induced by two-photon absorption of 266 nm light. The total reconstructed phase and amplitude are a combination of macroscopic propagation effects of the fundamental wavefront and microscopic contributions due to a modified HHG process. Additional transient-grating spectroscopy on the fundamental wavefront allows to disentangle the macroscopic contributions from the microscopic contributions. The importance of each contribution will have to be determined in future measurement, performed under identical transient-grating conditions. Subsequent advanced simulations provide a new way to relate the remaining microscopic phase and amplitude to the solid HHG process. More specifically, the relative microscopic phase could be related directly to a modification of the energy levels in MgO, induced by the excited carrier population. Moreover, preliminary simulations suggests that an excited carrier population enhances the efficiency of solid HHG. Overall, the presented combination of transient-grating spectroscopy performed on the fundamental wavefront and on the generated high harmonics provides a complete method to disentangle phase and amplitude contributions of macroscopic and microscopic contributions of HHG in the presence of an excited carrier population.

A

Electron Density Rate Equations

In Chapter 2.2.1 we discuss several approximations to describe the ionization mechanism for the excitation of electrons. The equations to calculate the ionization rates are presented here, and are based on the approach presented in [78]. The growth of the electron density due to strong-field ionization was described by Keldysh [74] for gases and solids. In the original work, Keldysh approximated the electron density rate for the case that tunnel ionization (TI) is the dominant photoionization process, described as,

$$\begin{aligned} W_{\mathrm{TI}} = \frac{2}{9\pi^2}\frac{E_{\mathrm{g}}}{\hbar}\left(\frac{m_e E_{\mathrm{g}}}{\hbar^2}\right)^{3/2}\left(\frac{e\hbar F}{\sqrt{m_e}E_{\mathrm{g}}^{3/2}}\right)^{5/2} \times \\ \exp\left[-\frac{\pi}{2}\frac{\sqrt{m_e}E_{\mathrm{g}}^{3/2}}{e\hbar F}\left(1-\frac{1}{8}\frac{m_e\omega^2 E_{\mathrm{g}}}{e^2F^2}\right)\right], \end{aligned} \tag{A.1}$$

with E_{g} the bandgap of the material, m_e the effective electron mass, e the electronic charge, ω the central angular frequency and F the field strength. Additionally, he approximated the electron density rate for the case that multi-photon ionization (MPI) is the dominant process,

$$\begin{aligned} W_{\mathrm{MPI}} = \frac{2\omega}{9\pi}\left(\frac{m_e\omega}{\hbar}\right)^{3/2}\phi\left[\left(2\left(\frac{E_{\mathrm{g}}^*}{\hbar\omega}+1\right)-\frac{2E_{\mathrm{g}}^*}{\hbar\omega}\right)^{1/2}\right] \times \\ \exp\left[2\left(\frac{E_{\mathrm{g}}^*}{\hbar\omega}+1\right)\left(1-\frac{e^2F^2}{4m_e\omega^2E_{\mathrm{g}}}\right)\right] \times \left(\frac{e^2F^2}{16m_e\omega^2E_{\mathrm{g}}}\right)^{(E_{\mathrm{g}}^*/\hbar\omega+1)}. \end{aligned} \tag{A.2}$$

Here, E_{g}^* represents the effective bandgap, given by,

$$E_{\mathrm{g}}^* = E_{\mathrm{g}} + \frac{e^2F^2}{4m_e\omega^2}, \tag{A.3}$$

and $\phi(x)$ represents the Dawson function,

$$\phi(x) = e^{-x^2} \int_0^x e^{-t^2} \mathrm{d}t. \tag{A.4}$$

The complete rate equation that Keldysh formulated in [74] is given by,

$$\begin{aligned} W_{\mathrm{SFI}} = \frac{2\omega}{9\pi} \left(\frac{\sqrt{1+\gamma^2}}{\gamma} \frac{m_e \omega}{\hbar} \right)^{3/2} Q\left(\gamma, \frac{E_{\mathrm{g}}^*}{\hbar\omega}\right) \quad \times \\ \exp\left\{ -\pi \left(\frac{E_{\mathrm{g}}^*}{\hbar\omega} + 1 \right) \times \left[K\left(\frac{\gamma}{\sqrt{1+\gamma^2}} \right) - E\left(\frac{\gamma}{\sqrt{1+\gamma^2}} \right) \right] / E\left(\frac{1}{\sqrt{1+\gamma^2}} \right) \right\}, \end{aligned} \tag{A.5}$$

where the function Q refers to,

$$\begin{aligned} Q(\gamma, x) = \left[\pi / 2K\left(\frac{1}{\sqrt{1+\gamma^2}} \right) \right]^{1/2} \times \\ \sum_{n=0}^{\infty} \exp\left\{ -\pi \left[K\left(\frac{\gamma}{\sqrt{1+\gamma^2}} \right) - E\left(\frac{\gamma}{\sqrt{1+\gamma^2}} \right) \right] n / E\left(\frac{1}{\sqrt{1+\gamma^2}} \right) \right\} \times \\ \phi\left\{ \left[\pi^2 (2\langle x+1 \rangle - 2x + n) / 2K\left(\frac{1}{\sqrt{1+\gamma^2}} \right) E\left(\frac{1}{\sqrt{1+\gamma^2}} \right) \right]^{1/2} \right\}. \end{aligned} \tag{A.6}$$

The quantities K and E correspond to elliptical integrals of the first and second kind respectively. Within the strong-field ionization rate, the effective bandgap is reformulated as,

$$E_{\mathrm{g}}^* = \frac{2}{\pi} E_{\mathrm{g}} \frac{\sqrt{1+\gamma^2}}{\gamma} E\left(\frac{1}{\sqrt{1+\gamma^2}} \right). \tag{A.7}$$

For completeness, the Keldysh parameter is given by,

$$\gamma = \frac{\omega}{e} \left[\frac{m_e c n \epsilon_0 E_{\mathrm{g}}}{I} \right]^{1/2} \tag{A.8}$$

with I the intensity of the light.

B

Sample preparation

The experiments described in Chapter 5 and Chapter 6 are performed using fused silica samples. The cleaning procedure and the techniques to structure these silica samples are described in this appendix.

B.1. Cleaning procedure

The 100 µm-thick amorphous fused silica samples utilized in this thesis were purchased from UQG Optics (CFS-1010 UV Coverslip) and cleaned with an acid piranha (H_2O / 37% NH_4OH / 30% H_2O_2, 5:1:1 mixture) solution at 70 degrees for 15 minutes, followed by isopropanol cleaning, prior to experimentation.

B.2. Structured samples

All structures are made on approximately 100 µm thick fused silica substrates (supplied by UQG Optics, Part No. CFS-1010). Before patterning, the substrates are cleaned following a base piranha procedure. Photoresists (Shipley microposit S1813 for UV lithography and CSAR 62 for e-beam lithography) are spincoated using a SUSS Delta 80 Spin Coater. The gratings with micrometer pitch, and the micrometer pillar array are fabricated by UV lithography (SUSS MA/BA 6 MASK Aligner). The nanometer grating and the more complex smiley pattern are made with electron beam Lithography (Raith e-LiNE lithography system Voyager). Etching of the substrates is done by reactive ion etching (Oxford Plasmalab 80+ Ion Beam Etching).

The gratings with micrometer pitch and micrometer array pillar samples are characterized using optical microscopy (Zeiss Axioskop2) and a surface profilometer (KLA-Tencor stylus profiler P7), to determine the pitch and the height of the structures, see Figs. B.1 and B.2.

The grating with 200 nm linewidth is characterized using an atomic force microscope (Bruker Dimension icon XR). The height and pitch of the grating is measured before and

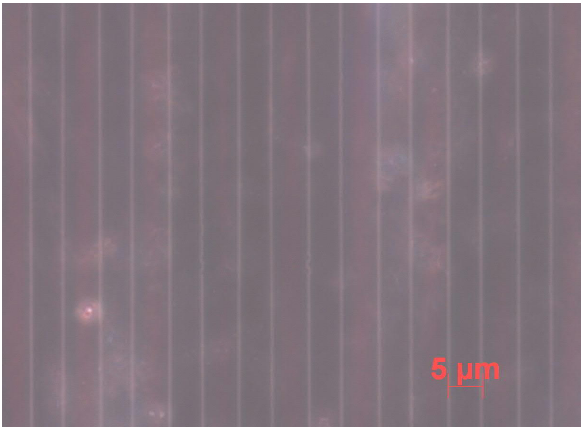

Figure B.1: Optical microscope image of the grating with 10 µm pitch and 5 µm linewidth.

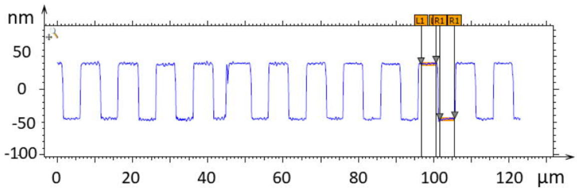

Figure B.2: Height determination of the grating with 10 µm pitch, using a profilometer. The height is measured to be 85 nm ± 3 nm.

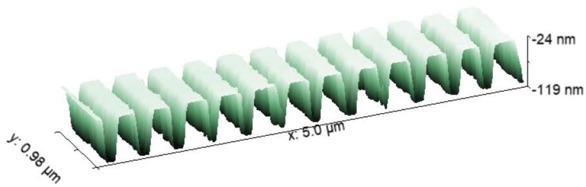

Figure B.3: Atomic force microscope image of the nanometric structure (400 nm pitch, 200 nm linewidth, 85 nm height), measured before the experiment.

after the measurements, to exclude degradation of the structure during the measurements (see Fig. B.3).

C

Simulations of HHG from nanostructures

In Chapter 5.3, we describe the generation of high harmonics from nanostructured silica and compare the experimental results with simulations, of which the details are described in this appendix.

C.1. Numerical simulations for nanostructured grating

Numerical modelling of HHG was performed in "fundamental-to-harmonic" sequence [216, 217] in a two-dimensional frequency-domain model using commercial finite-element software COMSOL Multiphysics. The geometry of our model is shown in Fig. C.1. It consists of a finite-sized rectangular grating of depth 85 nm, pitch 400 nm, linewidth 200 nm, and corner curvature radius 15 nm. The number of grooves was 100, yielding a total grating extent of 40 µm along the horizontal (x) direction (the grooves were effectively infinite along the out-of-plane (z) direction). The grating was placed on top of a substrate, modelled as a rectangle of height (y) 2.5 µm and width (x) 50 µm, and with frequency-dependent optical constants (n, k) of silica based on [117].

Freq.	Maximum element size [nm]			# Mesh Elements
	Red area	Green area	Blue area	
H1	10 ($\lambda_{SiO2}/54.8$)	25 ($\lambda/32$, $\lambda_{SiO2}/21.9$)	50 ($\lambda/16$, $\lambda_{SiO2}/11$)	5092922
H3	10 ($\lambda_{SiO2}/17.7$)	25 ($\lambda/10.7$, $\lambda_{SiO2}/7.1$)	50 ($\lambda/5.3$, $\lambda_{SiO2}/3.5$)	5092922
H5	10 ($\lambda_{SiO2}/9.7$)	25 ($\lambda/6.4$, $\lambda_{SiO2}/3.9$)	50 ($\lambda/3.2$, $\lambda_{SiO2}/1.9$)	5092922
H7	10 ($\lambda_{SiO2}/6.5$)	25 ($\lambda/4.6$, $\lambda_{SiO2}/2.6$)	50 ($\lambda/2.3$, $\lambda_{SiO2}/1.3$)	5092922
H9	10 ($\lambda_{SiO2}/6.7$)	20 ($\lambda/4.4$, $\lambda_{SiO2}/3.4$)	40 ($\lambda/2.2$, $\lambda_{SiO2}/1.7$)	7680278
H11	10 ($\lambda_{SiO2}/6.6$)	16 ($\lambda/4.5$, $\lambda_{SiO2}/4.1$)	32 ($\lambda/2.3$, $\lambda_{SiO2}/2.1$)	11308501

Table C.1: Mesh parameters in different areas of the model, as highlighted in Fig. C.1(a). The wavelength inside SiO2 and vacuum are defined as λ_{SiO2} and λ respectively.

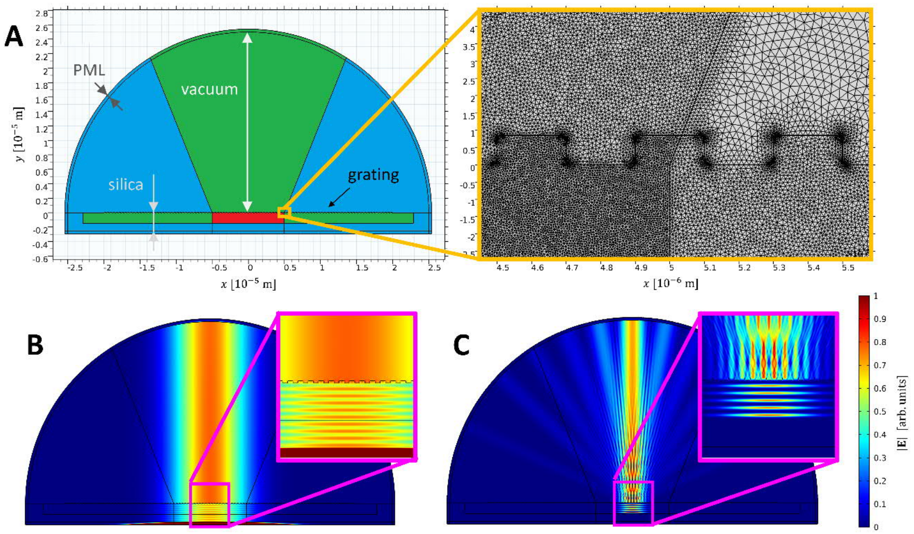

Figure C.1: (a) Geometry of the model used to simulate HHG in COMSOL. The simulation space consists of a rectangular block of silica with a grating on its top side, enclosed by a semi-circular vacuum region. The outermost layer is PML (Perfectly Matched Layer) with zero-field scattering boundary condition at the outer boundaries, except for the bottom boundary at fundamental frequency, where a source of electric field is defined. Different colors (red, green, blue) indicate areas of different mesh element sizes. (b,c) Example electric field distribution at the fundamental (b) and the 11th harmonic (c) for the incident field polarized at 45° with respect to the grating

To enable approximately free-space propagation of HHG diffraction orders, the upper (vacuum) part of the simulation space was shaped into a semi-circle of radius 25 μm (matching the horizontal extent of the substrate). The entire simulation space (rectangle + semi-circle) was additionally surrounded by a 400 nm-thick perfectly matched layer (PML), with scattering boundary condition set at the outermost boundaries. The mesh was adjusted to the wavelength of subsequent harmonics, and, furthermore, different areas of the simulation were meshed with various maximum element sizes, depending on their importance, which is summarized in table C.1. For example, a finer mesh was used in the silica volume in which the HHG occurs (red area in Fig. C.1(a)), or in the vacuum area through which the zeroth and first diffraction orders propagate (central green area in Fig. C.1(a)). Further details on the stability of the solutions can be found in the next section, convergence study.

Simulations at fundamental frequency (corresponding to free-space wavelength 800 nm) were performed assuming zero field everywhere except for the bottom boundary, where we set a Gaussian-profile excitation defined as $\propto (\hat{\mathbf{x}}\sin\alpha + \hat{\mathbf{z}}\cos\alpha)\exp(-iky - x^2/w^2)$, where $\hat{\mathbf{x}}$ and $\hat{\mathbf{z}}$ are the in-plane and out-of-plane unit vectors, α is the polarization angle of incident fundamental beam, and $w = 5$ μm. The model was solved at seven different polarization angles of incident electric field: 0°, 15°, 30°, 45°, 60°, 75°, and 90°, where $\alpha = 0°$ corresponds to the polarization along z (out-of-plane, along the grooves of

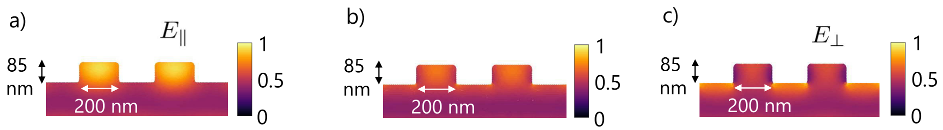

Figure C.2: Simulated field distribution of the fundamental field inside the nanostructured silica grating for 90°, 45°, and 0°, respectively. The color scale represents the intensity, normalized to the maximum intensity of the parallel configuration.

the grating), whereas $\alpha = 90°$ means the polarization along x (in-plane, perpendicular to the grooves, parallel to the periodicity axis). These simulations yielded spatial distributions of total (incident + scattered) electric field at fundamental frequency, which are shown in Fig. C.2(a,b,c) for 90°, 45°, and 0°, respectively.

Two different approaches were used to simulate HHG. In the first approach, we assumed that the HHG is a direct process, in which the fundamental beam is directly converted to the n^{th} harmonic via n^{th}-order nonlinear process. Therefore, the modeling sequence consisted of only two steps, performed separately for each of the considered polarization angles, the first step at the fundamental frequency (as described above), and the second step at the 5^{th}, 7^{th}, 9^{th}, and 11^{th} harmonic frequency (free-space wavelengths: 160, 114, 89, and 73 nm, respectively). In all simulations of the second step, the field was assumed zero at all outer boundaries, and the nonlinear polarization density $\mathbf{P}_{n\omega} = \epsilon_0 \chi^{(n)} (\mathbf{E}_\omega \cdot \mathbf{E}_\omega)^{n/2-1/2} \mathbf{E}_\omega$ was used as the source term within the red area in Fig. C.1(a), taking as input the fundamental electric field $\mathbf{E}_\omega$ simulated in the previous step. This formula was used for all harmonics, providing isotropic nonlinear optical response and the corresponding n^{th} power law dependence. In the second approach, applied to the simulations of H7, we have included two possible contributions of cascaded processes, as motivated in the main text. The first type of cascade under consideration was H7 due to third-order sum-frequency generation (SFG) of the fundamental and twice of H3. In this case, the nonlinear polarization density was calculated as $\mathbf{P}_{7\omega} = \epsilon_0 \chi^{(3)}_{\text{cas}} (\mathbf{E}_{3\omega} \cdot \mathbf{E}_{3\omega}) \mathbf{E}_\omega$, using as input the fundamental field $\mathbf{E}_\omega$ obtained in the first simulation step, and the 3rd harmonic field $\mathbf{E}_{3\omega}$ obtained in the additional, intermediate simulation step from $\mathbf{P}_{3\omega} = \epsilon_0 \chi^{(3)}_{\text{direct}} (\mathbf{E}_\omega \cdot \mathbf{E}_\omega) \mathbf{E}_\omega$. The second type of cascade was H7 originating from SFG of the H5 and twice the fundamental, with nonlinear polarization obtained from $\mathbf{P}_{7\omega} = \epsilon_0 \chi^{(3)}_{\text{cas}} (\mathbf{E}_\omega \cdot \mathbf{E}_\omega) \mathbf{E}_{5\omega}$. We reproduced the experimentally measured polarization dependence of the zeroth and the first diffraction order of H7 by simultaneously fitting both data sets, using complex-valued coefficients describing subsequent contributions as fitted parameters, and coherently adding complex-valued Cartesian components of the electric and magnetic fields resulting from these contributions, taking advantage of the superposition principle applied to radiated fields. Finally, the time-averaged power flow was calculated from the summed fields as $\propto \frac{1}{2}\text{Re}\{H_z^* E_y - H_y^* H_z\} n_x + \frac{1}{2}\text{Re}\{-H_z^* E_x + H_x^* E_z\} n_y$, with n_x, n_y being the components of the unit vector normal to the boundary. The simulations inherently take into account macroscopic phase matching due to the different refractive indices of XUV and IR in silica into account. Since the cascaded processes are dependent on the optical constants and structure-induced near-field effects at intermediate frequencies, one can envision that using resonances at intermediate frequencies may be a very promising strategy for tuning the contributions towards constructive interference [182]. Including the contribution of cascaded frequency conversion could possibly resolve the discrepancies between experiments and simulations also for other harmonics (especially those above the band gap, such as H9). However, we refrain from such detailed analysis, as our main intention in this work is to signal the possibility that such effects could play a significant role (on the example of H7), while they are certainly not the only factors determining the observed properties of HHG (with other potentially significant factors being transient and non-classical dynamics, which are not included in our frequency-domain simulations). Furthermore, higher-order harmonics such as H9 may contain contributions of a larger number of different types of cascades, which makes the analysis analogous to that performed for H7 significantly more tedious.

At the end of all HHG simulations, the power scattered to subsequent diffraction orders was obtained by fitting the appropriate spatial distributions of the time-averaged power flow over selected ranges of the semi-circular inner PML boundary using a Gaussian function, matching the beam profile inherited by subsequent harmonics after the fundamental beam. To illustrate this procedure, we present examples of such Gaussian fits for 11^{th} harmonic in Fig. C.3. Fitting the profiles of radiated HHG beams by Gaussian curves renders our results insensitive to the interference between spatially overlapping tails of the neighboring diffraction orders. To calculate the Stokes parameters presented in Table 5.1, we used complex-valued Cartesian components of the scattered electric fields obtained at the same PML boundary.

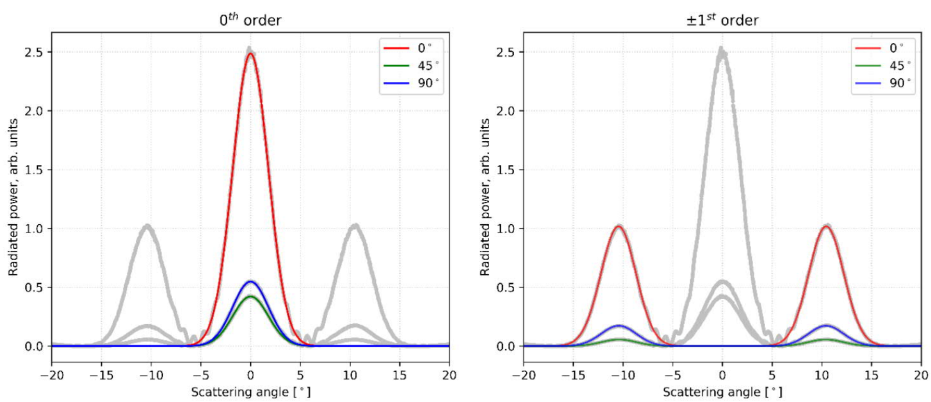

Figure C.3: Examples of the Gaussian fits (red, green, and blue lines) of the zeroth (left) and first (right) diffraction orders in the simulated radiated power (gray) at the inner PML boundary for the 11^{th} harmonic at polarization angles 0°, 45°, 90° (red, green, blue, respectively).

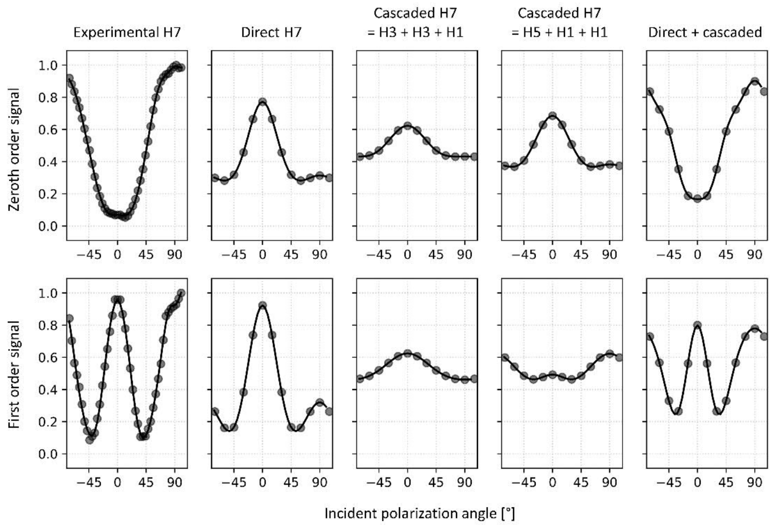

Figure C.4: Polarization dependence of the zeroth (top row) and the first diffraction order (bottom row) of the 7th harmonic: comparison of the experimental data (first column, the same as plotted in Fig. 5.9) with the separated contributions of direct and cascaded H7 simulated in COMSOL (columns 2-4). The last column shows the polarization dependence (the same as plotted in Fig. Fig. 5.9 in the main text) obtained by coherent superposition of three different contributions to the radiated H7 electromagnetic fields multiplied by complex coefficients: 1+0i for the direct process, -2.305-0.766i for the first cascaded process (third-order SFG of the fundamental and H3), and 2.291-2.153i for the second cascaded process (third-order SFG of the fundamental and H5).

C.2. Convergence study

Table C.1 shows that the mesh settings for the critical areas of our COMSOL model are in the regime that is generally accepted as sufficient for optical simulations. The central region of nonlinear polarization in silica (red area in Fig. C.1(a)) is resolved with more than 6 elements per wavelength (including correction by refractive index), whereas the regions of HHG propagation in vacuum (upper green area) are resolved with more than 4 elements per wavelength. On the other hand, the side regions containing residual fraction of optical fields are poorly meshed due to limited computational resources. However, the mesh quality in these regions does not significantly influence the radiated HHG power of the zeroth and first diffraction orders, which is demonstrated by a convergence study presented in Fig. C.5, using H11 as an example. Here, the mesh settings, labelled with letters A, B, ..., are tuned from extremely coarse (A) to extremely fine (E), as specified in Table C.2. Here, settings labelled with 'D' correspond to the settings used to obtain the results for H11 presented in this work. The mesh parameters are tuned only for the side regions (blue area, green area in silica), while the parameters in the critical regions are not changed. The largest variation between poorly meshed (A) and well meshed (E) simulation results is found to be around 8%, which is observed in the absolute radiated power under incident polarization 0°. However, when considering the ratio between radiated HHG power at different polarization angles (i.e. the shape of polarization response of HHG), this variation does not exceed 5%. With mesh settings 'D', used to obtain the results presented in this work, we are very clearly in the 'safe zone', with variation between 'D' and 'E' not exceeding 0.05% in the absolute power and 0.025% in the power ratio. The situation may be slightly worse for other harmonics, especially for H7, in case of which the mesh parameters in the side regions are close to 'B' in the A-E scale (due to the high refractive index of silica at that frequency). However, even in such case, the eventual error would likely not exceed 5% in the power ratio, as suggested by the results presented here, hence not affecting the simulated polarization response in a visible way.

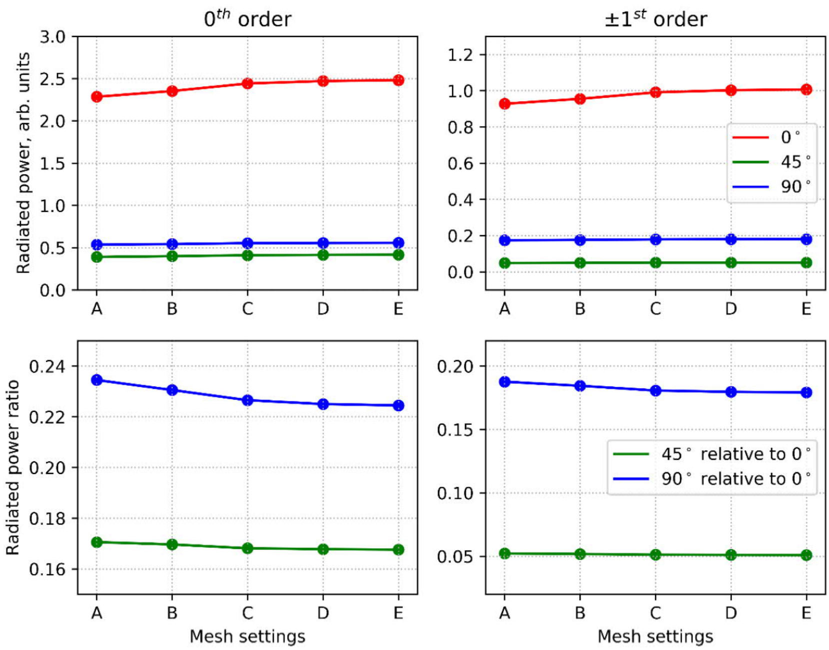

Figure C.5: Convergence study for H11. The top plots show the absolute radiated power (in arbitrary units) for subsequent polarization angles (0°, 45°, 90°) of the fundamental beam, whereas the bottom plots show the H11 power generated under incident polarization 45° and 90° relative to the power generated under incident polarization 0°. Mesh settings corresponding to labels A, B, . . . , are provided in Table C.2

Mesh settings (Fig. C.1)	Element size [nm]	
	Green area in silica	Blue area
A	30 ($\lambda_{SiO2}/2.2$)	60 ($\lambda/1.2$, $\lambda_{SiO2}/1.1$)
B	25 ($\lambda_{SiO2}/2.6$)	50 ($\lambda/1.5$, $\lambda_{SiO2}/1.3$)
C	20 ($\lambda_{SiO2}/3.3$)	40 ($\lambda/1.8$, $\lambda_{SiO2}/1.6$)
D	16 ($\lambda_{SiO2}/4.1$)	32 ($\lambda/2.3$, $\lambda_{SiO2}/2.1$)
E	13 ($\lambda_{SiO2}/5.1$)	26 ($\lambda/2.8$, $\lambda_{SiO2}/2.5$)

Table C.2: Mesh parameters for the blue areas and green areas in silica (Fig. C.1) used in the convergence study (Fig. C.5). The wavelength inside SiO2 and vacuum are defined as λ_{SiO2} and λ respectively.

C.3. Lack of resonant confinement

Rigorous modelling of ultrafast phenomena typically requires time-domain simulation approaches such as FDTD. However, taking into account the large size of our model, as well as extremely high resolution of spatio-temporal grids required for the stability of FDTD algorithms, such approaches would be impractical in this case. Hence, we used frequency-domain FEM method, which is more feasible in terms of computational resources. Such approximation is further justified by the lack of resonant field enhancement in the studied silica grating, which is explained below and in Figure C.6. Every nanostructure that supports some kind of optical resonances will modify the temporal dynamics of the optical fields by the ring down effects. In other words, the optical energy would be stored for some time (proportional to the resonance Q factor), decaying exponentially, leading to time-dependent enhancement of the local optical fields, which could have significant effect especially on the nonlinear optical phenomena. In such case, a transient time-domain modelling approach would be inevitable to accurately predict the optical response of the system. However, the nanostructures considered in this work do not support any kind of such resonant field confinement, which we have confirmed by performing eigenfrequency analysis in COMSOL. We have used a model consisting of a single unit cell of the grating, with a thick (5 µm) layer of silica below the grating, and with similarly thick layer of vacuum above the grating, both terminated by 1 µm tick perfectly matched layers (PML) which emulate the radiative damping of the fields at infinity. The in-plane momentum ($k_{\|}$, in the units of π/a, where a = 400 nm is the grating period) is set by the Floquet periodic boundary condition, swept over half of the first Brillouin zone. The overall design of this model is conceptually similar to that used to reveal the eigenmodes of a diffractive metasurface in [218]. Here, we have used such model to reveal optical eigenmodes supported by the grating, and we have investigated the degree of spatial confinement of optical fields associated with these eigenmodes. We have quantified this spatial confinement by numerically evaluating the fraction of electromagnetic energy density $U = \frac{1}{2}n^2\epsilon_0|\mathbf{E}|^2$ contained within a distance of <1 µm from the surface of the grating. Since the total thickness of the model geometry is 10 µm (excluding the PML), a fraction of 10% or less is equivalent to the lack of confinement. Results of this eigenfrequency analysis are presented in Fig.C.6, in which two types of geometries are considered. The first (on the left) is identical to the grat-

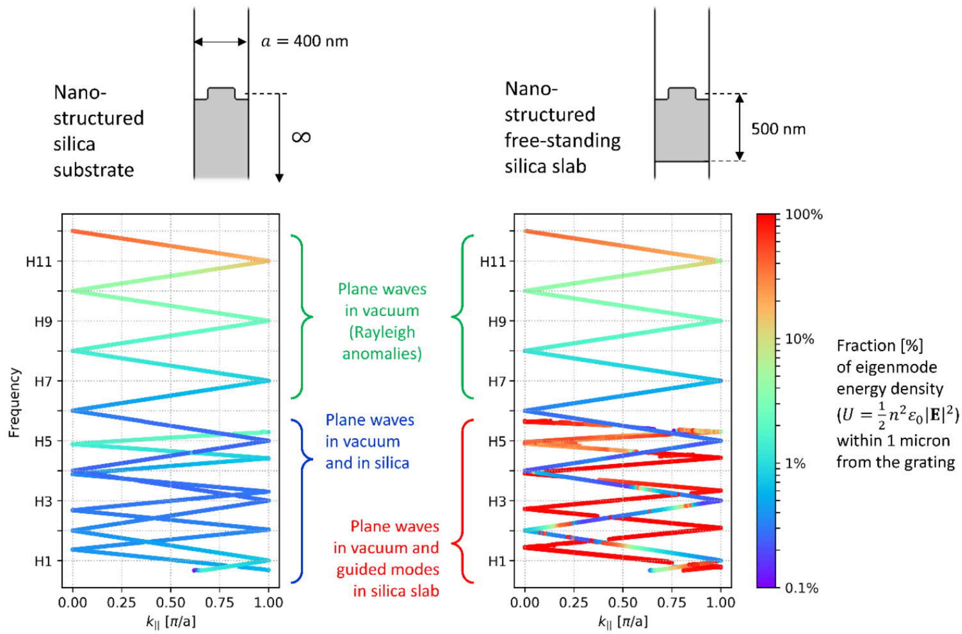

Figure C.6: Results of eigenfrequency analysis in COMSOL, performed for the silica grating (on the left, equivalent to the grating studied in this work) and for a free-standing nanostructured silica slab (on the right). In both cases, only one unit cell is modelled, with in-plane momentum ($k_{\|}$) set by the Floquet periodic boundary condition. The color of the lines corresponds to the degree of spatial confinement of the eigenmodes in the vicinity of the grating's surface.

ing investigated in this work, while the second geometry (on the right) is a 500 nm thick nanostructured free-standing silica slab, which is investigated for comparison. In the first case (on the left), the degree of eigenmode energy confinement does not exceed 10% (blue color of the lines), except for the high frequencies (around H11). This means that all eigenmodes found in this simulation are freely propagating plane waves, folded into the first Brillouin zone by the grating periodicity, forming so-called Rayleigh anomalies. Similar eigenmodes are found in the second case (free-standing slab, on the right), however, the degree of confinement is significantly higher (red color of the lines), as guided modes of the slab turn into resonant Bloch modes. Such structure should be regarded as a system with resonant field enhancement, requiring a time-domain approach for accurate modelling of ultrafast optical phenomena, as opposed to the non-resonant grating structure central to this work.

Bibliography

1. Maiman, T. H. Stimulated Optical Radiation in Ruby. *Nature* **187,** 493–494 (1960).
2. DeMaria, A. J., Glenn, W. H., Brienza, M. J. & Mack, M. E. Picosecond laser pulses. *Proc. IEEE* **57,** 2–25 (1969).
3. Ippen, E., Shank, C. & Dienes, A. Passive mode locking of the cw dye laser. *Appl. Phys. Lett.* **21,** 348–350 (1972).
4. Shank, C. & Ippen, E. Subpicosecond kilowatt pulses from a mode-locked cw dye laser. *Appl. Phys. Lett.* **24,** 373–375 (1974).
5. Strickland, D. & Mourou, G. Compression of amplified chirped optical pulses. *Opt. Commun.* **55,** 447–449 (1985).
6. NobelPrize.org. *The Nobel Prize in Physics 2018,* `https://www.nobelprize.org/prizes/physics/2018/summary/`. Accessed: 02-09-2022.
7. Franken, P. A., Hill, A. E., Peters, C. W. & Weinreich, G. Generation of optical harmonics. *Phys. Rev. Lett.* **7,** 118 (1961).
8. Boyd, R. W. *Nonlinear optics* (Academic press, 2020).
9. Abbe, E. Beiträge zur Theorie des Mikroskops und der mikroskopischen Wahrnehmung. *Archiv für mikroskopische Anatomie* **9,** 413–468 (1873).
10. Levinson, H. J. *Principles of Lithography* (SPIE press, 2005).
11. Zewail, A. H. Femtochemistry: atomic-scale dynamics of the chemical bond using ultrafast lasers (Nobel Lecture). *Angew. Chem. Int. Ed.* **39,** 2586–2631 (2000).
12. Krausz, F. & Ivanov, M. Attosecond physics. *Rev. Mod. Phys.* **81,** 163 (2009).
13. McPherson, A. *et al.* Studies of multiphoton production of vacuum-ultraviolet radiation in the rare gases. *J. Opt. Soc. Am. B.* **4,** 595–601 (1987).
14. Ferray, M. *et al.* Multiple-harmonic conversion of 1064 nm radiation in rare gases. *J. Phys. B: At. Mol. Opt. Phys.* **21,** L31 (1988).
15. Corkum, P. B. Plasma perspective on strong field multiphoton ionization. *Phys. Rev. Lett.* **71,** 1994 (1993).
16. Schafer, K., Yang, B., DiMauro, L. & Kulander, K. Above threshold ionization beyond the high harmonic cutoff. *Phys. Rev. Lett.* **70,** 1599 (1993).
17. Corkum, P., Burnett, N. & Ivanov, M. Y. Subfemtosecond pulses. *Opt. Lett.* **19,** 1870–1872 (1994).
18. Drescher, M. *et al.* X-ray Pulses Approaching the Attosecond Frontier. *Science* **291,** 1923–1927 (2001).
19. Hentschel, M. *et al.* Attosecond metrology. *Nature* **414,** 509–513 (2001).

20. Drescher, M. *et al.* Time-resolved atomic inner-shell spectroscopy. *Nature* **419,** 803–807 (2002).
21. Uiberacker, M. *et al.* Attosecond real-time observation of electron tunnelling in atoms. *Nature* **446,** 627–632 (2007).
22. Holler, M., Schapper, F., Gallmann, L. & Keller, U. Attosecond Electron Wave-packet Interference Observed by Transient Absorption. *Phys. Rev. Lett.* **106,** 123601 (2011).
23. Cavalieri, A. L. *et al.* Attosecond spectroscopy in condensed matter. *Nature* **449,** 1029–1032 (2007).
24. Chapman, H. N. & Nugent, K. A. Coherent lensless X-ray imaging. *Nat. Photonics* **4,** 833–839 (2010).
25. Sakdinawat, A. & Attwood, D. Nanoscale X-ray imaging. *Nat. Photonics* **4,** 840–848 (2010).
26. Abbey, B. *et al.* Lensless imaging using broadband X-ray sources. *Nat. Photonics* **5,** 420–424 (2011).
27. Witte, S., Tenner, V. T., Noom, D. W. & Eikema, K. S. Lensless diffractive imaging with ultra-broadband table-top sources: from infrared to extreme-ultraviolet wavelengths. *Light Sci. Appl.* **3,** e163–e163 (2014).
28. Miao, J., Ishikawa, T., Robinson, I. K. & Murnane, M. M. Beyond crystallography: Diffractive imaging using coherent x-ray light sources. *Science* **348,** 530–535 (2015).
29. Lein, M. Attosecond Probing of Vibrational Dynamics with High-Harmonic Generation. *Phys. Rev. Lett.* **94,** 053004 (2005).
30. Itatani, J. *et al.* Tomographic imaging of molecular orbitals. *Nature* **432,** 867–871 (2004).
31. Peng, P., Marceau, C. & Villeneuve, D. M. Attosecond imaging of molecules using high harmonic spectroscopy. *Nat. Rev. Phys* **1,** 144–155 (2019).
32. Lewenstein, M., Balcou, P., Ivanov, M. Y., L'huillier, A. & Corkum, P. B. Theory of high-harmonic generation by low-frequency laser fields. *Phys. Rev. A* **49,** 2117 (1994).
33. Johnson, A. S., Avni, T., Larsen, E. W., Austin, D. R. & Marangos, J. P. Attosecond soft X-ray high harmonic generation. *Philos. Trans. R. Soc. A* **377,** 20170468 (2019).
34. Wegener, M. *Extreme Nonlinear Optics: An Introduction* (Springer Science & Business Media, 2005).
35. Golde, D., Meier, T. & Koch, S. W. High harmonics generated in semiconductor nanostructures by the coupled dynamics of optical inter-and intraband excitations. *Phys. Rev. B* **77,** 075330 (2008).
36. Ghimire, S. *et al.* Observation of high-order harmonic generation in a bulk crystal. *Nat. Phys.* **7,** 138–141 (2011).
37. Schubert, O. *et al.* Sub-cycle control of terahertz high-harmonic generation by dynamical Bloch oscillations. *Nat. Photonics* **8,** 119–123 (2014).
38. Langer, F. *et al.* Lightwave-driven quasiparticle collisions on a subcycle timescale. *Nature* **533,** 225–229 (2016).

39. Lanin, A., Stepanov, E., Fedotov, A. & Zheltikov, A. Mapping the electron band structure by intraband high-harmonic generation in solids. *Optica* **4,** 516–519 (2017).

40. Luu, T. T. *et al.* Extreme ultraviolet high-harmonic spectroscopy of solids. *Nature* **521,** 498–502 (2015).

41. Garg, M. *et al.* Multi-petahertz electronic metrology. *Nature* **538,** 359–363 (2016).

42. Gholam-Mirzaei, S., Beetar, J. & Chini, M. High harmonic generation in ZnO with a high-power mid-IR OPA. *Appl. Phys. Lett.* **110,** 061101 (2017).

43. You, Y. S., Reis, D. A. & Ghimire, S. Anisotropic high-harmonic generation in bulk crystals. *Nat. Phys.* **13,** 345–349 (2017).

44. Kim, H., Han, S., Kim, Y. W., Kim, S. & Kim, S.-W. Generation of Coherent Extreme-Ultraviolet Radiation from Bulk Sapphire Crystal. *ACS photonics* **4,** 1627–1632 (2017).

45. Vampa, G., You, Y., Liu, H., Ghimire, S. & Reis, D. Observation of backward high-harmonic emission from solids. *Opt. Express* **26,** 12210–12218 (2018).

46. Hirori, H. *et al.* High-order harmonic generation from hybrid organic–inorganic perovskite thin films. *APL Materials* **7,** 041107 (2019).

47. Liu, H. *et al.* High-harmonic generation from an atomically thin semiconductor. *Nat. Phys.* **13,** 262–265 (2017).

48. Yoshikawa, N., Tamaya, T. & Tanaka, K. High-harmonic generation in graphene enhanced by elliptically polarized light excitation. *Science* **356,** 736–738 (2017).

49. Korobenko, A. *et al.* High-harmonic generation in metallic titanium nitride. *Nat. Commun.* **12,** 4981 (2021).

50. Sivis, M. *et al.* Tailored semiconductors for high-harmonic optoelectronics. *Science* **357,** 303–306 (2017).

51. Vampa, G. *et al.* Plasmon-enhanced high-harmonic generation from silicon. *Nat. Phys.* **13,** 659–662 (2017).

52. Liu, H. *et al.* Enhanced high-harmonic generation from an all-dielectric metasurface. *Nat. Phys.* **14,** 1006–1010 (2018).

53. Franz, D. *et al.* All semiconductor enhanced high-harmonic generation from a single nanostructured cone. *Sci. Rep.* **9,** 5663 (2019).

54. Vampa, G. *et al.* All-Optical Reconstruction of Crystal Band Structure. *Phys. Rev. Lett.* **115,** 193603 (2015).

55. Borsch, M. *et al.* Super-resolution lightwave tomography of electronic bands in quantum materials. *Science* **370,** 1204–1207 (2020).

56. Costello, J. *et al.* Reconstruction of Bloch wavefunctions of holes in a semiconductor. *Nature* **599,** 57–61 (2021).

57. Uzan, A. J. *et al.* Attosecond spectral singularities in solid-state high-harmonic generation. *Nat. Photonics* **14,** 183–187 (2020).

58. Luu, T. T. & Wörner, H. J. Measurement of the Berry curvature of solids using high-harmonic spectroscopy. *Nat. Commun.* **9,** 916 (2018).

59. Ghimire, S. & Reis, D. A. High-harmonic generation from solids. *Nat. Phys.* **15,** 10–16 (2019).

60. Goulielmakis, E. & Brabec, T. High harmonic generation in condensed matter. *Nat. Photonics* **16,** 411–421 (2022).

61. Tzallas, P., Skantzakis, E., Nikolopoulos, L., Tsakiris, G. D. & Charalambidis, D. Extreme-ultraviolet pump–probe studies of one-femtosecond-scale electron dynamics. *Nat. Phys.* **7,** 781–784 (2011).

62. Carpeggiani, P. *et al.* Disclosing intrinsic molecular dynamics on the 1-fs scale through extreme-ultraviolet pump-probe measurements. *Phys. Rev. A* **89,** 023420 (2014).

63. Sansone, G., Poletto, L. & Nisoli, M. High-energy attosecond light sources. *Nat. Photonics* **5,** 655–663 (2011).

64. Brabec, T. & Krausz, F. Intense few-cycle laser fields: Frontiers of nonlinear optics. *Rev. Mod. Phys.* **72,** 545 (2000).

65. Corkum, P. B. & Krausz, F. Attosecond science. *Nat. Phys.* **3,** 381–387 (2007).

66. Trebino, R. *Frequency-Resolved Optical Gating: The Measurement of Ultrashort Laser Pulses* (Springer Science & Business Media, 2000).

67. Ishii, N. *et al.* Carrier-envelope phase-dependent high harmonic generation in the water window using few-cycle infrared pulses. *Nat. Commun.* **5,** 3331 (2014).

68. Bloembergen, N. *Encounters In Nonlinear Optics: Selected Papers of Nicolaas Bloembergen (With Commentary)* (World Scientific, 1996).

69. Shen, Y.-R. *Principles of Nonlinear Optics* (Wiley-Interscience, New York, NY, USA, 1984).

70. Jürgens, P. *et al.* Origin of strong-field-induced low-order harmonic generation in amorphous quartz. *Nat. Phys.* **16,** 1035–1039 (2020).

71. Han, S. *et al.* Extraction of higher-order nonlinear electronic response in solids using high harmonic generation. *Nat. Commun.* **10,** 3272 (2019).

72. Krause, J. L., Schafer, K. J. & Kulander, K. C. High-order harmonic generation from atoms and ions in the high intensity regime. *Phys. Rev. Lett.* **68,** 3535 (1992).

73. Vampa, G. *et al.* Theoretical Analysis of High-Harmonic Generation in Solids. *Phys. Rev. Lett.* **113,** 073901 (2014).

74. Keldysh, L. *et al.* Ionization in the field of a strong electromagnetic wave. *Sov. Phys. JETP* **20,** 1307–1314 (1965).

75. Brunel, F. Harmonic generation due to plasma effects in a gas undergoing multiphoton ionization in the high-intensity limit. *J. Opt. Soc. Am. B.* **7,** 521–526 (1990).

76. Vampa, G. & Brabec, T. Merge of high harmonic generation from gases and solids and its implications for attosecond science. *J. Phys. B: At. Mol. Opt. Phys* **50,** 083001 (2017).

77. Ivanov, M. Y., Spanner, M. & Smirnova, O. Anatomy of strong field ionization. *J. Mod. Opt.* **52,** 165–184 (2005).

78. Ferris, C. Theoretical modeling of laser-induced absorption phenomena in optical materials. Master's thesis. *University of Nebraska-Lincoln.* Accessed: 10-10-2022. https://digitalcommons.unl.edu/elecengtheses/52/ (2014).

79. Yudin, G. L. & Ivanov, M. Y. Nonadiabatic tunnel ionization: Looking inside a laser cycle. *Phys. Rev. A* **64,** 013409 (2001).

80. Zhokhov, P. & Zheltikov, A. Field-Cycle-Resolved Photoionization in Solids. *Phys. Rev. Lett.* **113,** 133903 (2014).

81. Keldysh, L. V. Multiphoton ionization by a very short pulse. *Physics-Uspekhi* **60,** 1187 (2017).

82. Ammosov, M. V., Delone, N. B. & Krainov, V. P. Tunnel ionization of complex atoms and of atomic ions in an alternating electromagnetic field. *Soviet Journal of Experimental and Theoretical Physics* **64,** 1191 (1986).

83. Brugnera, L. *et al.* Trajectory Selection in High Harmonic Generation by Controlling the Phase between Orthogonal Two-Color Fields. *Phys. Rev. Lett.* **107,** 153902 (2011).

84. Kaxiras, E. *Atomic and Electronic Structure of Solids* (Cambridge University press, 2003).

85. Bloch, F. Über die Quantenmechanik der Elektronen in Kristallgittern. *Zeitschrift für physik* **52,** 555–600 (1929).

86. Zener, C. A theory of the electrical breakdown of solid dielectrics. *Proc. R. Soc. Lond. A* **145,** 523–529 (1934).

87. Wu, M., Ghimire, S., Reis, D. A., Schafer, K. J. & Gaarde, M. B. High-harmonic generation from Bloch electrons in solids. *Phys. Rev. A* **91,** 043839 (2015).

88. You, Y. S. *et al.* Laser waveform control of extreme ultraviolet high harmonics from solids. *Opt. Lett.* **42,** 1816–1819 (2017).

89. Spielmann, C. *et al.* Generation of coherent X-rays in the water window using 5-femtosecond laser pulses. *Science* **278,** 661–664 (1997).

90. Cousin, S. *et al.* High-flux table-top soft x-ray source driven by sub-2-cycle, CEP stable, 1.85-μm 1-kHz pulses for carbon K-edge spectroscopy. *Opt. Lett.* **39,** 5383–5386 (2014).

91. Kazamias, S. & Balcou, P. Intrinsic chirp of attosecond pulses: Single-atom model versus experiment. *Phys. Rev. A* **69,** 063416 (2004).

92. Varjú, K. *et al.* Frequency chirp of harmonic and attosecond pulses. *J. Mod. Opt.* **52,** 379–394 (2005).

93. Chang, Z. *Fundamentals of Attosecond Optics* (CRC press, 2016).

94. López-Martens, R. *et al.* Amplitude and Phase Control of Attosecond Light Pulses. *Phys. Rev. Lett.* **94,** 033001 (2005).

95. Kim, K. T. *et al.* Self-Compression of Attosecond High-Order Harmonic Pulses. *Phys. Rev. Lett.* **99,** 223904 (2007).

96. Vampa, G. *et al.* Linking high harmonics from gases and solids. *Nature* **522,** 462–464 (2015).

97. Ortmann, L. & Landsman, A. S. in *Advances In Atomic, Molecular, and Optical Physics* 103–156 (Elsevier, 2021).

98. Korbman, M., Kruchinin, S. Y. & Yakovlev, V. S. Quantum beats in the polarization response of a dielectric to intense few-cycle laser pulses. *New J. Phys.* **15,** 013006 (2013).

99. Wu, M., Browne, D. A., Schafer, K. J. & Gaarde, M. B. Multilevel perspective on high-order harmonic generation in solids. *Phys. Rev. A* **94,** 063403 (2016).

100. Houston, W. Acceleration of Electrons in a Crystal Lattice. *Phys. Rev.* **57,** 184 (1940).

101. Kim, Y. W. *et al.* Spectral Interference in High Harmonic Generation from Solids. *ACS Photonics* **6,** 851–857 (2019).

102. Faisal, F. & Kamiński, J. Floquet-Bloch theory of high-harmonic generation in periodic structures. *Phys. Rev. A* **56,** 748 (1997).

103. Wang, Y., Steinberg, H., Jarillo-Herrero, P. & Gedik, N. Observation of Floquet-Bloch States on the Surface of a Topological Insulator. *Science* **342,** 453–457 (2013).

104. Wannier, G. H. Wave functions and effective Hamiltonian for Bloch electrons in an electric field. *Phys. Rev.* **117,** 432 (1960).

105. Földi, P., Benedict, M. G. & Yakovlev, V. S. The effect of dynamical Bloch oscillations on optical-field-induced current in a wide-gap dielectric. *New J. Phys.* **15,** 063019 (2013).

106. Higuchi, T., Stockman, M. I. & Hommelhoff, P. Strong-Field Perspective on High-Harmonic Radiation from Bulk Solids. *Phys. Rev. Lett.* **113,** 213901 (2014).

107. Glück, M., Kolovsky, A., Korsch, H. J. & Moiseyev, N. Calculation of Wannier-Bloch and Wannier-Stark states. *Eur. Phys. J. D* **4,** 239–246 (1998).

108. Floss, I., Lemell, C., Yabana, K. & Burgdörfer, J. Incorporating decoherence into solid-state time-dependent density functional theory. *Phys. Rev. B* **99,** 224301 (2019).

109. Lindberg, M. & Koch, S. W. Effective Bloch equations for semiconductors. *Phys. Rev. B* **38,** 3342 (1988).

110. Haug, H. & Koch, S. W. *Quantum Theory of the Optical and Electronic Properties of Semiconductors* (World Scientific Publishing Company, 2009).

111. Burns, K. J., Vasil, G. M., Oishi, J. S., Lecoanet, D. & Brown, B. P. Dedalus: A Flexible Framework for Numerical Simulations with Spectral Methods. *Phys. Rev. Res.* **2,** 023068 (2020).

112. Balcou, P., Salières, P., L'Huillier, A. & Lewenstein, M. Generalized phase-matching conditions for high harmonics: The role of field-gradient forces. *Phys. Rev. A* **55,** 3204 (1997).

113. Rundquist, A. *et al.* Phase-Matched Generation of Coherent Soft X-Rays. *Science* **280,** 1412–1415 (1998).

114. Constant, E. *et al.* Optimizing High Harmonic Generation in Absorbing Gases: Model and Experiment. *Phys. Rev. Lett.* **82,** 1668 (1999).

115. Geissler, M., Tempea, G. & Brabec, T. Phase-matched high-order harmonic generation in the nonadiabatic limit. *Phys. Rev. A* **62,** 033817 (2000).

116. Mairesse, Y. *et al.* Attosecond Synchronization of High-Harmonic Soft X-Rays. *Science* **302,** 1540–1543 (2003).

117. Rodríguez-de Marcos, L. V., Larruquert, J. I., Méndez, J. A. & Aznárez, J. A. Self-consistent optical constants of SiO_2 and Ta_2O_5 films. *Opt. Mater. Express* **6,** 3622–3637 (2016).

118. Taib, M. *et al.* First principles study on Zn doped MgO using Hubbard U correction. *Materials Research Express* **6,** 094012 (2019).

119. Giannozzi, P. *et al.* Advanced capabilities for materials modelling with QUANTUM ESPRESSO. *J. Condens. Matter Phys* **29,** 465901 (2017).

120. Perdew, J. P., Burke, K. & Ernzerhof, M. Generalized Gradient Approximation Made Simple. *Phys. Rev. Lett.* **77,** 3865 (1996).

121. Tan, G.-L., Lemon, M. F. & French, R. H. Optical Properties and London Dispersion Forces of Amorphous Silica Determined by Vacuum Ultraviolet Spectroscopy and Spectroscopic Ellipsometry. *J. Am. Ceram. Soc* **86,** 1885–1892 (2003).

122. Yu, C. *et al.* Dependence of high-order-harmonic generation on dipole moment in SiO_2 crystals. *Phys. Rev. A* **94,** 013846 (2016).

123. Heo, S. *et al.* Band gap and defect states of MgO thin films investigated using reflection electron energy loss spectroscopy. *AIP Advances* **5,** 077167 (2015).

124. Roscam Abbing, S. D. C. *et al.* Divergence Control of High-Harmonic Generation. *Phys. Rev. Applied* **13,** 054029 (2020).

125. Roscam Abbing, S. D. C., Campi, F., Zeltsi, A., Smorenburg, P. & Kraus, P. M. Divergence and efficiency optimization in polarization-controlled two-color high-harmonic generation. *Sci. Rep.* **11,** 24253 (2021).

126. Corkum, P. B. & Krausz, F. Attosecond science. *Nat. Phys.* **3,** 381–387 (2007).

127. Schultze, M. *et al.* Attosecond band-gap dynamics in silicon. *Science* **346,** 1348–1352 (2014).

128. Kraus, P. M. *et al.* Measurement and laser control of attosecond charge migration in ionized iodoacetylene. *Science* **350,** 790–795 (2015).

129. Kraus, P. M. & Wörner, H. J. Perspectives of Attosecond Spectroscopy for the Understanding of Fundamental Electron Correlations. *Angewandte Chemie International Edition* **57,** 5228–5247 (2018).

130. Kraus, P. M., Zürch, M., Cushing, S. K., Neumark, D. M. & Leone, S. R. The ultrafast X-ray spectroscopic revolution in chemical dynamics. *Nat. Rev. Chem.* **2,** 82–94 (2018).

131. Sandberg, R. L. *et al.* Lensless Diffractive Imaging using Tabletop Coherent High-Harmonic Soft-X-Ray Beams. *Phys. Rev. Lett.* **99,** 098103 (2007).

132. Zürch, M. *et al.* Real-time and Sub-wavelength Ultrafast Coherent Diffraction Imaging in the Extreme Ultraviolet. *Sci. Rep.* **4,** 7356 (2014).

133. Gardner, D. F. *et al.* Subwavelength coherent imaging of periodic samples using a 13.5 nm tabletop high-harmonic light source. *Nat. Photonics* **11,** 259–263 (2017).

134. Rothhardt, J., Tadesse, G. K., Eschen, W. & Limpert, J. Table-top nanoscale coherent imaging with XUV light. *Journal of Optics* **20,** 113001 (2018).

135. Wörner, H. J., Bertrand, J. B., Kartashov, D. V., Corkum, P. B. & Villeneuve, D. M. Following a chemical reaction using high-harmonic interferometry. *Nature* **466,** 604–607 (2010).

136. Kaplan, C. J. *et al.* Femtosecond tracking of carrier relaxation in germanium with extreme ultraviolet transient reflectivity. *Phys. Rev. B* **97,** 205202 (2018).

137. Kaplan, C. J. *et al.* Retrieval of the complex-valued refractive index of germanium near the M 4, 5 absorption edge. *J. Opt. Soc. Am. B.* **36,** 1716–1720 (2019).

138. Sadegh, N. *et al.* XUV induced bleaching of a tin oxo cage photoresist studied by high harmonic absorption spectroscopy. *Journal of Photopolymer Science and Technology* **33,** 145–151 (2020).

139. Fu, Y. *et al.* High efficiency ultrafast water-window harmonic generation for single-shot soft X-ray spectroscopy. *Commun. Phys* **3,** 92 (2020).

140. Den Boef, A. J. *Optical metrology of semiconductor wafers in lithography* in *International Conference on Optics in Precision Engineering and Nanotechnology (icOPEN2013)* **8769** (2013), 57–65.

141. Den Boef, A. J. Optical wafer metrology sensors for process-robust CD and overlay control in semiconductor device manufacturing. *Surface Topography: Metrology and Properties* **4,** 023001 (2016).

142. Kinoshita, H., Harada, T., Nagata, Y., Watanabe, T. & Midorikawa, K. Development of EUV mask inspection system using high-order harmonic generation with a femtosecond laser. *Japanese Journal of Applied Physics* **53,** 086701 (2014).

143. Krause, J. L., Schafer, K. J. & Kulander, K. C. High-order harmonic generation from atoms and ions in the high intensity regime. *Phys. Rev. Lett.* **68,** 3535 (1992).

144. Lewenstein, M., Salières, P. & L'huillier, A. Phase of the atomic polarization in high-order harmonic generation. *Phys. Rev. A* **52,** 4747 (1995).

145. Bellini, M. *et al.* Temporal coherence of ultrashort high-order harmonic pulses. *Phys. Rev. Lett.* **81,** 297 (1998).

146. Gaarde, M. B. *et al.* Spatiotemporal separation of high harmonic radiation into two quantum path components. *Phys. Rev. A* **59,** 1367 (1999).

147. Schapper, F. *et al.* Spatial fingerprint of quantum path interferences in high order harmonic generation. *Opt. Express* **18,** 2987–2994 (2010).

148. Wikmark, H. *et al.* Spatiotemporal coupling of attosecond pulses. *Proceedings of the National Academy of Sciences* **116,** 4779–4787 (2019).

149. Quintard, L. *et al.* Optics-less focusing of XUV high-order harmonics. *Sci. Adv.* **5,** eaau7175 (2019).

150. Dudovich, N. *et al.* Measuring and controlling the birth of attosecond XUV pulses. *Nat. Phys.* **2,** 781–786 (2006).

151. Shafir, D. *et al.* Resolving the time when an electron exits a tunnelling barrier. *Nature* **485,** 343–346 (2012).

152. Soifer, H. *et al.* Spatio-spectral analysis of ionization times in high-harmonic generation. *Chemical Physics* **414,** 176–183 (2013).

153. He, X. *et al.* Interference effects in two-color high-order harmonic generation. *Phys. Rev. A* **82,** 033410 (2010).

154. Kim, I. J. *et al.* Highly efficient high-harmonic generation in an orthogonally polarized two-color laser field. *Phys. Rev. Lett.* **94,** 243901 (2005).

155. Jin, C., Wang, G., Wei, H., Le, A.-T. & Lin, C. Waveforms for optimal sub-keV high-order harmonics with synthesized two-or three-colour laser fields. *Nat. Commun.* **5,** 4003 (2014).

156. Jin, C., Stein, G. J., Hong, K.-H. & Lin, C. D. Generation of bright, spatially coherent soft X-ray high harmonics in a hollow waveguide using two-color synthesized laser pulses. *Phys. Rev. Lett.* **115,** 043901 (2015).

157. Jin, C. & Lin, C. Control of soft X-ray high harmonic spectrum by using two-color laser pulses. *Photonics Research* **6,** 434–442 (2018).

158. Haessler, S. *et al.* Optimization of quantum trajectories driven by strong-field waveforms. *Phys. Rev.X* **4,** 021028 (2014).

159. Chipperfield, L., Robinson, J., Tisch, J. & Marangos, J. Ideal waveform to generate the maximum possible electron recollision energy for any given oscillation period. *Phys. Rev. Lett.* **102,** 063003 (2009).

160. Lambert, G. *et al.* Towards enabling femtosecond helicity-dependent spectroscopy with high-harmonic sources. *Nat. Commun.* **6,** 6167 (2015).

161. Mahieu, B. *et al.* Control of ellipticity in high-order harmonic generation driven by two linearly polarized fields. *Phys. Rev. A* **97,** 043857 (2018).

162. Zhai, C. *et al.* Ellipticity control of high-order harmonic generation with nearly orthogonal two-color laser fields. *Phys. Rev. A* **101,** 053407 (2020).

163. Fang, Y. & Liu, Y. Optimal control over high-order-harmonic ellipticity in two-color cross-linearly-polarized laser fields. *Phys. Rev. A* **103,** 033116 (2021).

164. L'Huillier, A., Balcou, P., Candel, S., Schafer, K. J. & Kulander, K. C. Calculations of high-order harmonic-generation processes in xenon at 1064 nm. *Phys. Rev. A* **46,** 2778 (1992).

165. Salières, P. *et al.* Feynman's path-integral approach for intense-laser-atom interactions. *Science* **292,** 902–905 (2001).

166. Salières, P., L'huillier, A., Antoine, P. & Lewenstein, M. Study of the spatial and temporal coherence of high order harmonics. *arXiv preprint quant-ph/9710060* (1997).

167. Ferré, A. *et al.* A table-top ultrashort light source in the extreme ultraviolet for circular dichroism experiments. *Nat. Photonics* **9,** 93–98 (2015).

168. Okino, T. *et al.* Direct observation of an attosecond electron wave packet in a nitrogen molecule. *Sci. Adv.* **1,** e1500356 (2015).

169. Drescher, L. *et al.* Extreme-ultraviolet refractive optics. *Nature* **564,** 91–94 (2018).

170. Hohenleutner, M. *et al.* Real-time observation of interfering crystal electrons in high-harmonic generation. *Nature* **523,** 572–575 (2015).

171. You, Y. S. *et al.* High-harmonic generation in amorphous solids. *Nat. Commun.* **8,** 724 (2017).

172. Paul, P.-M. *et al.* Observation of a train of attosecond pulses from high harmonic generation. *Science* **292,** 1689–1692 (2001).

173. Loetgering, L. *et al.* Tailoring spatial entropy in extreme ultraviolet focused beams for multispectral ptychography. *Optica* **8,** 130–138 (2021).

174. Paganin, D. *et al. Coherent X-ray optics* (Oxford University Press on Demand, 2006).

175. Imasaka, K., Kaji, T., Shimura, T. & Ashihara, S. Antenna-enhanced high harmonic generation in a wide-bandgap semiconductor ZnO. *Opt. Express* **26,** 21364–21374 (2018).

176. Han, S. *et al.* High-harmonic generation by field enhanced femtosecond pulses in metal-sapphire nanostructure. *Nat. Commun.* **7,** 13105 (2016).

177. Korobenko, A. *et al.* Generation of structured coherent extreme ultraviolet beams from an MgO crystal. *Opt. Express* **29,** 24161–24168 (2021).

178. Shcherbakov, M. R. *et al.* Generation of even and odd high harmonics in resonant metasurfaces using single and multiple ultra-intense laser pulses. *Nat. Commun.* **12,** 4185 (2021).

179. O'Shea, D. C., Suleski, T. J., Kathman, A. D. & Prather, D. W. *Diffractive optics: design, fabrication, and test* (SPIE press, 2004).

180. Talbot, H. F. LXXVI. Facts relating to optical science. No. IV. *Lond. Edinb. Dublin philos. mag. j. sci.* **9,** 401–407 (1836).

181. Rayleigh, L. XXV. On copying diffraction-gratings, and on some phenomena connected therewith. *Lond. Edinb. Dublin philos. mag. j. sci.* **11,** 196–205 (1881).

182. Doron, O., Michaeli, L. & Ellenbogen, T. Direct and cascaded collective third-harmonic generation in metasurfaces. *J. Opt. Soc. Am. B.* **36,** E71–E77 (2019).

183. Jansen, G., Rudolf, D., Freisem, L., Eikema, K. & Witte, S. Spatially resolved Fourier transform spectroscopy in the extreme ultraviolet. *Optica* **3,** 1122–1125 (2016).

184. Miao, J., Charalambous, P., Kirz, J. & Sayre, D. Extending the methodology of X-ray crystallography to allow imaging of micrometre-sized non-crystalline specimens. *Nature* **400,** 342–344 (1999).

185. Latychevskaia, T. Iterative phase retrieval in coherent diffractive imaging: practical issues. *Applied optics* **57,** 7187–7197 (2018).

186. Gardner, D. F. *et al.* Subwavelength coherent imaging of periodic samples using a 13.5 nm tabletop high-harmonic light source. *Nat. Photonics* **11,** 259–263 (2017).

187. Wang, Z. *et al.* The roles of photo-carrier doping and driving wavelength in high harmonic generation from a semiconductor. *Nat. Commun.* **8,** 1686 (2017).

188. Luu, T. T., Scagnoli, V., Saha, S., Heyderman, L. J. & Wörner, H. J. Generation of coherent extreme ultraviolet radiation from α–quartz using 50 fs laser pulses at a 1030 nm wavelength and high repetition rates. *Opt. Lett.* **43,** 1790–1793 (2018).

189. Campi, F., Abbing, S. D. R., Zhang, Z.-Y., van der Geest, M. & Kraus, P. M. *Efficient extreme-ultraviolet multi-band high-order wave mixing in silica* in *International Conference on X-Ray Lasers 2020* **11886** (2021), 118860G.

190. Hafez, H. A. *et al.* Extremely efficient terahertz high-harmonic generation in graphene by hot Dirac fermions. *Nature* **561,** 507–511 (2018).

191. Roscam Abbing, S. D. C. *et al.* Extreme-Ultraviolet Shaping and Imaging by High-Harmonic Generation from Nanostructured Silica. *Phys. Rev. Lett.* **128,** 223902 (2022).

192. Ku, Y.-S. *et al.* EUV scatterometer with a high-harmonic-generation EUV source. *Opt. Express* **24,** 28014–28025 (2016).

193. Brizuela, F. *et al.* Efficient high-order harmonic generation boosted by below-threshold harmonics. *Sci. Rep.* **3,** 1410 (2013).

194. Rajeev, R. *et al.* In situ frequency gating and beam splitting of vacuum-and extreme-ultraviolet pulses. *Light Sci. Appl.* **5,** e16170–e16170 (2016).

195. Lai, C.-J. *et al.* Wavelength scaling of high harmonic generation close to the multiphoton ionization regime. *Phys. Rev. Lett.* **111,** 073901 (2013).

196. Bertrand, J. *et al.* Ultrahigh-order wave mixing in noncollinear high harmonic generation. *Phys. Rev. Lett.* **106,** 023001 (2011).

197. Heyl, C. *et al.* Macroscopic effects in noncollinear high-order harmonic generation. *Phys. Rev. Lett.* **112,** 143902 (2014).

198. Li, L. *et al.* Scaling law of high harmonic generation in the framework of photon channels. *Phys. Rev. Lett.* **120,** 223203 (2018).

199. Perez-Piskunow, P. M., Usaj, G., Balseiro, C. A. & Torres, L. F. Floquet chiral edge states in graphene. *Phys. Rev. B* **89,** 121401 (2014).

200. Oka, T. & Kitamura, S. Floquet engineering of quantum materials. *Annual Review of Condensed Matter Physics* **10,** 387–408 (2019).

201. Lindner, N. H., Refael, G. & Galitski, V. Optically engineering the topological properties of a spin Hall insulator. *Nat. Phys* **7,** 490 (2011).

202. McIver, J. W. *et al.* Light-induced anomalous Hall effect in graphene. *Nat. Phys.* **16,** 38–41 (2020).

203. Silva, R., Blinov, I. V., Rubtsov, A. N., Smirnova, O. & Ivanov, M. High-harmonic spectroscopy of ultrafast many-body dynamics in strongly correlated systems. *Nat. Photonics* **12,** 266–270 (2018).

204. Lakhotia, H. *et al.* Laser picoscopy of valence electrons in solids. *Nature* **583,** 55–59 (2020).

205. Li, J. *et al.* Attosecond science based on high harmonic generation from gases and solids. *Nat. Commun.* **11,** 2748 (2020).

206. Yost, D., Schibli, T. & Ye, J. Efficient output coupling of intracavity high-harmonic generation. *Opt. Lett.* **33,** 1099–1101 (2008).

207. Pupeza, I. *et al.* Compact high-repetition-rate source of coherent 100 eV radiation. *Nat. Photonics* **7,** 608–612 (2013).

208. Martini, R. *et al.* Superradiant emission from Bloch oscillations in semiconductor superlattices. *Phys. Rev. B* **54,** R14325 (1996).

209. Heide, C. *et al.* Probing electron-hole coherence in strongly driven 2D materials using high-harmonic generation. *Optica* **9,** 512–516 (2022).

210. Mairesse, Y. *et al.* High-order harmonic transient grating spectroscopy in a molecular jet. *Phys. Rev. Lett.* **100,** 143903 (2008).

211. Ruf, H. *et al.* High-harmonic transient grating spectroscopy of NO2 electronic relaxation. *The Journal of Chemical Physics* **137,** 224303 (2012).

212. Kraus, P. M. & Wörner, H. J. Time-resolved high-harmonic spectroscopy of valence electron dynamics. *Chemical Physics* **414,** 32–44 (2013).

213. Nighan Jr, W., Gong, T., Liou, L. & Fauchet, P. Self-diffraction: a new method for characterization of ultrashort laser pulses. *Optics communications* **69,** 339–344 (1989).

214. Eichler, H. J. & Hermerschmidt, A. in *Photorefractive Materials and Their Applications 1* 7–42 (Springer, 2006).

215. Guizard, S. *et al.* Contrasted behaviour of an electron gas in MgO, Al2O3 and SiO2. *EPL (Europhysics Letters)* **29,** 401 (1995).

216. Bachelier, G. *et al.* Origin of optical second-harmonic generation in spherical gold nanoparticles: Local surface and nonlocal bulk contributions. *Phys. Rev. B* **82,** 235403 (2010).

217. Kolkowski, R., Petti, L., Rippa, M., Lafargue, C. & Zyss, J. Octupolar plasmonic meta-molecules for nonlinear chiral watermarking at subwavelength scale. *ACS Photonics* **2,** 899–906 (2015).

218. Kolkowski, R. & Koenderink, A. F. Gain-induced scattering anomalies of diffractive metasurfaces. *Nanophotonics* **9,** 4273–4285 (2020).

List of Publications

This thesis is based on the following publications:

1 S.D.C. Roscam Abbing, F. Campi, F.S. Sajjadian, N. Lin, P. Smorenburg and P.M. Kraus. "*Divergence Control of High-Harmonic Generation*", Physical Review Applied, **13**,054029 (2020)
Presented in Chapter 4.

2 S.D.C. Roscam Abbing, F. Campi, A. Zeltsi, P. Smorenburg and P.M. Kraus, "*Divergence and efficiency optimization in polarization-controlled two-color high-harmonic generation*", Scientific Reports, **11**, 24253 (2021)
Presented in Chapter 4.

3 S.D.C. Roscam Abbing, R. Kolkowski, Z. Zhang, F. Campi, L. Lötgering, A.F. Koenderink, and P.M. Kraus , "*Extreme-Ultraviolet Shaping and Imaging by High-Harmonic Generation from Nanostructured Silica*", Physical Review Letters, **128**, 223902, (2022)
Presented in Chapter 5.

4 S.D.C Roscam Abbing, F.Campi, B. de Keijzer, C. Morice, Z. Zhang, M.L.S. van der Geest, and P.M. Kraus, "*Efficient extreme-ultraviolet high-order wave mixing from laser-dressed silica*", submitted to Nature Communications.
Presented in Chapter 6.

5 S.D.C Roscam Abbing, N. Kuzkova, F. Campi, and P.M. Kraus, "*Transient high-harmonic spectroscopy in MgO*", in preparation.
Presented in Chapter 7

Summary

The light source that has revolutionized attosecond science over the last decades is based on the process of high-harmonic generation (HHG), which is a unique method to generate a broadband coherent spectrum extending into the extreme-ultraviolet (XUV) range. The temporal and spatial resolution of HHG enables investigation of strong-field light-matter interaction in the ultrafast and ultrasmall dimensions, and finds applications in attosecond science, lensless imaging, and industrial metrology. Unfortunately, the intrinsic low conversion efficiency of HHG and the limited methods to control the generated XUV wavefront, slow down present research and future development of applications that are based on HHG. Control over the HHG process is essential to improve the conversion efficiency and XUV wavefront characteristics, in order to facilitate next-generation attosecond science and metrology.

The generation of high-harmonics emerges from the electron dynamics that are induced by strong-field light-matter interaction. In gas-based HHG, the strong field ionizes an electron from the atom, subsequently the electron is accelerated in the field, and finally recombines with the parent ion, resulting in the emission of XUV photons. In solid-based HHG, the combination of excitation and recombination of carriers between energy bands, referred to as interband processes, and the acceleration of carriers within the band, called the intraband processes, both lead to the generation of harmonics. Since the characteristics of the HHG process are determined by the strong-field light-matter interaction, the generated XUV pulses can be used to probe this interaction directly.

This thesis presents experimental techniques and results that demonstrate control over both gas-based and solid-based HHG in the extreme-ultraviolet regime. Additionally, the underlying mechanism and working principles are explained through theoretical models and simulations, of which the theoretical background is described in Chapter 2. All experiments were performed using intense femtosecond pulses, and details on the generation and manipulation of these pulses using optics is presented in the Chapter 3.

In Chapter 4, we demonstrate divergence and yield optimization in polarization controlled two-color gas-based HHG. Imaging, spectroscopy, and metrology applications using HHG sources require high XUV brightness, related to the conversion efficiency and the focusability of the generated XUV pulses. We systematically investigate, both experimentally and theoretically, the effect of the relative polarization between the fundamental and its second harmonic in two-color HHG, and compare the results to a one-color configuration. In a perpendicular two-color field, the relative phase between the two colors can be used to manipulate the long or the short trajectories, allowing control over the divergence of the harmonics. In a parallel two-color field, the relative phase can be used to modify the ionization rate to select trajectories and additionally allows to

enhance the total yield.

Next, we describe extreme-ultraviolet shaping and imaging by HHG from nanostructured silica in Chapter 5. Tailoring of any XUV wavefront after generation is challenged by the lack of efficient optical elements and limits HHG applications. We demonstrate how HHG from a structured generation medium enables control over the phase, amplitude, and polarization properties of extreme-ultraviolet pulses. Moreover, we use the emitted patterns to reconstruct height profiles, probe the near-field confinement in nanostructures below the diffraction limit of the fundamental, and image complex structures using the coherent diffractive emission from the structures.

In another experiment, we establish efficient extreme-ultraviolet high-order wavemixing from laser-dressed silica, described in Chapter 6. Solid-based HHG allows to produce a coherent, broadband, extreme-ultraviolet light source with tailored emission profiles, but is put at disadvantage due to the low conversion efficiency from infrared to XUV photons. Here, we overcome the low conversion efficiency by driving the HHG simultaneously with the fundamental and its second harmonic, in a non-collinear geometry. The observed high-order wave mixing emission follows perturbative intensity scalings and enhances the XUV efficiency by at least one order of magnitude. The underlying generation mechanism is described by a quantum theory, that reveals that solid HHG is boosted through laser-dressed states.

Finally, we demonstrate transient grating high-harmonic spectroscopy in MgO in Chapter 7, and investigate how an excited carrier population influences solid-state HHG. Two crossed 266-nm pulses induce a transient grating of excited carrier population due to two-photon absorption in the MgO. The modification of the relative amplitude and phase of the harmonics at the generation plane results in diffraction in the far field. Preliminary analysis demonstrates that both the macroscopic propagation effects onto the fundamental and the microscopic generation mechanism of the HHG process contribute to the amplitude and phase modulation.

Samenvatting

De afgelopen decennia is de wetenschap zich steeds meer gaan bezighouden met het bestuderen van ultrasnelle femtoseconde (= 10^{-15} s) processen en ultrakleine nanometer (= 10^{-9} m) karakteristieken van onze wereld. De lichtbron die de laatste decennia een revolutie teweeggebracht heeft in dat vakgebied is gebaseerd op het proces van hogere harmonische generatie (HHG). Dit proces is een unieke manier om een breedbandig coherent licht spectrum te genereren dat zich uitstrekt tot in het extreem-ultraviolet (XUV) regime. De korte XUV golflengtes worden in attoseconde (= 10^{-18} s) lichtpulsen gegenereerd, waardoor HHG een uitstekende techniek is om ultrasnelle fysische processen te onderzoeken in het vakgebied van de attoseconde wetenschap. Daarnaast lenen de korte XUV golflengtes zich voor lensloze beeldvorming en industriële metrologie, een vakgebied wat zich bezig houdt met het inspecteren en bestuderen van kleine structuren op de nanometer schaal. Helaas zitten er ook nadelen aan de HHG techniek. Ten eerste, is het genereren van de XUV fotonen erg inefficiënt. Ten tweede, is het uitermate lastig om het XUV licht te beheersen, omdat normale lenzen en spiegels niet goed werken voor de korte golflengtes. Deze nadelen zorgen ervoor dat de huidige wetenschap en toekomstige toepassingen, die gebaseerd zijn op de HHG techniek, worden vertraagd. Controle over het HHG proces is essentieel om de omzettings efficiëntie en het gebruik van het XUV licht te verbeteren, om de volgende generatie van attoseconde wetenschap en nanometer metrologie te faciliteren.

De generatie van hogere harmonische komt voort uit de beweging van de elektronen die wordt geïnduceerd door de intense licht-materie interactie. In gas-HHG, ioniseert het sterke laser veld een elektron van het atoom, waarna het elektron vervolgens wordt versneld door het laser licht, en tenslotte recombineert met het atoom waaruit het ioniseerde, wat resulteert in de emissie van hoog energetische XUV fotonen. Bij HHG, waarbij een vaste stof dient als generatie medium, leidt de combinatie van excitatie en recombinatie van geladen deeltjes tussen energiebanden, de zogenaamde interband processen, en de versnelling van geladen deeltjes binnen de energieband, de zogenaamde intraband processen, beide tot het ontstaan van hogere harmonische. Aangezien de karakteristieken van het HHG proces bepaald worden door de licht-materie interactie, kunnen de opgewekte XUV pulsen gebruikt worden om deze interactie te bestuderen.

Dit proefschrift presenteert experimentele technieken en resultaten, die controle aantonen over zowel gas-gebaseerde als vaste stof-gebaseerde HHG in het extreem-ultraviolet regime. Bovendien worden het onderliggende mechanisme en de werkingsprincipes toegelicht door middel van theoretische modellen en simulaties, waarvan de theoretische achtergrond wordt beschreven in hoofdstuk 2. Alle experimenten werden uitgevoerd met intense femtoseconde pulsen, en details over het genereren en manipuleren van deze pulsen met behulp van optica worden gepresenteerd in hoofdstuk 3.

In hoofdstuk 4 demonstreren we de optimalisatie van de divergentie en de signaal sterkte van gas-HHG door middel van polarisatie-gecontroleerde twee-kleuren HHG. Toepassingen die gebruik maken van HHG bronnen, zoals beeldvorming, spectroscopie, en metrologie, vereisen een hoge XUV helderheid, wat gerelateerd is aan de omzettings-efficiëntie en de focusseerbaarheid van de gegenereerde XUV pulsen. Wij onderzoeken systematisch, zowel experimenteel als theoretisch, het effect van de relatieve polarisatie tussen de fundamentele laser en zijn tweede harmonische in twee-kleuren HHG, en vergelijken de resultaten met een één-kleuren configuratie. In een loodrecht tweekleurenveld kan de relatieve fase tussen de twee kleuren worden gebruikt om de lange of de korte elektronen banen te manipuleren, waardoor controle over de divergentie van de hoge harmonischen mogelijk wordt. In een parallel tweekleurenveld kan de relatieve fase worden gebruikt om de ionisatie stap te manipuleren om specifieke elektronen banen te selecteren en maakt het bovendien mogelijk om het gehele HHG signaal te versterken.

Vervolgens beschrijven we het vormgeven van extreem-ultraviolet licht en beeldvorming door middel van HHG van nano-gestructureerd silica in hoofdstuk 5. Het op maat maken van een XUV golffront na generatie wordt bemoeilijkt door het gebrek aan efficiënte optische elementen en beperkt HHG toepassingen. Wij tonen aan hoe HHG van een gestructureerde vaste stof controle mogelijk maakt over de fase, amplitude en polarisatie-eigenschappen van extreem-ultraviolette pulsen. Bovendien gebruiken we de uitgezonden patronen om hoogteprofielen te reconstrueren, de verdeling van het laser licht in nanostructuren onder de diffractielimiet van de fundamentele te onderzoeken, en complexe structuren af te beelden met behulp van de coherente diffractieve emissie van de structuren.

In een volgend experiment stellen we efficiënte extreme-ultraviolette hoge-orde golfvermenging vast in siliciumdioxide, beschreven in hoofdstuk 6. HHG in een vaste stof maakt het mogelijk een coherente, breedbandige, extreem-ultraviolette lichtbron te produceren met op maat gemaakte emissieprofielen, maar wordt benadeeld door de lage omzettingsefficiëntie van infrarode naar XUV fotonen. Door HHG tegelijkertijd aan te drijven met de fundamentele en zijn tweede harmonische, in een niet-collineaire geometrie, overkomen we de lage omzettingsefficiëntie. De waargenomen hoge-orde golfmenging volgt perturbatieve intensiteits schalingen en verhoogt de XUV efficiëntie met ten minste een orde van grootte. Het onderliggende generatiemechanisme wordt beschreven door een kwantumtheorie, die onthult dat HHG in een vaste stof wordt versterkt door laser beïnvloede kwantum toestanden.

Tenslotte demonstreren we in hoofdstuk 7 roostervormige hoog-harmonische spectroscopie in MgO, en onderzoeken we hoe een populatie van aangeslagen geladen deeltjes HHG in een vaste stof beïnvloedt. Twee gekruiste 266-nm pulsen induceren een rooster van aangeslagen elektronen, door middel van twee-foton absorptie in MgO. De verandering van de relatieve amplitude en fase van de hoge harmonischen in het generatievlak resulteert in diffractie in het detectievlak. Uit een voorlopige analyse blijkt dat zowel de macroscopische propagatie-effecten op het fundamentele veld als het microscopische opwekkingsmechanisme van het HHG process bijdragen aan de amplitude- en fasemodulatie.

Acknowledgements

As the final part of this thesis I would like to thank all of the people who helped me along the way and who made this PhD an exceptional and unforgettable experience for me.

First of all, I would like to thank my supervisor Peter Kraus. Since day one of my PhD, your passion for science has been contagious and has been the driving force for so many fun and interesting discussions and experiments. Not only your enthusiastic guidance, but also your ambitiousness, accepting (laser) failures, and always going the extra mile, make you an 'uitstekende' group leader. Thank you for the last four amazing years! I look forward to see where the group is headed, and am excited that I can witness that from the sideline in my next job.

Secondly, I want to thank all previous and current members of the HHG and EUV science group, my PhD was truly a team effort, and would not have been as successful and fun without any of the group members. Filippo Campi, with your HHG experience my PhD got a great kickstart. The endless discussions about science, but also about life, pulled me through the covid lockdowns and the less motivated moments, thank you! Maarten van der Geest, as my fellow PhD student in the group we experienced many things together over the last four years, thank you for being part of the journey and making it so much more fun! Also, the cute pictures of your daughter were a great distraction during the last few years. Reinout Jaarsma, although you will not be able to read this anymore, your hard work during the first part of my PhD has to be praised here. Building the setup from scratch, moving it to the other lab, and always being there with last-minute inventions proved what a skilled person you were. Your passing away reminds me on a daily basis that life is fragile and should be enjoyed every moment. Najmeh Sadegh, it was great having you around in the group and office, I admire your perseverance and that you always keep smiling! Zhonghui Nie, thank you for all the many interesting discussion about strong-field light-matter interaction, science in general, and world politics, I learned a lot from you! Stefan Lehmann, during the last year you made sure the laser was well behaving and made it possible for me to finish. Thank you for all your wisdom and advice, laughs, and gezelligheid! Falco Bijloo, when you started, your sparkling enthusiasm about nonlinear optics and photonics reminded me how cool it actually is! Thank you for all the fun coffee breaks and physics chats! Nataliia Kuzkova, you were my partner in crime during the last part of my PhD. With your experience and talent it was possible to finish the final experiments smoothly, the setup is in great hands with you. Your drive, dedication, and motivation are inspiring, and i truly admire your strength and courage during the last year. Leo Guery, only during the last group outing I really started to get to know you, who knew you were such a karaoke fan. Also, I still volunteer for a glass of champagne from your home town. Kevin Murzyn, from the start we had a great connection, possibly because of our matching hair style. Thank you for all the foosball games, tire replacements, and for the social atmosphere you bring to the group and the institute! Peter Juergens, i really appreciated and enjoyed all the many interesting discussions about ionization and strong-field physics we had during the last few months! Faegheh, thank you for your help and company during the first months of my PhD, and getting the first experiments going. Zoey, your enthusiasm, skills, and curiosity regarding structured-solid HHG have led to many great successes and results in the group, thank you! Alexandra, your hard work and organized way of working helped to get the second paper on divergence control finalized, thank you. Roy, with even two student projects, we had the chance to enjoy your jokes for quite some time and do out of the box HHG experiments, thanks! Brian, because of your AwesomeSBE project we managed to get much more understanding about solid HHG than before, thank you for your hard work!

Next, I would like to thank my promotor Stefan Witte, thank you for all the advice and insights regarding finishing my PhD during the last year! Moreover, I would like to thank all the collaborators of the scientific projects over the last years. Thank you Peter Smorenburg, with your simulations on two-color HHG we were able to get a complete story matching the experimental results! Nan Lin, thank you for helping with the first two-color HHG experiments in the lab. Femius Koenderink, it was great working together on the structured-solid HHG project, and to be able to link extreme nonlinear optics and nanophotonics! Radek Kolkowski, your simulations on field distribution in silica helped to solve our mystery, thanks for your creative insights! Lars Loetgering, your propagation code allowed to reproduce our experimental results, thank you for sharing your experience regarding XUV imaging. Corentin Morice, without your help I would never be able to do any DFT calculations, thank you for showing me all the tricks!

During most of my PhD I was involved with experimental work in the lab, and since I started with an empty optical table and lab that means the entire setup had to be designed/made/installed from scratch. It is with the great help of all technicians at ARCNL and the supporting staff at AMOLF, that my experiments were possible at all. Arend-Jan, Nik, Laurens, Mark, Bart-Jan and Thomas M, thank you all so much for always being there to help! I really had a great time working together with you all, you are the backbone of the institute that we can always count on. The workplace at AMOLF delivered excellent work regarding making the setup, thank you all for your great work! Also a big thanks to the software and electronics department, with always being there with quick solutions to get the experiments working.

Additionally, I would like to thank Marjan en Joost for making sure ARCNL is a wonderful place to work at. As part of the OR, together with Stefan, Roland and Bart-Jan, I had the opportunity to work closely together with you, which I really enjoyed! Also, I would like to thank all the other group leaders of ARCNL for their dedication to let the institute thrive. All of you contribute to an open atmosphere at ARCNL, where there is always time to talk about science, thank you! Moreover, I would like to thank Romy, Rosa, Cathelijne, and Marja, for keeping ARCNL running! It was great to have you around as the stable factor at ARCNL, thank you for always helping out!

Over the last four years, I had the pleasure to meet many kind, fun, and diverse people from all over the world at ARCNL. In the old building, the social activities started for me when I joined the PV. I had so much fun organizing the activities with the PV, which have resulted into many memories I will cherish for life. Thank you Victor, Maicie, Vanessa, Fiona, Gorsel, Jan, John, Neha, Zazo, Lucas, Yahia, Ksenia, and Ester, for the unforgettable borrels, activities, and legendary organization! Besides the PV activities, you were all always open for a chat, and made my time at ARCNL amazing! Next, I want to thank Team Astrella, starting with Guido: my Astrella-twin during the first three years of my PhD, thank you for being a great friend at ARCNL, all the laughs, and laser talk! As newest member of Team Astrella, I would like to thank Thomas vd H, for your help and the many foosball games during the last year, which provided the necessary breaks while writing my thesis. Given the amount of hours I spend at the foosball table, I should thank Marjan again, for introducing it after the move and starting a new social era at ARCNL! I met many great people at the table, and it was a great distraction for me over the years. Thanks to anyone who I played with over the years: Randy, Stephen, Maksym, Matthijs (thanks for the extra workout during all the games, having to get the ball from the other side of the atrium all the time..), Christos, Zoi, Perry, Zeudi (your shooting power still gives me nightmares), Ale A, Ale T, Lars L. Lars B, Anne, Kevin, Ruben, Joris, Diko, Bo, Lorenzo and Tamar. In hindsight, this list should contain everyone that I interacted with at ARCNL, thank you all (even if I forgot your name here) for the last years!

Outside my working hours, I had a great group of friends and family who supported me and allowed me to get my mind focused on something else than physics. Thank you to: the Bv5, my oldest friends, the FMB, my high school friends, and Versus/Cava, my friends from Utrecht! You were always interested in my work, and allowed me to practice communicating science in an understandable way, you are all friends for life! Additionally, a big thank you to my extended family for distracting me from work with many fun holidays and activities. A special thanks to Tanja and Georges for designing the front cover! Sometimes I think that growing up with two older brothers is what got me into this career path, make it a never ending sibling competition and always looking for a challenge. Thank you Marnix and Reinout for being my brothers and providing me with advice all along the way. In addition, thanks to both Amber and Miryam, for your honest interest in my work, and ofcourse thanks to Hidde en Mink, for being part of the family and lightening up our lives. Next, I would like to thank my parents Pieter en Renske for always being there for me and supporting me in every step I make. Pap, thank you for passing on your interest for technology, your patience, and your optimism, onto me. Mam, thank you for being an amazing role model, I learned a lot from your ambition, discipline and drive. Finally, Arjan, thank you for everything, you make my dreams come true.